University of Kent

Doctoral Thesis

Reservoir Computing-assisted optical system for high-throughput applications

---

Author:
Yuanli Yue

Supervisor:
Dr Chao Wang

A thesis submitted in fulfilment of the requirements for the degree of Doctor of Philosophy in Electronic Engineering

May 2025

Page count: 177 pages

Abstract

High-throughput photonic systems enable ultrafast data acquisition in many applications, but the large volumes of generated data create significant challenges for real-time signal processing. This thesis investigates optical approaches for high-throughput applications using machine learning-based reservoir computing (RC). As a simplified form of recurrent neural networks (RNNs), RC significantly reduces training complexity while maintaining strong capability in processing time-sequential data, making it particularly suitable for classification and prediction tasks in high-speed systems.

RC is first employed as a back-end data analysis tool for two high-throughput applications: indoor user localization and frequency hopping recognition. In the indoor localization system, RC is integrated with a photonic time-stretch framework using a 45° tilted fiber grating (TFG), enabling real-time tracking and accurate position identification of users. A proof-of-concept experiment demonstrates improved localization performance. In the frequency hopping recognition system, RC is applied in the post-processing stage to identify frequency transitions, enabling accurate detection of hopping time and duration while improving system responsiveness.

Building on these applications, an optical hardware implementation of reservoir computing is proposed and experimentally demonstrated. The system combines spectrum mixing, photonic time stretch, and a delay-based memory structure to enable efficient high-speed processing. In this design, both wavelength

and time dimensions are utilized as reservoir nodes, significantly expanding the number of virtual nodes and overcoming limitations in conventional hardware reservoir implementations. Simulation studies investigate key system parameters, including node number, optical feedback strength, and the gain characteristics of the semiconductor optical amplifier (SOA). Experimental results further validate the system through waveform classification and frequency classification tasks.

To further improve processing speed and enable real-time operation, a novel optical masking scheme is introduced. By embedding the mask directly within the optical link, this approach eliminates the electronic bottleneck associated with conventional pre-masking procedures and enables fully optical preprocessing. Three optical mask implementations are investigated and experimentally evaluated. The results demonstrate improved classification accuracy and highlight the potential of all-optical masking for high-speed photonic reservoir computing systems.

Overall, this work demonstrates that optical reservoir computing provides an effective solution for high-throughput machine learning tasks, offering significant advantages in processing speed, scalability, and real-time capability. The proposed architectures and techniques contribute to the development of next-generation photonic computing systems for ultrafast signal processing and intelligent optical sensing.

Acknowledgements

Throughout my four years of doctoral study and the preparation of this thesis, I have been fortunate to receive unwavering support, guidance, and encouragement, for which I am profoundly grateful.

First and foremost, I would like to express my deepest gratitude to my principal supervisor, Dr. Chao Wang. His exceptional expertise, high standards of research excellence, and steadfast support have been instrumental to my academic and personal growth. His insightful advice and constructive feedback continually sharpened my thinking and elevated the quality of my work. Every discussion with him enriched my understanding, inspiring me to push the boundaries of my research.

I am also grateful to my co-supervisor, Dr. Philippos Assimakopoulos, whose valuable insights and constructive feedback have significantly influenced the direction of my research. His thoughtful guidance and encouragement have been pivotal to the completion of this thesis.

Special thanks are due to Mr. Shouju Liu for his invaluable collaboration, which greatly enhanced my research. His support in laboratory access and our stimulating discussions were critical to the progress of my work.

I would also like to extend my sincere thanks to the visiting scholars and group members, including Dr. Yue Feng, Dr. Yanrong Zhai, Mr. Tianxiang Luan, and Mr. Weiqing Liao. Their helpful suggestions and contributions were invaluable in refining my research.

My heartfelt appreciation goes to the technical support staff at the School of Engineering, particularly Qi Zheng, Edwin Lui, Yan Zhang, and Antonio Mendoza. Their assistance and expertise played an indispensable role throughout my research journey. It has been an immense privilege to work alongside such talented and dedicated individuals, and I am deeply honored to have benefited from their guidance and collaboration.

Lastly, and most importantly, I owe my deepest gratitude to my parents. Their unwavering support, wise counsel, and boundless patience have been my foundation throughout this journey. Their encouragement and belief in me have been the driving force behind my accomplishments, and I dedicate this thesis to them.

List of Publications

Peer-reviewed Journal Articles

1. **Y. Yue**, Zhang, H., & Wang, C. "Experimental Demonstration of All-optical Input Masking in Photonic Time-stretch Reservoir Computing," *Journal of Lightwave Technology*, 2026.

2. **Y. Yue**, Y. Feng, S. Liu, & C. Wang*, "All-optical dispersive Fourier analysis for ultrafast user localization at 50 MHz in beam-steered optical wireless communication," *Optics Letters*, 50(23), 7304–7307, 2025.

3. **Y. Yue**, C. K. Mididoddi, N. Jing, & C. Wang*, "Reservoir computing assisted ultrafast user localization in beam steering optical wireless system," *IEEE Photonics Technology Letters*, 33(18), 1030–1033, June 2021.

4. S. Li, Z. Liu, A. Zhang, H. Pan, R. Stancu, **Y. Yue**, R. Zhang, and C. Wang*, "High-speed and high-resolution optical fiber sensor interrogation based on optical injection in semiconductor laser and microwave filtering," *IEEE/OSA Journal of Lightwave Technology*, 40(20), 6805–6812, 2022.

5. **Y. Yue**, C. Wang*, "Reservoir Computing Assisted High-throughput Moving Target Detection," *Optics Express*. (Under Review)

Conference Proceedings

1. **Y. Yue**, S. Liu, and C. Wang*, "All-optical Reservoir Computer using a Multi-mode Fibre-based Optical Mask," *2024 IEEE Photonics Conference (IPC)*, November 2024.

2. **Y. Yue**, S. Liu, and C. Wang*, "Reservoir computing assisted single-pixel high-throughput object classification," *2024 SPIE Photonics Europe*, April 2024.

3. **Y. Yue**, S. Liu, R. Zhang, T. Luan, A. Zhang, and C. Wang*, "Experimental Investigation of an Optical Reservoir Computer with MZI-based Optical Mask," *2023 IEEE International Topical Meeting on Microwave Photonics (MWP)*, October 2023.

4. **Y. Yue**, S. Liu, W. Xu, & C. Wang*, "Experimental Investigation of Time-Stretch-Based Reservoir Computing with an Optical Input Mask," *EOS Annual Meeting (EOSAM)*, Vol. 287, p. 13010, September 2023.

5. **Y. Yue**, S. Liu, Y. Zhai, & C. Wang*, "Enhanced photonic time-stretch reservoir computing using all-optical input masks," *2022 IEEE Photonics Conference (IPC)*, November 2022.

6. **Y. Yue**, S. Liu, Y. Zhai, & C. Wang*, "Experimental Implementation of An All-Optical Reservoir Computer Using Photonic Time Stretch and Spectral Mixing," *2022 IEEE International Topical Meeting on Microwave Photonics (MWP)*, October 2022.

7. **Y. Yue**, S. Liu, Y. Feng, & C. Wang*, "An all-optical reservoir computer based on time stretch and spectral mixing," *2022 Conference on Lasers and Electro-Optics (CLEO)*, May 2022.

8. **Y. Yue**, S. Li, Y. Feng, A. Zhang, & C. Wang*, "Real-time identification of frequency-hopping millimeter-wave signals using photonic time stretch and reservoir computing," *2021 SPIE/COS Photonics Asia*, Vol. 11902, pp. 108–112, October 2021.

9. **Y. Yue**, & C. Wang*, "Ultrafast Beam Steering User Localization in Optical Wireless Communication," *2021 Opto-Electronics and Communications Conference (OECC)*, July 2021.

10. W. Liao, **Y. Yue**, S. Liu, C. Wang, & A. Zhang, "High-Speed Multi-Channel Signal Acquisition in Photonic Time Stretch Optical Coherence Tomography Through Frequency Division Multiplexing," *2024 International Topical Meeting on Microwave Photonics (MWP)*, September 2024.

11. T. Luan, R. Zhang, **Y. Yue**, S. Liu, A. Zhang, C. Wang*, "A Frequency Modulated Continuous Wave LiDAR System Based on Reservoir Computing," *2023 IEEE International Topical Meeting on Microwave Photonics (MWP)*, October 2023.

12. Y. Feng, **Y. Yue**, Q. Wu, and C. Wang*, "Delay-Insensitive Time Stretch Interrogation of Fiber Bragg Grating Sensors," *2022 13th International Symposium on Communication Systems, Networks and Digital Signal Processing (CSNDSP)*, July 2022. (*Best Paper Award*)

13. D. Xiao, L. Shao, C. Wang, G. Wang, P. P. Shum, and **Y. Yue**, "A Curvature Sensor with High Resolution Based on SMS-Structure and Microwave Photonic Filter," *2021 IEEE International Topical Meeting on Microwave Photonics (MWP)*, November 2021.

14. Y. Feng, **Y. Yue**, S. Liu, and C. Wang, "A Remote FBG Sensor Interrogation System Based on a 45-Degree Tilted Fibre Grating," *Optica Sensing Congress*, Optica Publishing Group, 2024.

15. S. Liu, **Y. Yue**, M. Shi, A. Zhang, & C. Wang, "Single-Wavelength Multi-Tap Time Delay Line Over a Multimode Fibre Towards Microwave Photonic Filters," *2024 Conference on Lasers and Electro-Optics Pacific Rim (CLEO-PR)*, August 2024.

List of Abbreviations

A

ADC Analog-to-Digital Converter

ADCs Analog-to-Digital Converters

AI Artificial Intelligence

ANNs Artificial Neural Networks

ARC Acoustic Reservoir Computing

ASE Amplified Spontaneous Emission

AWG Arbitrary Waveform Generator

B

BER Bit Error Rates

BPTT Backpropagation Through Time

BS Beam Splitters

C

CS Compressive Sampling

CW Continuous Wave

D

DCF Dispersive Compensation Fiber

DFT Dispersive Fourier Transformation

DMD Digital Micromirror Device

DNN Deep Neural Network

DSP Digital Signal Processing

DAC Digital-to-Analog Converter

E

EDFA Erbium-Doped Fibre Amplifier

ENOB Effective Number of Bits

EOMs Electro-Optic Modulators

ERC Electronic Reservoir Computing

ESNs Echo State Networks

F

FBGs Fiber Bragg Gratings

FFNNs Feedforward Neural Networks

FFT Fast Fourier Transform

FH Frequency Hopping

FHSS Frequency-Hopping Spread Spectrum

FITH Fiber in the Home

FPGAs Field-Programmable Gate Arrays

FPL Femtosecond Fiber Laser

FSDD Free Spoken Digit Dataset

FSR Free Spectral Range

FTTH Fiber to the Home

FWM Four-Wave Mixing

G

GMMs Gaussian Mixture Models

GVD Group Velocity Dispersion

L

LPFGs Long-Period Fiber Gratings

LSMs Liquid State Machines

LSTM Long Short-Term Memory

LTI Linear Time-Invariant

LiDAR Light Detection and Ranging

M

MIR Mid-Infrared

ML Machine Learning / Mode Locking

MLL Mode-Locked Laser

MMF Multimode Fiber

MMI Multimode Interference

MRC Mechanical Reservoir Computing

MSE Mean-Square Error

MZI Mach-Zehnder Interferometer

MZM Mach-Zehnder Modulator

N

NA Numerical Aperture

NLP Natural Language Processing

NNs Neural Networks

NVMs Non-Volatile Memristors

O

ODE Ordinary Differential Equation

OERC Opto-Electronic Reservoir Computing

OPAs Optical Parametric Amplifiers

OPOs Optical Parametric Oscillators

OWC Optical Wireless Communication

P

PCA Principal Component Analysis

PD Photodetector

PM Polarization-Maintaining

PRC Photonic Reservoir Computing / Optoelectronic & Photonic Reservoir Computing

PTS Photonic Time Stretch

Q

QPRC Quantum Photonic Reservoir Computing

R

RC Reservoir Computing

RF Radio Frequency

RI Refractive-Index

RL Reinforcement Learning

RMSE Root-Mean-Square Error

RNNs Recurrent Neural Networks

S

SAW Surface Acoustic Waves

SLMs Spatial Light Modulators

SMF Single-Mode Fiber

SMFs Single-Mode Fibers

SMS Single-Mode-Multimode-Single-Mode

SNR Signal-to-Noise Ratio

SOAs Semiconductor Optical Amplifiers

SOD Second-Order Dispersion

SOI Silicon-On-Insulator

SRI Surrounding Refractive Index

STFT Short-Time Fourier Transform

STPC Spatiotemporal Photonic Computing

SVMs Support Vector Machines

T

TD Temporal Difference

TDRC Time-Delay-Based Reservoir Computing

TFBG 45-Degree Tilted Fiber Bragg Grating

TFG Tilted Fiber Grating

TOD Third-Order Dispersion

TOF Tunable Optical Filter

ToF Time-of-Flight

U

UV Ultraviolet

V

VLC Visible Light Communication

VOA Variable Optical Attenuator

W

WDM Wavelength Division Multiplexing

Contents

List of Tables

List of Figures

Chapter 1

Introduction

1.1 Background

With the rapid growth of data-intensive applications such as biomedical imaging, high-speed optical communication, and ultrafast spectroscopy, the demand for high-throughput detection has increased significantly. High-throughput detection refers to the ability to rapidly acquire and process large volumes of samples or signals within a short time window [1, 2]. Its workflow typically involves automated data acquisition and fast information processing, enabling efficient and precise analysis. Typical applications include biomedical imaging and diagnostics, high-speed optical communication monitoring, and ultrafast spectroscopy, spanning both academic research and industrial sectors [3, 4].

Compared with conventional detection methods [5, 6, 7, 8], high-throughput detection enables simultaneous or rapid sequential processing, significantly improving the efficiency of data acquisition and analysis. As a result, it offers higher processing speed, improved accuracy, and enhanced scalability.

Applications of high-throughput detection span multiple fields, including biomedical imaging [9] and diagnostics [10], high-speed optical communication

[11], and ultrafast spectroscopy [12]. For instance, in biomedical imaging, it enables real-time analysis of cells and tissues, facilitating early disease diagnosis. In optical communication, high-throughput detection enhances data transmission rates and signal integrity, optimizing the efficiency of modern communication networks.

As the demand for high-throughput detection continues to rise, the need for faster and more accurate data acquisition has become increasingly critical. A major challenge that follows is managing the extremely large volumes of collected data, which can easily exceed several gigabytes per second in typical photonic time-stretch systems due to the high sampling rates (tens to hundreds of mega-samples per second (MSa/s)) and wide optical bandwidths involved [13]. Traditional approaches, such as digital signal processing (DSP) [14] and Fourier-transform-based techniques[15], typically require extensive post-processing and significant computational resources. As data rates continue to increase, these methods struggle to efficiently handle large-scale datasets. Typical high-speed DSP pipelines consume tens of watts of power and require billions of operations per second for real-time processing. For instance, FFT-based signal processing at multi-gigahertz sampling rates demands extremely high computational throughput on FPGA or GPU platforms [16]. As a result, they introduce delays that prevent real-time decision-making, limiting their effectiveness in time-sensitive applications.

To address these challenges, there is an urgent need to develop novel data processing methods that achieve an optimal balance between processing speed and accuracy. This calls for the development of a new high-throughput detection system capable of handling large datasets efficiently, accurately, and in real time.

Photonic Time Stretch (PTS) [17, 18] has emerged as a powerful technique for high-throughput detection and ultrafast optical signal acquisition. It operates by using optical dispersion to slow down high-speed signals before digitization,

enabling the capture of rapid transient events that electronic detectors struggle to detect. By overcoming the speed limitations of conventional electronic devices, PTS has found applications in various fields, including biomedical imaging for single-cell analysis [19, 20, 21], real-time ultrafast spectral analysis in spectroscopy [22], and enhanced signal detection in high-speed optical communication [23].

Despite its advantages, PTS-based systems generate extremely large datasets, often reaching hundreds of megabytes to several gigabytes per second in practical implementations. For example, in state-of-the-art STEAM imaging, the real-time digitizer operates at 50 GSa/s, corresponding to a raw data throughput of over 60 GB/s for a 10-bit acquisition [24]. Traditional data processing methods are computationally expensive, leading to high power consumption and processing delays, making them impractical for large-scale PTS data. Machine learning [25] has emerged as a promising solution for high-throughput data processing, addressing the limitations of conventional digital signal processing (DSP) methods [26]. Machine learning algorithms efficiently handle complex, high-dimensional datasets, adapt to new patterns, and significantly reduce computational complexity, making them ideal for scalable and efficient PTS data processing [27].

Among various machine learning approaches, Recurrent Neural Networks (RNNs) [28, 29, 30] are widely used for processing time-series data due to their ability to capture temporal dependencies in sequential inputs. This makes them well-suited for handling the continuous data streams generated by PTS. However, RNNs have significant drawbacks, including long training times, vanishing gradient issues, and high computational costs, limiting their efficiency in real-time applications.

To overcome these challenges, Reservoir Computing (RC) has emerged as a more efficient neural network architecture [31]. RC utilizes a fixed, randomly initialized reservoir to project input data into a higher-dimensional space, significantly reducing the need for extensive training [32]. Because the reservoir is a

recurrent dynamical system with intrinsic temporal memory, its internal states naturally encode correlations across time, making RC particularly effective for time-series processing. The nonlinear dynamics of the reservoir allow it to capture both short- and long-range temporal dependencies without requiring backpropagation through time. This approach is particularly effective for processing time-gated data, such as the high-speed optical signals produced by PTS. Compared to traditional RNNs, RC offers faster training times and lower computational costs, making it a promising solution for high-throughput detection [33].

Given the strengths of PTS in ultrafast detection and RC in efficient time-series processing, this thesis explores their integration to develop a novel data-processing solution for high-throughput detection systems that balances speed and computational efficiency. The key contributions of this research include: Developing a hybrid system that combines PTS with Reservoir Computing to optimize high-throughput detection. Exploring all-optical reservoir computing to further reduce reliance on DSP and enhance real-time processing capabilities, which is important because optical processing avoids electronic bottlenecks and enables ultralow-latency handling of PTS-scale data rates.

By leveraging the complementary advantages of PTS and RC, this thesis aims to overcome the limitations of traditional DSP-based methods, enabling a faster, more efficient high-throughput detection system for applications in biomedical imaging, ultrafast spectroscopy, and high-speed communication networks.

1.2 Challenges and Aims

As the demand for high-throughput detection continues to grow, this technology has undergone rapid advancements. The integration of high-throughput detection with photonic methods has attracted significant research interest due to its ability to process signals at the speed of light. This combination offers several

advantages, including high sensitivity, precision, and rapid processing, while also enabling non-invasive and label-free detection. Currently, research in photonic reservoir computing primarily focuses on enhancing prediction/classification accuracy and improving processing speed to meet the increasing demands of real-time applications.

Key Challenges in High-Throughput Detection:

Currently, there are two primary challenges in high-throughput detection:

- **Data Overload and Real-Time Processing:** Real-time high-throughput detection generates massive volumes of data within a short period. Efficiently managing, storing, and processing such large datasets in real time remains a major challenge. Traditional computational methods struggle with scalability, leading to processing bottlenecks. Optimized algorithms and advanced processing techniques are needed to maintain efficiency while reducing delays.

- **Balancing Accuracy and Speed:** Even when real-time processing is achieved, maintaining high classification and prediction accuracy remains a critical challenge. Trade-offs between speed and accuracy can impact system performance, as delays or misclassifications reduce reliability in real-world applications. Thus, optimizing data processing pipelines to maintain both high speed and precision is essential.

Research Objectives:

This thesis aims to address these challenges by developing an all-optical reservoir computer that leverages the advantages of photonic time stretch. The research objectives of this thesis can be summarized as follows:

- **To develop a Novel Photonic Reservoir Computing Structure:** Unlike traditional photonic reservoir computing systems, this work integrates

photonic time stretch, which maps signals between wavelength and time to create virtual nodes for nonlinear processing. This approach can significantly increase the number of nodes in the reservoir layer, enhancing computational capacity and overcoming limitations in conventional setups.

- **To improve classification accuracy with all-optical masking in Reservoir computing:** To improve classification accuracy, an optical mask scheme is introduced, which alleviates electronic bandwidth limitations by performing the modulation in the optical domain. Several optical masking techniques are proposed and experimentally evaluated. The results identify the most effective scheme for improving classification accuracy. This strategy enhances the efficiency of the system while maintaining high-speed processing.

This work therefore focuses on developing a hardware-efficient photonic reservoir computing architecture that can process time-stretched signals in real time while maintaining high classification accuracy.

1.3 Contributions of this Thesis

This thesis makes several distinct contributions to the field of photonic time stretch and reservoir computing, particularly in high-throughput detection and optical computing systems. The key contributions are as follows:

- **RC-assisted Indoor User Localization System:** A novel indoor user localization system integrating photonic time stretch and reservoir computing is proposed. The system employs a 45-degree Tilted Fiber Bragg Grating (TFBG) as a diffraction device to spatially disperse wavelengths. User positions are determined by reflecting light of specific wavelengths off individuals, with time-of-flight measurements recorded via an oscilloscope.

Reservoir computing (RC) is utilized for post-processing, enabling accurate recognition of light-carried information and precise localization of multiple users.

- **A Photonic Reservoir Computing Architecture for PTS Systems:** Traditional electronic hardware implementations of reservoir computing often face limitations in scaling the number of physical nodes due to memory, power, and circuit complexity constraints. In contrast, photonic reservoir systems based on time-multiplexing can readily achieve thousands of virtual nodes, as demonstrated in prior work. Building on this capability, this thesis presents an all-optical reservoir computing system based on photonic time stretch and spectrum mixing. Spectrum mixing is employed to generate virtual nodes, thereby increasing the capacity of the reservoir layer. Semiconductor Optical Amplifiers (SOAs) are utilized to provide nonlinear processing, operating in a strongly nonlinear regime. The system is validated through frequency classification and spoken-digit recognition tasks, demonstrating superior performance compared to conventional methods.

- **Photonics Reservoir Computing with an Optical Mask Scheme:** To further enhance processing speed and classification performance, an optical mask scheme is integrated into the photonic reservoir computing system. Building on recent optical masking approaches using free-space or photonic-integrated platforms [34], this work investigates three optical mask techniques specifically tailored for photonic time-stretch signals. In these schemes, wavelength-dependent spectral filtering is mapped into the temporal domain after photonic time-stretching, thereby enriching the reservoir node states, increasing feature diversity, and improving the separability of different input classes. The parallel diffraction-grating mask introduces programmable spatial-spectral encoding; the Mach-Zehnder Interferometer

(MZI)-based mask provides interference-induced spectral modulation; and the Single-Mode-Multimode-Single-Mode (SMS) fiber mask exploits multimode interference to generate a more complex non-uniform spectral response. A comparative analysis of these schemes demonstrates improved classification accuracy and processing efficiency, establishing a robust foundation for future photonic reservoir computing applications.

1.4 Thesis Outline

Chapter 1 introduces the background and motivation of the research, outlines the key challenges in high-throughput detection, and summarizes the main contributions of this thesis.

Chapter 2 presents the theoretical background of the research, including the principles of photonic time stretch and reservoir computing. It begins with an in-depth discussion of Photonic Time Stretch (PTS), covering its mathematical principles, photonic mechanisms, and applications explored in previous studies. Since this thesis focuses on reservoir computing (RC), a specialized form of recurrent neural networks (RNNs), the chapter examines how RC overcomes the training challenges of RNNs. It further categorizes and analyzes different types of reservoir computing architectures, with a focus on advancements in Photonic Reservoir Computing (PRC). Various implementations are reviewed, including electro-optical reservoir computing, all-optical reservoir computing, and integrated photonic reservoir computing based on photonic integration chips.

Chapter 3 investigates the application of reservoir computing in high-throughput signal analysis, including indoor user localization and frequency-hopping recognition. The first application is Indoor User Localization: RC is used to process reflected signals containing spatial information, enabling precise indoor positioning of users based on light reflections. The second application is

Frequency Hopping Detection and Recognition: RC is applied to identify hopping times and classify different frequency bands, enhancing the accuracy of frequency hopping communication systems.

Chapter 4 introduces a photonic reservoir computing architecture based on photonic time stretch and spectral mixing. In this approach, wavelengths are selected as nodes in the reservoir layer, and nonlinear processing is achieved through a semiconductor optical amplifier. Long short-term memory is realized using a variable optical attenuator to adjust feedback strength. The proposed system is tested using basic waveform classification and spoken-digit classification tasks.

Chapter 5 presents an enhanced photonic reservoir computing system incorporating optical input masking techniques. To enhance processing speed and address hardware bandwidth limitations, an all-optical reservoir computing system is introduced, incorporating an optical mask as a programmable optical filter. Three optical mask designs are explored. The first is Parallel Diffraction Gratings – introduces spatial encoding for signal processing. The second is Mach-Zehnder Interferometer (MZI)-Based Optical Mask – utilizes interference-based feature extraction. The third is Single-Mode-Multimode-Single-Mode (SMS) Fiber-Based Optical Mask – enhances mode dispersion for improved system performance. A comparative analysis reveals that the SMS fiber-based optical mask achieves the best performance, optimizing the trade-off between processing speed and accuracy.

Chapter 6 concludes the thesis and discusses potential directions for future research. This chapter summarizes the key findings of the research and discusses future directions for advancing photonic reservoir computing and high-throughput detection.

1.5 Summary

This chapter has introduced the research motivation, identified the key challenges associated with high-throughput optical signal processing, and outlined the objectives and main contributions of this thesis. By positioning reservoir computing within the context of photonic time-stretch systems, the chapter establishes the foundation for the proposed all-optical architecture.

The following chapter presents the theoretical background of photonic time stretch, machine learning, and reservoir computing, providing the fundamental principles required for understanding the proposed system design.

Chapter 2

BACKGROUND STUDY AND LITERATURE REVIEW

Chapter 1 introduced the motivation and significance of this thesis, as well as the key challenges associated with high-throughput detection across various application domains. This research is built upon two key concepts: Photonic Time Stretch (PTS) and Reservoir Computing (RC). In this chapter, I will explore the theoretical foundations of PTS and its integration with machine learning, particularly in achieving photonic reservoir computing (PRC). This combination provides an effective solution to the challenges outlined in Chapter 1, enhancing real-time data processing and improving the efficiency of high-throughput detection systems.

Photonic time stretch enables ultrafast optical signal acquisition, which consequently generates massive volumes of real-time data and creates significant challenges for efficient data processing. Machine learning provides a promising solution due to its ability to handle complex, high-dimensional data efficiently. Among machine learning models, Recurrent Neural Networks (RNNs) are particularly suited for time-series data processing. However, their long training times and high computational complexity limit their applicability in real-time systems.

The remainder of this chapter is organized as follows:

- The first part presents the mathematical foundations and principles of photonic time stretch. This section provides a mathematical analysis of ultrashort optical pulse propagation and the fundamental principles of photonic time stretch (PTS). It then explores dispersive Fourier transformation, explaining how PTS is achieved and how wavelength-to-time mapping is established. The section concludes with a discussion on various applications of PTS across different fields.

- The second part introduces machine learning concepts and reservoir computing. This section introduces key machine learning concepts, including Artificial Neural Networks (ANNs), Feedforward Neural Networks (FFNNs), and Recurrent Neural Networks (RNNs). It then presents reservoir computing (RC), emphasizing its advantages in processing time-series data with low computational cost and high efficiency. The mathematical model, structural components, and training procedure of RC are detailed.

- Furthermore, second section also explores photonic reservoir computing (PRC) and its inherent benefits when integrated with photonic techniques. Several examples of PRC implementations are provided, along with a literature review of recent advancements in the field. The discussion highlights existing methodologies, technological challenges, and future research directions in photonic reservoir computing.

The theoretical models and concepts explored in this chapter serve as the foundation for subsequent chapters, where they are further applied and expanded in photonic reservoir computing applications in high-throughput detection systems.

2.1 Photonic Time-Stretch

2.1.1 Fundamentals of time stretch

Ultrafast photonics plays a critical role in sensing and detection across a wide range of scientific and engineering fields [35]. However, conventional techniques often struggle to detect ultrafast non-stationary processes, primarily due to insufficient response times and the inability to capture rapid changes in real time [36].

In real-time optical measurements, two key challenges limit the effectiveness of current methodologies [37, 38]. The first is the limitations of Analog-to-Digital Converters (ADCs) [39].

In real-time data acquisition, a fundamental trade-off exists between sampling speed and accuracy. Increasing the sampling rate requires shorter aperture times and faster comparator operation, which amplifies thermal noise, quantization errors, and clock jitter. Consequently, high-speed ADCs (> 1 GS/s) typically achieve only 6–8 bits of resolution, making precise digitization of ultrafast signals difficult. The second challenge is the trade-off between conversion speed and sensitivity in the optoelectronic front-end [40]. Higher photoelectric conversion speeds reduce photon collection time, lowering the SNR and thus decreasing detection sensitivity, making it difficult to detect weak or low-contrast ultrafast events while maintaining high operation speeds.

In many ADCs, noise and distortion may reduce the accuracy of signal representation. To address this, the Effective Number of Bits (ENOB) is used as a key performance metric. ENOB quantifies the number of effective bits that contain meaningful information, offering a more accurate assessment of ADC performance. It is typically measured at a specific analog input frequency and serves as a critical parameter for evaluating the effectiveness of ADCs in high-speed signal processing.

ENOB can be mathematically expressed as:

$$\text{ENOB} = \frac{10 \times \log_{10}\left(\frac{P_{\text{signal}}}{P_{\text{noise}}+P_{\text{distortion}}}\right) - 1.76}{6.02} \tag{2-1}$$

where P_{signal}, P_{noise} and $P_{\text{distortion}}$ represent the powers of the signal, noise, and distortion, respectively, it is assumed that the input signal amplitude corresponds to the full-scale range of the ADC input. Generally, ENOB decreases as the signal frequency increases.

To overcome the speed limitations of ADCs using non-electronic methods, Coppinger et al. (1999) [41] introduced the photonic time-stretch technique. This method allows for the measurement and analysis of non-stationary phenomena in ultra-high-speed systems by slowing down the signal before digitization, enabling more effective sampling and processing. Fig. 2.1 illustrates and compares the time-stretch procedure with the direct sampling approach [42].

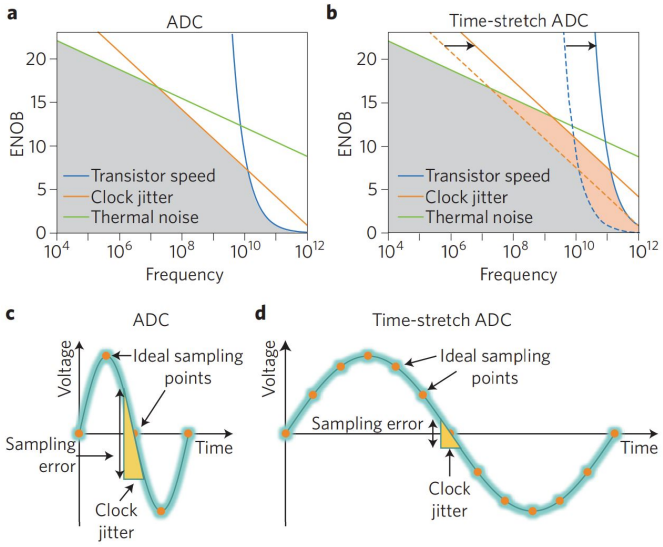

Fig. 2.1: Digitizer Limitations and Time-Stretch Solution.

The performance of high-speed digitizers is fundamentally limited by several physical constraints, including comparator ambiguity arising from the finite gain-bandwidth product of transistors [43], sampling errors caused by clock (aperture) jitter [44], and intrinsic thermal (Johnson) noise [45]. These factors collectively

degrade signal fidelity, particularly at high frequencies where timing precision becomes critical.

As illustrated in Fig. 2.1 (a) and (b), the ENOB decreases as signal frequency increases, reflecting the inherent trade-off between bandwidth and resolution in conventional ADCs. Such limitations become increasingly restrictive in ultrafast optical systems, where preserving temporal accuracy during digitization is essential for subsequent signal processing.

In Fig. 2.1 (b), the time-stretch technique mitigates these issues by slowing down the signal before digitization, effectively reducing the impact of aperture jitter and comparator ambiguity.

Fig. 2.1 (c) and (d) further examine the effects of clock jitter on high-frequency signal sampling: Fig. 2.1 (c): Even minor jitter causes significant errors in sampled amplitudes, degrading signal accuracy. Fig. 2.1 (d): Time-stretching decelerates the signal, significantly reducing the influence of clock jitter while also relaxing comparator speed requirements. Additionally, time-stretch ADCs are versatile, supporting both burst-mode and continuous data acquisition, making them ideal for ultrafast detection applications [41].

A major challenge in high-speed real-time measurements is the limited photon collection efficiency [46]. This issue is addressed through distributed amplification, achieved via stimulated Raman scattering within the same dispersive optical medium used for time stretching (typically a dispersive fiber) [47]. Alternatively, discrete amplifiers can be used to further enhance signal strength, as demonstrated in later sections of this thesis.

Originally designed for real-time ADC conversion with femtosecond temporal resolution, the amplified time-stretch technique has since been adapted for a wide range of applications, including spectroscopy and advanced imaging systems [48].

2.1.2 Mathematical Foundation for Achieving Photonic Time Stretch

In this thesis, photonic time stretch is implemented within a photonic experimental system using a mode-locked laser (MLL) as the light source. The MLL generates ultrashort optical pulses, produced through mode-locking, a mechanism that forces many longitudinal cavity modes to oscillate with a fixed phase relationship. This phase coherence causes constructive interference at regular intervals, forming periodic pulses with extremely short durations (typically femtoseconds to picoseconds) and broad optical spectra. This section establishes the theoretical framework for the propagation of ultrashort pulses in optical fibers, detailing the key principles governing their dispersion and evolution.

To quantitatively describe the time-stretch process and the wavelength–time mapping mechanism employed throughout this thesis, it is necessary to establish the mathematical framework governing ultrashort pulse propagation in dispersive media. The following derivation outlines the fundamental relationship between the optical pulse envelope, dispersion, and temporal stretching, which forms the theoretical basis of the photonic time-stretch system used in later chapters.

An ultrashort electromagnetic wave $G(t)$ can be mathematically described as the product of a plane-wave carrier and an envelope function $A(t)$, such that [49, 50].

$$G(z,t) = A(t)E_0 e^{i(\omega t - kz + \phi)} \tag{2-2}$$

Since mode-locked lasers typically exhibit a Gaussian temporal power distribution, the corresponding ultrashort optical pulse can be modeled with a Gaussian envelope as:

$$A(t) = Ae^{-\Gamma t^2} \tag{2-3}$$

where A represents the pulse amplitude, and the envelope is defined by the

Gaussian function $e^{-\Gamma t^2}$. Here, Γ is a parameter that can have both real and complex components. The real part, Γ_1, is inversely proportional to the pulse duration τ and determines the temporal width of the pulse. Here, τ denotes the temporal full-width at half-maximum (FWHM) of the Gaussian pulse envelope. The imaginary component governs the time-dependent phase shift $\Phi(t)$, influencing the pulse's spectral properties.

The phase shift $\Phi(t)$ affects the instantaneous frequency of the pulse, $\omega(t)$, which is given by:

$$\tau = \sqrt{\frac{2\ln 2}{\Gamma_1}} \tag{2-4}$$

$$\omega(t) = \frac{d\Phi(t)}{dt} = \omega_0 + 2\Gamma_2 t \tag{2-5}$$

In our laboratory, ultrashort optical pulses are generated using a commercial mode-locked laser (MLL), which produces pulses with a temporal duration of approximately 800 femtoseconds (fs) at a repetition rate of 50 MHz. Mode locking (ML) is a fundamental optical technique that enables a laser to emit intense, ultrashort pulses. This is achieved by establishing a fixed phase relationship among the longitudinal modes within the laser cavity. The constructive interference of these modes results in a coherent train of laser pulses. Following pulse generation, the ultrashort optical pulse is temporally stretched using a dispersive compensation fiber (DCF) [51]. A DCF is a specially engineered optical fiber that provides large negative chromatic dispersion through tailored refractive-index and waveguide design. When placed after standard single-mode fiber, it counteracts the accumulated positive dispersion and re-compresses broadened pulses, enabling effective dispersion management in optical links. This temporal stretching is a crucial step in facilitating the implementation of photonic time-stretch techniques, enabling high-speed signal processing and ultrafast detection applications.

Assuming that the laser-emitted pulse exhibits a Gaussian temporal profile $A(t)$, its corresponding Fourier transform $G(\omega)$ can be analytically derived [52, 53].

$$A(t) = A \cdot \exp\left(-\frac{t^2}{2\tau^2}\right) \tag{2-6}$$

$$G(\omega) = \tau\sqrt{2\pi}A \cdot \exp\left(-\frac{\tau^2\omega^2}{2}\right) \tag{2-7}$$

Where the parameter A represents the pulse amplitude, while τ denotes the Full-Width at Half Maximum (FWHM) of the Gaussian pulse. This τ is identical to the pulse-duration parameter introduced in Eq. (2.4). For the implementation of photonic time-stretching, Dispersive Fourier Transformation (DFT) [51]—also known as real-time Fourier transformation or frequency-to-time mapping—is employed. DFT uses large chromatic dispersion to convert the pulse's spectrum into a time-stretched waveform, enabling real-time spectral analysis without digital computation. In DFT, strong chromatic dispersion converts the spectrum of a broadband ultrashort optical pulse into a temporally stretched waveform.

The concept of DFT originates from the analogy between spatial Fraunhofer diffraction and temporal chromatic dispersion. Fraunhofer diffraction describes the far-field regime in which the diffraction pattern is the Fourier transform of the input field. There exists a well-established duality between far-field diffraction of a light beam through a thin lens and temporal pulse propagation in a dispersive medium under the second-order dispersion approximation. When a transform-limited ultrashort optical pulse propagates through a highly dispersive medium, satisfying the temporal far-field condition, the stretched pulse adopts an intensity envelope that mirrors the optical power spectrum of the original pulse.

The principle of DFT can be intuitively understood through the dispersion-stretching effect: Chromatic dispersion introduces a frequency-dependent linear

time delay to the input optical pulse. Hence, with sufficient dispersion, the spectral components of the broadband pulse become fully separated in time, creating a one-to-one mapping between the frequency domain and time domain. A schematic diagram illustrating the concept of DFT is shown in Fig. 2.2.

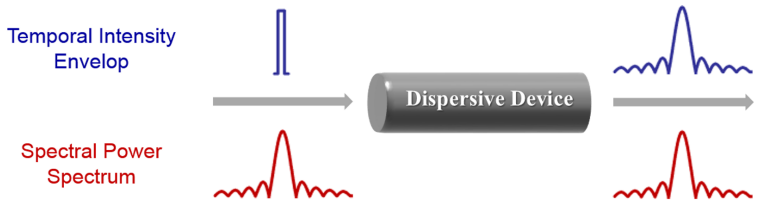

Fig. 2.2: Schematic Diagram of the Dispersive Fourier Transformation Process in a Dispersive Medium.

A dispersive element can be modeled as a linear time-invariant (LTI) system, defined by a transfer function that dictates its behavior during the transformation process, as expressed below:

$$H(\omega) = |H(\omega)| \exp\left[-j\Phi(\omega)\right] \tag{2-8}$$

where $H(\omega)$ and $\Phi(\omega)$ represent the magnitude and phase response of the dispersive element at an angular frequency ω, respectively. The phase response $\Phi(\omega)$ can be expanded using a Taylor series.

Under the second-order dispersion approximation, where higher-order phase terms are neglected within the spectral bandwidth of interest, the transfer function and its corresponding impulse response can be expressed as follows:

$$H(\omega) \cong |H(\omega)| \exp\left(-j\Phi_0\right) \exp\left(-j\dot{\Phi}_0\omega\right) \exp\left(-j\frac{1}{2\ddot{\Phi}_0}\omega^2\right) \tag{2-9}$$

$$h(t) = \widetilde{\mathcal{F}}^{-1}\left[H(\omega)\right] \propto \exp\left[j\frac{1}{2\ddot{\Phi}_0}(t-\dot{\Phi}_0)^2\right] \tag{2-10}$$

where $\dot{\Phi}_0$ represents the group delay, and $\ddot{\Phi}_0$ denotes the second-order dispersion, also referred to as Group Velocity Dispersion (GVD).

Let $x(t)$ and $y(t)$ represent the complex envelopes of the input and output optical pulses, respectively, for a dispersive element characterized by an impulse response $h(t)$. If the dispersive device has a sufficiently wide bandwidth that fully encompasses the entire spectrum of the input optical pulse, the output pulse can be expressed in terms of the input pulse through a convolution operation:

$$y(t) = x(t) * h(t) \tag{2-11}$$

By substituting the impulse response from the equation above, the output pulse can be expressed as:

$$\begin{aligned} y(t) &= \int_{-\infty}^{+\infty} x(t')h(t-t')dt' \propto \int_{-\infty}^{+\infty} x(t') \exp\left[j\frac{1}{2\ddot{\Phi}_0}(t-t')^2\right] dt' \\ &\propto \exp\left(j\frac{t^2}{2\ddot{\Phi}_0}\right) \int_{-\infty}^{+\infty} x(t') \exp\left(j\frac{1}{2\ddot{\Phi}_0}t'^2\right) \exp\left(-j\frac{1}{\ddot{\Phi}_0}tt'\right) dt' \end{aligned} \tag{2-12}$$

Here, the constant time delay $\dot{\Phi}_0$ is omitted to focus solely on the pulse broadening effect induced by dispersion. We assume the incident pulse has a finite pulse width Δt_0.

If the dispersion is sufficiently large, satisfying the condition:

$$\left|\frac{\ddot{\Phi}_0}{(\Delta t_0)^2}\right| \gg 1 \tag{2-13}$$

This is commonly known as the temporal Fraunhofer approximation, the stretched pulse can be further approximated as [54]:

$$
\begin{aligned}
y(t) &\propto \exp\left(j\frac{t^2}{2\ddot{\Phi}_0}\right)\int_{-\infty}^{+\infty} x(t')\exp\left(-j\frac{t}{\ddot{\Phi}_0}t'\right)dt' \\
&\propto \exp\left(j\frac{t^2}{2\ddot{\Phi}_0}\right)X(\omega)\Big|_{\omega=\frac{t}{\ddot{\Phi}_0}}
\end{aligned}
\tag{2-14}
$$

where $X(\omega) = \widetilde{\mathcal{F}}[x(t)]$ represents the Fourier transform of the input pulse.

The equation above clearly shows that the output temporal pulse envelope is directly proportional to the input pulse spectrum, with an additional phase factor. This establishes the principle of Dispersive Fourier Transformation (DFT), also known as dispersion-induced frequency-to-time mapping.

The equation serves as the theoretical foundation for standard DFT, which relies on the second-order dispersion approximation. Under this approximation: a unique, linear one-to-one mapping is established between optical frequency and time. This mapping is enabled by the linear group delay response with respect to frequency. Higher-order dispersion effects, if present, may introduce deviations from this ideal mapping, affecting the accuracy of DFT-based measurements. Higher-order dispersion refers to third-order and higher-order dispersion terms that produce nonlinear variations in group delay with optical frequency, leading to temporal distortions of the stretched waveform.

When higher-order dispersion is taken into account, the frequency-to-time mapping remains valid as long as the temporal Fraunhofer approximation is satisfied [55, 56]. However, due to the frequency-dependent nature of higher-order group delay, the mapping relationship becomes nonlinear. In this case, a modified nonlinear mapping function is required to accurately account for the effects of higher-order dispersion [57]:

$$
\omega = \frac{t}{\ddot{\Phi}_0} - \sum_{k=3}^{\infty}\left[\frac{\Phi_0^{(k)}}{(k-1)!(\ddot{\Phi}_0)^k}t^{k-1}\right] \tag{2-15}
$$

where $\Phi_0^{(k)}$ is the kth-order dispersion coefficient.

This section has presented the mathematical modeling of pulse propagation in dispersive media, describing how ultrashort optical pulses evolve under dispersion. It also introduces key parameters such as GVD and higher-order dispersion coefficients, which influence the accuracy of the time-stretch process. By applying these principles, PTS enables high-throughput detection across various applications, including real-time spectroscopy, biomedical imaging, and optical communication, making it an essential tool for capturing and processing ultrafast events. In the next section, we will present examples of PTS applications across various research fields.

2.1.3 Photonics Time Stretch Enables High-Throughput Detection and Ultrafast Optics

The PTS technique has revolutionized high-throughput and real-time measurement, addressing the limitations of traditional instruments in capturing ultrafast signals. By slowing down optical signals for detailed analysis, PTS has become an essential tool across various disciplines. Its applications span high-speed measurement and detection technologies, including ultrafast optical cameras, optical imaging, LiDAR, and medical diagnostics [24, 58, 59]. In this section, I will explore the applications of PTS across various research fields.

In flow cytometry, a major challenge lies in achieving the speed and sensitivity required to analyze thousands to millions of cells efficiently using current optical imaging technologies [60]. While these technologies are highly optimized for single-cell analysis and play a crucial role in modern biology and clinical diagnostics, their scalability remains limited.

The adoption of PTS has emerged as a promising approach to overcoming the limitations of conventional optical imaging technologies. As illustrated in

Fig. 2.3, PTS enables ultrahigh-throughput optofluidic single-cell imaging, achieving throughput rates 1–2 orders of magnitude higher than traditional imaging flow cytometers, with the ability to analyze up to 100,000 cells per second [61].

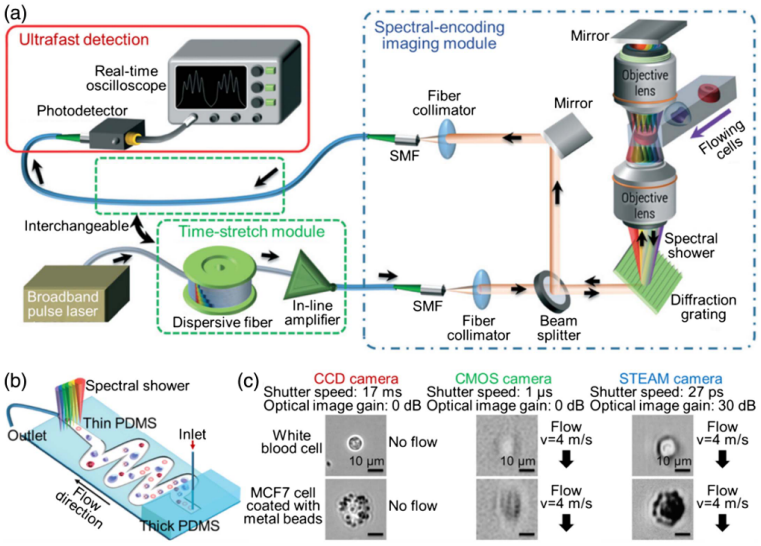

Fig. 2.3: Optofluidic time-stretch imaging system. (a) System architecture of STEAM. (b) Microfluidic channel configuration for single-cell imaging using spectrally encoded illumination. (c) Comparison of CCD, CMOS, and STEAM imaging, showing that STEAM enables blur-free imaging of cells at high flow speeds due to its ultrashort effective shutter time [61].

Moreover, this technique facilitates the quantification of intrinsic biophysical markers at the single-cell level—an underexplored class of cellular signatures that exhibit strong correlations with commonly studied biochemical markers. This unique capability significantly broadens the scope of cellular analysis and diagnostic applications, offering new insights into single-cell characterization.

PTS imaging is widely used for high-speed, high-throughput applications such as cell screening [62], but its practical implementation faces challenges due to the massive data burden. To address this, a Fourier-domain-compressed PTS imaging system with low-pass filtering is proposed, shown as Fig. 2.4, significantly simplifying the setup by eliminating the need for complementary dispersive media and optical amplifiers. This reduces signal-to-noise ratio (SNR) degradation while

maintaining image quality.

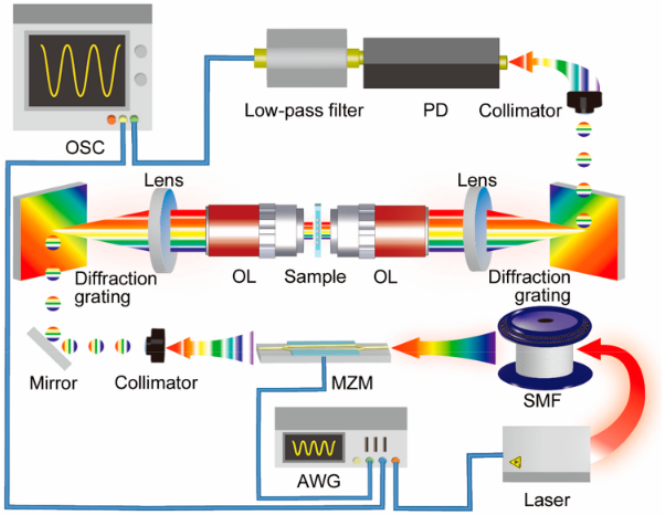

Fig. 2.4: Experimental setup of the all-optical Fourier-domain-compressed time-stretch imaging system with low-pass filtering. OSC: oscilloscope; PD: photodetector; MZM: Mach–Zehnder modulator; AWG: arbitrary waveform generator; SMF: single-mode fibre; OL: objective lens [62].

Experimental validation demonstrates high-resolution imaging of flowing cells at 1 m/s with 80% data compression, achieving similar performance to conventional methods while reducing data volume for real-time processing. The system is adaptable across different wavelengths and can be further optimized with balanced photodetection to improve compression efficiency. This innovation enhances the scalability of OTS imaging, making it more practical for large-scale single-cell analysis and real-time imaging applications.

Photonics time-stretch has emerged as a key enabler for high-speed LiDAR (Light Detection and Ranging), particularly in robotics and 3D imaging [63]. In Fig. 2.5, a spectrally scanned time-of-flight (ToF) LiDAR system has been developed, achieving 1 MHz single-shot imaging and inertia-free scanning using a single laser and detector. Two implementations: a gain-switched supercontinuum source (1,550 nm) and a Fourier-domain mode-locked (FDML) laser (1,060 nm). FDML laser is a wavelength-swept laser in which the tunable filter inside the laser

cavity is synchronized with the round-trip time of the optical signal in a long fiber delay line. This synchronization enables rapid and continuous wavelength sweeping with high stability and narrow instantaneous linewidth, making FDML lasers particularly suitable for high-speed imaging and sensing applications such as LiDAR and optical coherence tomography.

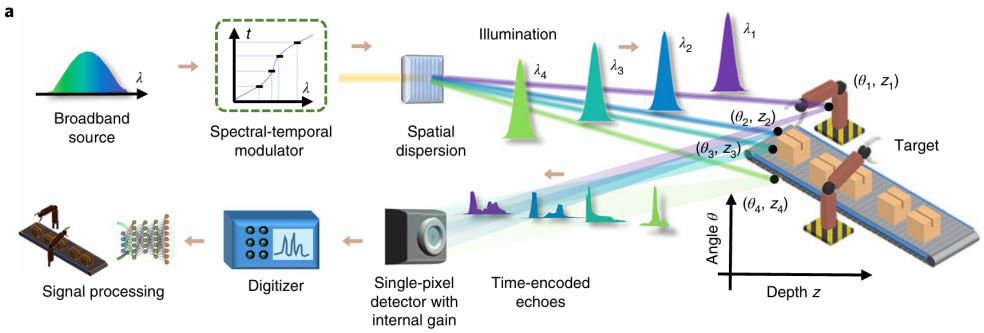

Fig. 2.5: PTS-based spectrally scanned time-of-flight (ToF) LiDAR system. In this implementation, PTS generates a spectro-temporally encoded pulse train in which different wavelengths illuminate different angular positions, while depth information is encoded in the temporal delay of the returned echoes [63].

The system utilizes spectro-temporal encoding for potential 2D imaging and can be enhanced with optical dynamic range compression to extend detection range. Future improvements, such as bandwidth expansion, pulse optimization, and spectral multiplexing, could further boost performance. This approach demonstrates the potential of photonics time-stretch technology to revolutionize high-speed, adaptive LiDAR systems for robotics and advanced imaging applications.

PTS-OCT enables real-time, high-speed imaging, but its massive data volumes present a significant challenge [64, 65]. To address this, a photonic compressive sensing approach is proposed, shown as Fig. 2.6 leveraging spectral sparsity to achieve a 66% data compression ratio, enabling high-throughput OCT at a 1.51-MHz scan rate with a reduced 50 MS/s sampling rate [64].

Further optimization using a Gaussian-shaped analog random bit sequence

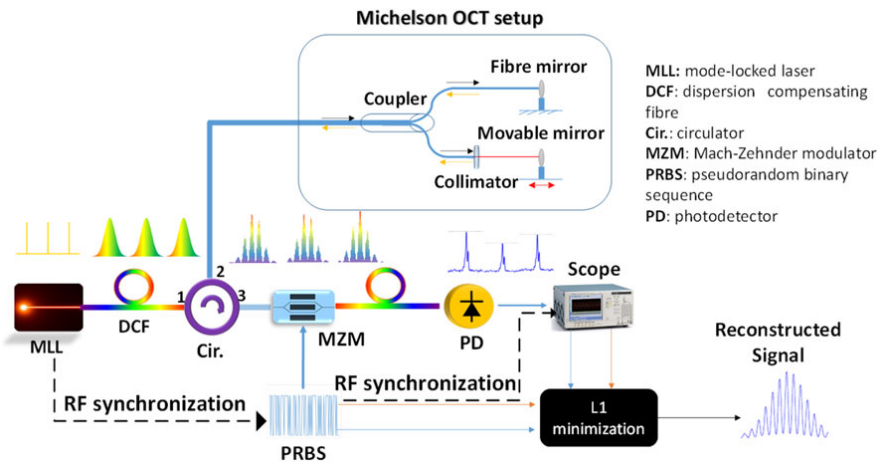

Fig. 2.6: Block diagram of the compressive sensing PTS-OCT system. A broadband pulse from a mode-locked laser (MLL) is first time-stretched by dispersion compensating fibre (DCF) and sent to a Michelson interferometer for spectral-domain OCT measurement. The time-encoded signal is then modulated by a pseudorandom binary sequence (PRBS) using a Mach–Zehnder modulator (MZM), followed by optical integration via opposite dispersion fibre. The compressed measurements are detected by a photodetector (PD) and reconstructed using ℓ_1 minimization[64].

enhances compression efficiency by an additional 10%, while a dual-pulse integration method improves frequency resolution without increasing data requirements in [64]. Additionally, primal-dual interior point optimization proves most effective for accurate and efficient OCT signal reconstruction. This method reduces data processing demands and enhances measurement resolution and scalability, advancing high-speed OCT applications.

Time-stretch imaging has proven effective for high-throughput phenotypic screening, but its application to solid-substrate assays and biomolecular specificity has been limited. To address this, a spinning time-stretch imaging platform is developed, shown as Fig. 2.7, integrating ultrafast line-scan imaging ($> 10\,\text{MHz}$) with a functionalized DVD disc for real-time analysis of adherent cell cultures and biochemically specific assays [66].

By leveraging wavelength-swept laser pulses through a dispersive fiber and

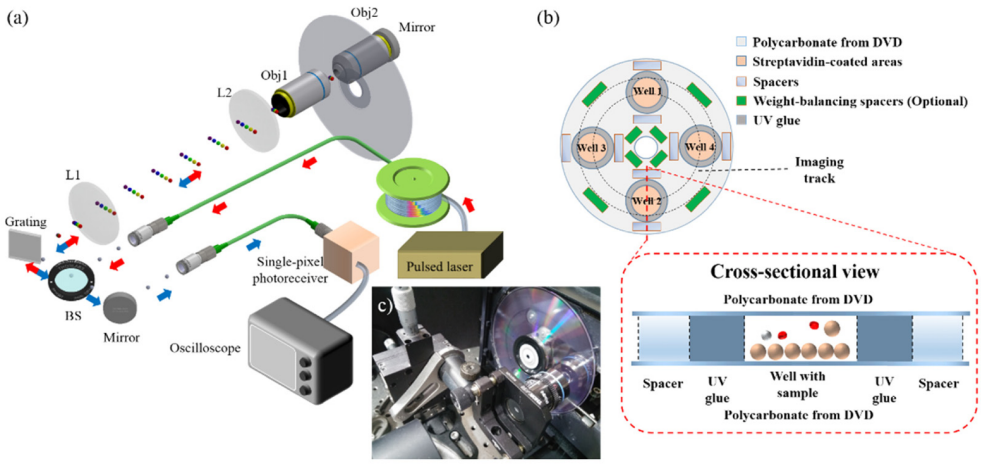

Fig. 2.7: Spinning time-stretch imaging platform based on a modified DVD. (a) Optical setup of the time-stretch imaging system, where broadband pulses are stretched in dispersive fibre and spectrally encoded into a line-scan beam using a diffraction grating and relay optics to scan the spinning DVD, with detection by a single-pixel photoreceiver. (b) Functionalized DVD assay platform with multiple wells on a double-layer polycarbonate disc forming enclosed chambers for cell culture or cell-capture assays [66].

high-speed DVD spinning, this system achieves an imaging throughput of 100,000 – 1,000,000 cells per second, surpassing traditional automated microscopy, which is constrained by camera frame rates and stage-scanning speeds. Additionally, it overcomes resolution-FOV trade-offs inherent in optical microscopy, enabling high-resolution imaging across an ultra-large field of view. This innovation significantly advances high-throughput cell imaging and screening technologies.

2.1.4 Summary

This section introduces the theoretical model and principles of PTS. The model demonstrates how ultrafast optical pulses propagate and undergo dispersion through a dispersive element, utilizing Dispersive Fourier Transformation to establish a wavelength-to-time mapping.

Additionally, we explore various applications of PTS in fields such as optical imaging, LiDAR, and medical diagnostics. However, despite its advantages,

existing PTS applications still struggle to meet the demands of high-throughput detection and real-time processing.

To overcome these limitations, this work focuses on machine learning-based approaches to enhance high-throughput detection capabilities. The next section provides a detailed discussion on machine learning techniques and their role in addressing this challenge.

2.2 Machine Learning

2.2.1 Machine Learning overview

Machine learning provides computational models capable of extracting patterns from data and performing prediction or classification tasks. In high-throughput optical systems, machine learning is particularly useful for processing the large volumes of time-sequential data generated by photonic time-stretch systems. Among the various machine learning paradigms, supervised learning is the primary focus of this thesis, since reservoir computing is typically implemented within this framework.

In supervised learning, a model is trained using labeled data to learn the mapping between inputs and desired outputs. Once trained, the model can generalize to unseen data by identifying patterns learned during training. Machine learning techniques can be broadly categorized into three main types, depending on the specific requirements of the task:

A: Supervised Learning

- Supervised learning aims to establish a mapping between input data ("observations") and a target variable ("labels") [67]. The model utilizes features extracted from the input data ("feature vectors") to predict the corresponding labels. Learning is considered successful or generalized when the model can reliably predict labels for previously unseen data.

Supervised learning is broadly classified into two categories: Classification, where labels are discrete (e.g., identifying spam emails or diagnosing diseases); Regression – where labels are continuous (e.g., predicting house prices or stock market trends).

As the most widely used form of machine learning, supervised learning is applied across diverse fields, from healthcare and finance to natural language processing and computer vision. Common algorithms include: Nearest Neighbor, Naïve Bayes, Decision Trees, Support Vector Machines (SVMs), and Neural Networks [68, 69].

B: Unsupervised learning

- In some cases, the objective is to identify hidden structures within a dataset rather than predict specific outcomes. These scenarios fall under unsupervised learning, where data points lack explicit labels. Unsupervised learning is particularly valuable for tasks such as clustering and dimensionality reduction [70].

  A common clustering example is an online retailer analyzing historical sales data to segment customers into distinct market groups. This segmentation enables targeted advertising campaigns and personalized recommendations. On the other hand, dimensionality reduction techniques serve as preprocessing tools for supervised learning, helping to: Select relevant features, Compress input data to speed up model training, and Visualize high-dimensional datasets in a lower-dimensional space.

  Popular unsupervised learning algorithms include: Clustering: k-means and Gaussian Mixture Models (GMMs) [71]. Dimensionality Reduction: Principal Component Analysis (PCA), t-SNE, and Autoencoders [72, 73].

C: Reinforcement Learning:

- Reinforcement learning (RL) is another learning paradigm in which an agent interacts with an environment and learns optimal actions through reward-based feedback. Although RL has achieved success in areas such as robotics and control systems, it is not directly relevant to this thesis and will not be discussed further [74] [75] [76, 77].

In some cases, different learning paradigms can be combined to improve performance, commonly referred to as hybrid learning approaches. Hybrid learning approaches combine elements of different learning paradigms, such as supervised and unsupervised learning, to leverage both labeled and unlabeled data. A common example is semi-supervised learning, where a small labeled dataset is used alongside a larger unlabeled dataset to improve generalization performance. While hybrid strategies can enhance learning efficiency in certain applications, they are beyond the scope of this work.

This thesis primarily focuses on supervised learning techniques, where prior knowledge of the correct output is available. Supervised learning typically involves optimizing a set of weights, but to prevent overfitting (which often manifests as excessively large weights), regularization techniques are applied—these will be discussed in subsequent sections.

Among supervised learning models, neural network architectures have become particularly prominent due to their strong representation capability.

2.2.2 Artificial Neural Network (ANN)

Artificial Neural Networks (ANNs) are computational models composed of interconnected processing units designed to approximate complex nonlinear mappings between inputs and outputs [78]. Owing to their strong representation capability, ANNs have achieved remarkable success in classification and regression tasks.

An ANN typically consists of an input layer, one or more hidden layers, and an output layer. Each neuron performs a weighted summation of its inputs followed

by a nonlinear activation function. During training, the connection weights are optimized to minimize prediction error.

Fig. 2.8 illustrates the analogy between biological neurons and artificial neurons. In artificial neural networks, nodes process incoming signals, connections transmit information, and weights determine the strength of influence between neurons.

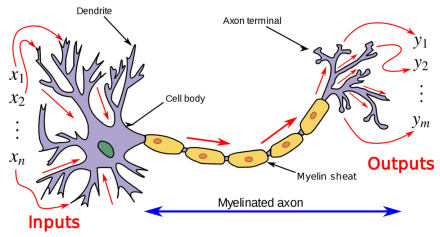

Fig. 2.8: Neuron and Myelinated Axon: Signal flow from dendritic inputs to axon terminals. Nodes (neurons) process incoming data, links (synapses) transmit signals, and weights determine the strength of influence between nodes.

Based on their connectivity structure, neural networks can be broadly categorized into feedforward neural networks (FFNNs) and recurrent neural networks (RNNs).

In FFNNs, information flows unidirectionally from the input layer to the output layer without feedback connections, as shown in Fig. 2.9. Due to this acyclic structure, FFNNs are well suited for static mapping tasks but lack intrinsic memory mechanisms for modeling temporal dependencies.

In contrast, RNNs introduce feedback connections that allow hidden states to depend on previous time steps, enabling the modeling of temporal dynamics and sequential correlations.

Although RNNs are powerful for sequential data processing, they are typically trained using backpropagation through time (BPTT). Repeated multiplication of weight matrices across time steps may lead to vanishing or exploding gradients, which limits the learning of long-range dependencies [79]. While gated variants

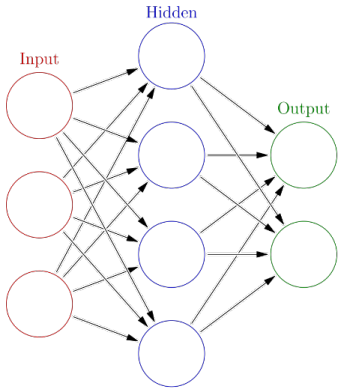

Fig. 2.9: Typical feedforward neural network structure. Information flows strictly from input to output without feedback connections.

such as LSTM and GRU alleviate these issues, training complexity remains significant.

These limitations motivate the exploration of simplified recurrent frameworks for temporal processing.

2.3 Reservoir Computing

2.3.1 Introduction to Reservoir Computing

ANNs are broadly categorized into two main types: FFNNs and RNNs [80]. FFNNs are the most widely studied and utilized type of neural network. They consist of three primary components: an input layer, one or more hidden layers (intermediate layers), and an output layer. The defining characteristic of FFNNs is their unidirectional flow of information, where data moves strictly from the input layer to the output layer without feedback loops. Due to this acyclic structure, FFNNs are relatively simple to train, computationally efficient, and well suited for static mapping tasks such as classification and regression problems, including image recognition and tabular data analysis [81]. However, FFNNs do not possess an internal memory mechanism and therefore cannot naturally model temporal

dependencies or sequential data.

In contrast, Recurrent Neural Networks (RNNs) incorporate feedback connections that allow hidden states to depend on previous time steps, enabling the modeling of temporal dynamics and sequential information [82]. This makes RNNs particularly suitable for time-series prediction, speech recognition, and natural language processing. Nevertheless, conventional RNNs often suffer from issues such as vanishing and exploding gradients during training, which can limit their ability to capture long-range dependencies. Variants such as Long Short-Term Memory (LSTM) and Gated Recurrent Units (GRU) were developed to mitigate these limitations [80]. Fig. 2.10a illustrates a simple feedforward neural network with a single hidden layer.

Unlike FFNNs, RNNs introduce feedback loops, allowing hidden states to be updated recursively based on both the current input and previous hidden states. This recurrent structure enables the network to maintain an internal memory of past information, making it capable of modeling temporal dependencies and sequential correlations in time-series or language data. The feedback connections within RNNs, as shown in Fig. 2.10b, enable them to model dependencies between inputs and outputs over time. Mathematically, RNNs can be viewed as nonlinear dynamical systems in which the hidden state evolves over time according to a state transition function [83]. This capability makes RNNs particularly suitable for tasks requiring memory, such as speech recognition, time-series prediction, and language modeling. However, standard RNNs may suffer from vanishing or exploding gradient problems during training, which can hinder learning of long-range dependencies [79]. To address this limitation, architectures such as Long Short-Term Memory (LSTM) and Gated Recurrent Units (GRU) introduce gating mechanisms to regulate information flow and preserve long-term context.

Despite their advantages, RNNs are typically trained using gradient-based optimization methods, most commonly backpropagation through time (BPTT) [84].

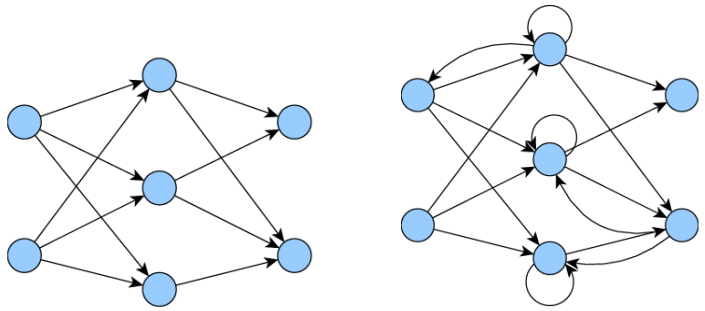

Fig. 2.10: Comparison between feedforward and recurrent neural network architectures. (a) Feedforward neural network (FFNN), where information flows strictly from input to output without feedback connections. (b) Recurrent neural network (RNN), where hidden states are connected across time steps through recurrent feedback loops, allowing the network to retain information from previous inputs and model temporal dependencies.

In BPTT, the recurrent network is unfolded across time steps to form an equivalent deep feedforward structure, and gradients are computed by applying standard backpropagation through this temporal unfolding. The gradients are then accumulated across time to update shared parameters. However, because the same weights are repeatedly multiplied across many time steps, the gradient signals can either decay exponentially (vanishing gradients) or grow uncontrollably (exploding gradients), making it difficult to learn long-range temporal dependencies.

To address these limitations, this work focuses on an alternative approach: reservoir computing. In this method, the internal RNN parameters are not trained but are instead configured to operate within an appropriate dynamical regime. Only the readout layer is trained, simplifying implementation and facilitating hardware applications.

The next section delves into the origins, theory, and practical applications of reservoir computing.

2.3.2 Principle of Reservoir Computing

Reservoir Computing (RC) was developed to simplify the training process for Recurrent Neural Networks (RNNs) in supervised learning tasks [85]. Traditional RNNs require training all network weights, including input, recurrent, and output connections, which leads to significant computational complexity. They are typically optimized using gradient-based methods, such as stochastic gradient descent (SGD), where the gradients of a loss function are iteratively used to update the model parameters [86].

RC addresses this limitation by keeping the internal reservoir weights fixed and training only the readout layer, thereby significantly reducing training complexity. RC was independently introduced in the early 2000s through two primary models:

- Echo State Networks (ESNs) – Proposed by Herbert Jaeger in 2001 [87], focusing on an engineering-oriented approach. ESNs utilize a randomly initialized RNN with a topology designed to satisfy the echo state property, ensuring past inputs gradually fade over time.
- Liquid State Machines (LSMs) – Introduced by Wolfgang Maass in 2002 [88], emphasizing biological plausibility and its application in neuroscience and robotics.

In both models, input signals are projected into a high-dimensional reservoir, where complex temporal dynamics are generated before being interpreted by a simple linear readout layer. A typical RC system consists of three main components: an input layer, a dynamic reservoir, and a readout layer, as illustrated in Fig. 2.11. The input layer projects external signals into a high-dimensional nonlinear reservoir composed of recurrently connected nodes. Within the reservoir, the internal states evolve according to fixed recurrent connections, generating rich temporal dynamics that transform the input into a higher-dimensional representation. Importantly, the reservoir weights remain fixed after initialization and are not trained. Only the linear readout layer is optimized, typically using simple

linear regression or ridge regression. This separation between dynamic state generation and output learning significantly reduces training complexity and makes RC particularly suitable for hardware implementation and real-time processing.

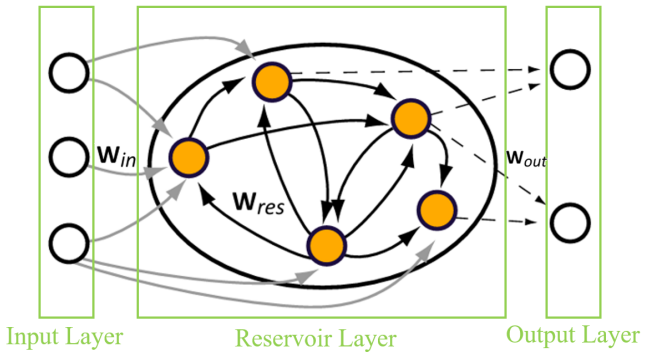

Fig. 2.11: Schematic Representation of a Reservoir Computing System. Input Layer: Feeds the input signal into a nonlinear dynamical system (the reservoir); Reservoir layer: A fixed recurrent neural network (RNN) with random, untrained weights that captures temporal dependencies; Output Layer: A trainable linear layer that maps the reservoir's states to the desired output.

Fig. 2.11 provides a schematic representation of a RC system. The input signals are injected into all or a subset of reservoir nodes, which are randomly interconnected through recurrent connections. The resulting reservoir states are then propagated to the output layer, as indicated by the dashed arrows in the figure.

Each connection in the system is associated with a weight, organized into weight matrices denoted as $\mathbf{W}$. During training, only the output layer weights—those connecting the reservoir states to the output layer—are updated, while all other weights within the reservoir remain fixed. This approach simplifies training while preserving the system's ability to process complex temporal patterns.

Echo State Networks (ESNs) are a specialized form of Recurrent Neural Networks (RNNs) used for supervised temporal machine learning tasks [89]. Given a training dataset, where the input signal $\mathbf{u}(n) \in \mathbb{R}^{N_u}$ corresponds to a desired

target output $\mathbf{y}^{\text{target}}(n) \in \mathbb{R}^{N_y}$, the goal is to train a model that generates an output signal $\mathbf{y}(n)$ that closely approximates $\mathbf{y}^{\text{target}}(n)$ while generalizing effectively to unseen data.

The model is optimized by minimizing an error measure, typically the Mean-Square Error (MSE) or the Root-Mean-Square Error (RMSE), providing a quantitative evaluation of performance. The Normalized RMSE (NRMSE) further normalizes the error based on the variance of the target signal, ensuring scale-invariance.

$$E(y, y^{\text{target}}) = \frac{1}{N_y} \sum_{i=1}^{N_y} \sqrt{\frac{1}{T} \sum_{n=1}^{T} \left(y_i(n) - y_i^{\text{target}}(n) \right)^2} \tag{2-16}$$

The RMSE is averaged over the N_y dimensions i of the output. To make the error metric scale-independent, RMSE is normalized by dividing it by the variance of the target signal $\mathbf{y}^{\text{target}}(n)$, resulting in the NRMSE.

The NRMSE provides an absolute measure of error, unaffected by the arbitrary scaling of $\mathbf{y}^{\text{target}}(n)$. A value of 1 is obtained if the output $\mathbf{y}(n)$ is a constant set to the mean of $\mathbf{y}^{\text{target}}(n)$, indicating a baseline performance. For a well-performing model of a stationary process, the NRMSE typically falls between 0 and 1.

The normalization and square root components enhance interpretability, ensuring comparability across datasets. Notably, minimizing the NRMSE also minimizes the unnormalized MSE, provided no additional penalties or weighting terms are introduced.

ESNs typically employ leaky-integrated, discrete-time neurons with continuous activation values, where the reservoir update equations are:

$$\tilde{\mathbf{x}}(n) = \tanh\left(\mathbf{W}^{\text{in}}[1; \mathbf{u}(n)] + \mathbf{W}\mathbf{x}(n-1) \right) \tag{2-17}$$

$$\mathbf{x}(n) = (1 - \alpha)\mathbf{x}(n-1) + \alpha\tilde{\mathbf{x}}(n) \tag{2-18}$$

where $\mathbf{x}(n) \in \mathbb{R}^{N_x}$ represents the reservoir state vector, and $\tilde{\mathbf{x}}(n) \in \mathbb{R}^{N_x}$ is its update, both at time step n. The matrices $\mathbf{W}^{\text{in}} \in \mathbb{R}^{N_x \times (1+N_u)}$ and $\mathbf{W} \in \mathbb{R}^{N_x \times N_x}$ are the input and recurrent weight matrices, respectively. The parameter $\alpha \in (0, 1]$, known as the leaking rate, controls the degree of leaky integration, influencing the reservoir's memory and temporal dynamics. The function $\tanh(\cdot)$ is applied element-wise. While $\tanh(\cdot)$ is the most commonly used activation function, other sigmoid-like functions can also be employed.

In the special case where $\alpha = 1$, the leaky integration is effectively disabled, and the update simplifies to $\tilde{\mathbf{x}}(n) \equiv \mathbf{x}(n)$.

The network output is computed as:

$$y(n) = \mathbf{W}^{\text{out}}[1; \mathbf{u}(n); \mathbf{x}(n)] \tag{2-19}$$

where $\mathbf{W}^{\text{out}}$ is the only trainable parameter, obtained through linear regression to minimize the error between $\mathbf{y}(n)$ and $\mathbf{y}^{\text{target}}(n)$.

An additional nonlinearity can be applied to $\mathbf{y}(n)$, providing greater flexibility to the output function. Additionally, feedback connections $\mathbf{W}^{\text{fb}}$ from $(n-1)$ to $\tilde{\mathbf{x}}(n)$ can be introduced to enhance the model's temporal dynamics, allowing it to capture more complex dependencies over time.

Fig. 2.12 graphically represents an RC, illustrating its notation and training approach. The figure outlines the data processing procedure. In a typical RC, the first step involves generating a large random reservoir in the hidden layer. This is achieved by constructing a recurrent neural network with random input weights ($\mathbf{W}^{\text{in}}$), random recurrent weights ($\mathbf{W}$), and a defined leaking rate (α).

Once initialized, the network is trained using the input $\mathbf{u}(n)$, which drives the reservoir, producing activation states $\mathbf{x}(n)$. These states are then collected. In the readout layer, linear regression is applied to determine the output weight matrix $\mathbf{W}^{\text{out}}$ by minimizing the mean squared error (MSE) between the network output $y(n)$ and the target output $\mathbf{y}^{\text{target}}(n)$. During testing, the trained output weights

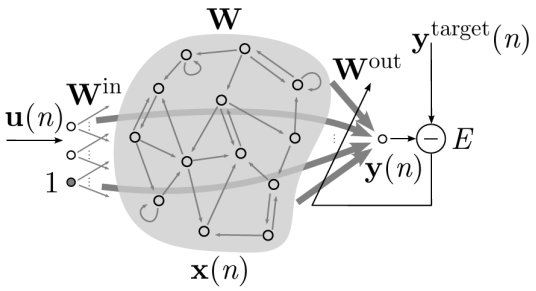

Fig. 2.12: Schematic of an Echo State Network (ESN). The input signal is projected into a randomly connected recurrent reservoir, where the internal states generate rich nonlinear temporal dynamics. The reservoir connections remain fixed, while only the output (readout) layer is trained. The network output is compared with a target signal to compute an error, which is used to update the readout weights.

$\mathbf{W}^{\text{out}}$ are applied to compute $y(n)$ for new input data $\mathbf{u}(n)$.

Designing an effective reservoir is critical for optimal performance. Key parameters such as the spectral radius, leaking rate, and echo state property must be carefully tuned to ensure stable and efficient dynamics.

2.3.3 Factors in Designing an Effective Reservoir Computing Structure

A: Spectral Radius and Stability

For a reservoir computing system to be effective in time-series computation, it must exhibit fading memory—a property ensuring that past inputs gradually lose their influence over time [90]. This can be achieved by appropriately scaling the reservoir weight matrix ($\mathbf{W}_{\text{res}}$) to maintain stability. Optimizing the spectral radius—the largest absolute eigenvalue of the weight matrix—is crucial for fine-tuning the reservoir's dynamic behavior.

The spectral radius ($\rho_{\mathbf{W}_{\text{res}}}$) determines the reservoir's stability and memory retention. It is defined as the largest absolute eigenvalue of the reservoir connection matrix. The closer the reservoir dynamics are tuned to the edge of stability ($\rho \approx 1$), the longer the system retains information about past inputs, optimizing

performance for many tasks [91]. The spectral radius determines the strength of feedback from previous reservoir states. If it is too small, past inputs quickly vanish and the reservoir loses memory; if it is too large, the dynamics may become unstable or chaotic. Hence, setting it near the edge of stability balances memory retention and stability, which is critical for time-series computation.

For neurons with a maximum gain of one, such as those using the tanh activation function, the spectral radius directly corresponds to the largest eigenvalue of the interconnection matrix $\mathbf{W}_{\text{res}}$. If the neuron gain differs from one, an upper bound for the spectral radius can be computed by incorporating the neurons' maximal gain function f.

Given a reservoir weight matrix $\mathbf{W}_{\text{res}}$ of size $n \times n$, with complex or real elements ($\mathbf{W}_{\text{res}} \in \mathbb{C}^{n \times n}$), and a diagonal matrix $\mathbf{G}_{\max}$ representing the neurons' maximum gain, an upper bound for the spectral radius is:

$$\rho_{\mathbf{W}_{\text{res}}} \leq \max_{1 \leq i \leq n} \left| \text{eig}_i \left(\mathbf{G}_{\max} \mathbf{W}_{\text{res}} \right) \right| \tag{2-20}$$

The spectral radius serves as an indicator of network stability: When $\rho > 1$, the network may become unstable, leading to unbounded activations. For zero input, instability always occurs if $\rho > 1$. For non-zero input, instability may occur when $\rho > 1$, but it depends on the system's actual gain at a given time. To ensure stability, the spectral radius is typically adjusted close to unity. In practice, slightly exceeding $\rho = 1$ may still provide optimal performance for some tasks [92].

B: Leaking Rate (α) in Reservoir Computing

The leaking rate (α) in reservoir nodes determines the speed of state updates in a discrete-time system. It can be interpreted as the rate at which the reservoir updates its dynamics, and it has a continuous-time counterpart expressed as an Ordinary Differential Equation (ODE):

$$\dot{\mathbf{x}} = -\mathbf{x} + \tanh\left(\mathbf{W}^{\text{in}}[1; \mathbf{u}] + \mathbf{W}\mathbf{x}\right) \tag{2-21}$$

Applying Euler's discretization to this ODE leads to:

$$\frac{\Delta x}{\Delta t} = \frac{x(n+1) - x(n)}{\Delta t} \approx \dot{x} \tag{2-22}$$

Through this discretization, α corresponds to the sampling interval (Δt) in the continuous domain, representing the time step between two consecutive updates in the discrete-time realization. The role of α is similar to resampling the input $\mathbf{u}(n)$ and target output $\mathbf{y}^{\text{target}}(n)$, particularly for slow signals. α can be adjusted dynamically to compensate for time warping in signals [93]. Instead of using α as a discrete sampling interval, it can also be introduced as a time constant ($\Delta t \equiv 1$) in Eq. (2-21).

While there are variations in how leaky integration is implemented [94], the standard formulation in Eq. (2-18) is widely preferred because it ensures that the reservoir state $x(n)$ remains bounded within $(-1, 1)$, preventing instability.

From a signal processing perspective, leaky integration in Eq. (2-18) can also be seen as a digital low-pass filter, commonly referred to as exponential smoothing. Some studies suggest replacing this simple filter with more advanced filtering techniques to refine the system's behavior [95].

C: Training Readouts and Ridge Regression

Since the readout layer in an ESN is typically linear and feedforward, its output can be expressed in matrix form as:

$$\mathbf{Y} = \mathbf{W}^{\text{out}}\mathbf{X} \tag{2-23}$$

where $\mathbf{Y} \in \mathbb{R}^{N_y \times T}$ contains all network outputs $\mathbf{y}(n)$, and $\mathbf{X} \in \mathbb{R}^{(1+N_u+N_x)\times T}$ includes all input and reservoir states $[1; \mathbf{u}(n); \mathbf{x}(n)]$, generated while presenting the reservoir with $\mathbf{u}(n)$.

To find the optimal output weights $\mathbf{W}^{\text{out}}$, we minimize the squared error between the network output $\mathbf{y}(n)$ and the target output $\mathbf{y}^{\text{target}}$. This corresponds to solving an overdetermined system of linear equations:

$$\mathbf{Y}^{\text{target}} = \mathbf{W}^{\text{out}}\mathbf{X} \tag{2-24}$$

A widely used approach for training the output weights is ridge regression (Tikhonov regularization), which provides a stable and universally applicable solution:

$$\mathbf{W}^{\text{out}} = \mathbf{Y}^{\text{target}}\mathbf{X}^{\top}\left(\mathbf{X}\mathbf{X}^{\top} + \beta\mathbf{I}\right)^{-1} \tag{2-25}$$

where β is a regularization coefficient, and $\mathbf{I}$ is the identity matrix, used to prevent overfitting by penalizing large weight values.

D: Readouts for Classification

This thesis primarily focuses on classification tasks, including basic waveform classification, frequency classification, and spoken-digit classification. For short time-series classification, the output $y(n)$ is structured such that each class corresponds to a specific output dimension. The target output $\mathbf{y}^{\text{target}}(n)$ is defined as 1 for the correct class and 0 for all other classes.

The predicted class is determined using the argmax function:

$$\text{class}(\mathbf{u}(n)) = \arg\max_k \left(\frac{1}{|\tau|}\sum_{n\in\tau} y_k(n)\right) = \arg\max_k \left((\Sigma y)_k\right) \tag{2-26}$$

A more efficient method refines the above equation using the time-averaged reservoir states Σ_x:

$$\Sigma_y = \frac{1}{|\tau|}\sum_{n\in\tau} y(n) = \mathbf{W}^{\text{out}}\Sigma_x \tag{2-27}$$

where Σ_x represents the time-averaged input and reservoir state vector over τ.

Instead of minimizing the error for each time step n, training can be optimized by minimizing the error between time-averaged values

$$E(\Sigma y^{\text{target}}, \Sigma y) \tag{2-28}$$

This allows individual $y(n)$ values to deviate from $\mathbf{y}^{\text{target}}(n)$ as long as their time-averaged counterpart Σy remains close to Σy^{target}. For short sequences, the target remains constant:

$$\mathbf{y}^{\text{target}} \equiv \Sigma \mathbf{y}^{\text{target}} = \mathbf{y}^{\text{target}}(n) = \text{const} \tag{2-29}$$

For long temporal sequences, such as detection and classification tasks, special considerations must be made for signal shape, duration, delays, and pattern formation in $\mathbf{u}(n)$.

2.3.4 Hardware Implementation of Reservoir Computing

The theoretical model and operating principles of Reservoir Computing (RC) have been outlined above. With its energy efficiency, high-speed processing, and real-time signal analysis capabilities, RC has become a powerful technique for time-series data processing, drawing significant research interest. As a result, various hardware implementations have been developed to enhance its performance and expand its applications across different fields, including Mechanical Reservoir Computing [96], Acoustic Reservoir Computing (ARC) [97], Electronic Reservoir Computing (ERC) [98], and Optoelectronic & Photonic Reservoir Computing (PRC) [99]. The following section provides a brief overview of these hardware-based advancements in RC.

Mechanical Reservoir Computing (MRC) utilizes mechanical devices, such as mechanical oscillators, as reservoirs in the hidden layer [100]. By leveraging the inherent physical dynamics for information processing, MRC significantly reduces

computational power consumption, making it highly energy-efficient. Additionally, since it relies on physical implementations rather than conventional electronic computation resources, it minimizes the demand for traditional computing infrastructure.

MRC has broad real-world applications, particularly in robotics and sensing. In robotics-based physical reservoir computing, the robot's body functions as a highly specific dynamical system, where observed states and dynamic transformations are crucial for task execution. This approach has been successfully applied in real-time robot control and optimization [100].

In sensing applications, MRC typically employs micro-mechanical devices that serve both sensing and computing functions. For instance, as demonstrated in [101], a delay-coupled electromechanical reservoir computing system utilizes a Duffing non-linear silicon beam as the computational medium, with virtual nodes multiplexed in time. This system enables accurate temporal input processing with minimal error rates, showcasing the potential of MRC in high-precision sensing and real-time data analysis.

Acoustic Reservoir Computing (ARC) leverages sound waves and acoustic propagation dynamics to implement reservoir computing. By utilizing sound propagation through physical media, ARC enables energy-efficient and robust time-series data processing [97].

In ARC, input signals such as audio and vibrations are encoded into an acoustic medium and transmitted into the reservoir layer. Within this layer, signals propagate through a complex medium, undergoing nonlinear transformations and temporal mixing. This inherent complexity enhances computational power while maintaining efficiency.

ARC has been explored in various experimental setups, including Acoustic Waveguides, Surface Acoustic Waves (SAW), and MEMS-Based Acoustic Reservoirs [102, 103]. For instance, in [102], a proof-of-concept SAW-based reservoir

computing system was introduced, utilizing electronic memory to simulate a delay line. The study measured the linear and nonlinear transmission properties of two-port SAW resonator devices, where SAW resonators served as the physical reservoir medium. The nonlinear process was achieved through nonlinear acoustic wave interactions, enabling complex computational tasks such as radio frequency signal processing.

Electronic Reservoir Computing (ERC) typically employs Field-Programmable Gate Arrays (FPGAs), digital logic gates, flip-flops, and other digital components [98, 104] to implement reservoir computing architectures. This structure offers key advantages such as reconfigurability, parallel processing, and high-speed computation.

Different types of ERC exist depending on the specific devices used, including memristors, spintronic oscillators, ferroelectric devices, and ionic transistors [105, 106]. These devices contribute to memory storage and introduce nonlinearity, enhancing computational efficiency. For instance, in [106], a fully analog reservoir computing (RC) system was demonstrated, utilizing dynamic memristors (DMs) as reservoir nodes and non-volatile memristors (NVMs) as the readout layer. This memristor-based analog RC system achieved real-time signal processing with an efficiency improvement of three orders of magnitude over digital implementations. Performance evaluation through arrhythmia detection and dynamic gesture recognition demonstrated high classification accuracy, reaching 96.6% and 97.9%, respectively.

Optoelectronic & Photonic Reservoir Computing (PRC) encompasses a broad range of hardware implementations rather than a single architectural approach. Early demonstrations relied on delay-based single-node reservoirs using optical fiber loops or optoelectronic feedback systems, while more recent developments include spatially distributed integrated photonic reservoirs based on microring

resonators, semiconductor lasers with delayed feedback, microcomb sources, silicon photonic circuits, and free-space diffractive optical networks [99] [107]. These platforms exploit optical nonlinearity, ultrafast carrier dynamics, and inherent parallelism of light to achieve high-speed and energy-efficient computation.

Among these, Optoelectronic and Photonic Reservoir Computing (PRC) has emerged as a leading approach due to its exceptional speed, energy efficiency, and scalability. Compared to electronic implementations, PRC offers distinct advantages: Ultrafast processing at near-light speed; High bandwidth for handling large-scale data streams; Lower power consumption than traditional electronic reservoirs. This section explores photonic implementations of RC, emphasizing their architectural strengths and real-world applications.

2.3.5 Photonics Reservoir Computing

PRC involves various design paradigms and implementation strategies, particularly in practical applications. These approaches can be classified based on node types, implementation techniques, and emerging methodologies. In this section, I will introduce two types of Photonic Reservoir Computing (PRC), which utilize two primary node types: physical nodes and virtual nodes. Each of these methodologies represents a critical evolution in PRC design, enhancing its versatility and broadening its application potential. Further discussions will explore their advantages, limitations, and practical implementations.

A: Physical Nodes in PRC:

Physical nodes are discrete optical components [31] or optical carries (wavelength) [32] within the reservoir layer, forming an optical node array. These nodes are directly implemented using elements such as semiconductor optical amplifiers (SOAs) or microring resonators, creating a structured and tangible computational network. Beyond traditional optical component arrays, a specialized form of physical nodes, known as Spatial Photonic Reservoir Computing, extends

PRC to spatial information processing in free-space [34]. This approach leverages spatial light modulators (SLMs) or Digital Micromirror Device (DMD) to encode and manipulate spatial data, enabling reservoir computing in spatial domains and expanding PRC applications beyond temporal processing. Additionally, optical carriers, particularly wavelengths, can also serve as nodes [108]. In general, a photonic reservoir utilizing frequency and wavelength multiplexing can further expand the size and complexity of the reservoir nodes.

The following demonstrates photonic reservoir computing using physical nodes, including specific optical components, spatial information processing-based physical nodes, and physical nodes with wavelength nodes.

(i) Photonics Reservoir Computing with Physical node

PRC with a physical array typically utilizes a network of interconnected photonic nodes, where each node is a distinct optical component (e.g., microring resonators, optical waveguides, fiber loops). These nodes act as nonlinear elements, creating a high-dimensional representation of input data. Readout is performed via detectors that capture the final output state [109].

The spatial distribution of optical nodes enables parallel processing of input signals, enhancing computational efficiency. Additionally, the physical separation of nodes reduces interference, minimizes sensitivity to noise, and improves system stability. For more complex tasks, increasing the number of nodes enhances accuracy and efficiency.

Various PRC systems have been designed using physical node arrays with optical components. Fig. 2.13 illustrates a 4×4 swirl-topology photonic reservoir integrated on a silicon chip [110]. This reservoir employs nonlinear microring resonators as nodes, each comprising a single microring resonator interconnected through waveguides with typical propagation losses of 3.0 dB/cm.

The key findings highlight the reservoir's strong performance in executing the delayed XOR task across various operational conditions. It achieves processing

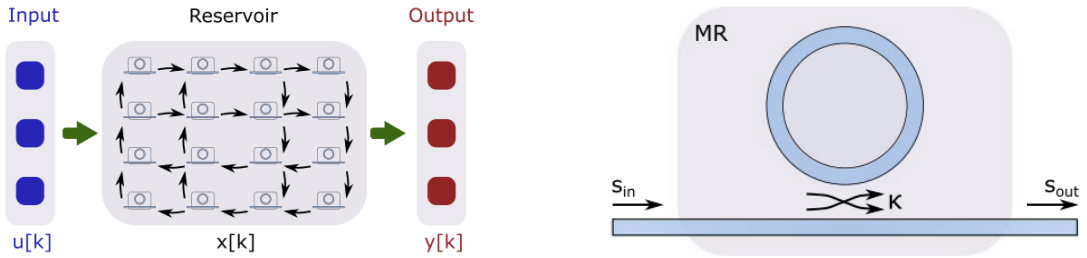

(a) (b)

Fig. 2.13: (a) Schematic of the 4 × 4 swirl-topology photonic reservoir. (b) Diagram of a silicon-on-insulator (SOI) microring resonator serving as a nonlinear node within the reservoir.

speeds of 20 Gb/s with bit error rates (BER) below 10^{-3} while maintaining an average injection power of less than 2.5 mW.

Moreover, the system exhibits high robustness to heterogeneities, including variations in the resonance frequencies of nonlinear nodes, ensuring stable performance even in non-ideal conditions.

These results underscore the effectiveness of the integrated photonic reservoir, which leverages a swirl topology and nonlinear microring resonators for Boolean tasks like the delayed XOR task. Its exceptionally low power consumption further establishes it as a scalable and energy-efficient solution for high-speed photonic computation.

(ii) Spatial reservoir computing

For physical reservoirs implemented with discrete optical components, the number of nodes is typically limited to only a few tens in early demonstrations (e.g., fewer than 23 neurons in some on-chip implementations), while more recent integrated approaches have reached a few hundreds of virtual nodes (e.g., 512 nodes using spatiotemporal encoding) [111]. Such limited node counts constrain the representational capacity and memory depth of the reservoir, thereby restricting overall computational performance.

To address this limitation, researchers have turned to spatial light-based RC.

By leveraging spatial light modulation, this approach overcomes the constraints of RC system based on discrete optical components, enabling higher processing speeds and improved chip-scale integration. A key advantage of spatial photonic reservoir computing (PRC) is its ability to perform true parallel processing, as all nodes process information simultaneously. Additionally, software implementations of spatial PRC have also been explored.

Traditional photonic computing is limited by slow memory operations, restricting dynamic processing capabilities. To overcome this, a spatiotemporal photonic computing (STPC) architecture is proposed, shown as Fig. 2.14 integrating high-speed temporal computing with parallel spatial computing to achieve ultrafast dynamic machine vision [112]. The system eliminates memory read/write bottlenecks by directly processing optical signals, significantly enhancing computational efficiency.

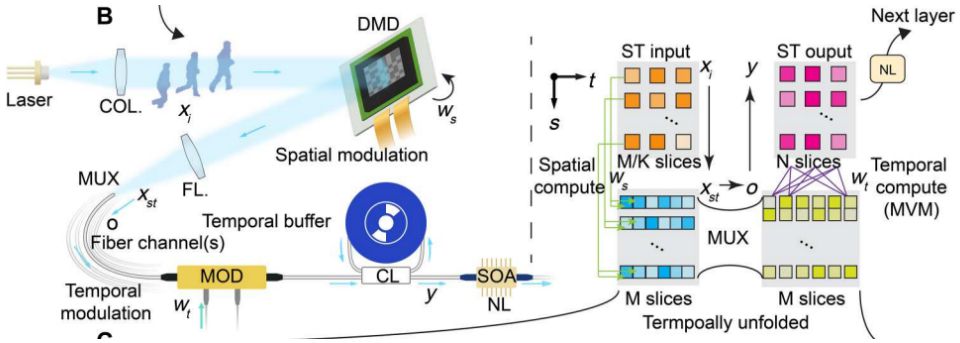

Fig. 2.14: Core architecture of the spatiotemporal photonic computing (STPC) unit. The left panel shows the experimental implementation, including spatial modulation (DMD), spatial-to-temporal multiplexing, temporal weighting and buffering, and nonlinear activation using an SOA. The right panel presents the corresponding network model with temporally unfolded slices and matrix–vector multiplication [112].

Experimental validation shows that STPC improves photonic processing speed 40-fold while reducing parameters 35-fold. A wavelength-multiplexed STPC (WMUX-STPC) system achieves frame times as low as 3.57 nanoseconds, enabling

real-time analysis of nonrepetitive transient visual phenomena. Future advancements in high-speed modulators, multimode fibers, and photonic integration are expected to further scale its capabilities. This architecture revolutionizes ultrafast machine learning and optical computing, with applications in autonomous systems, ultrafast science, and real-time light-field control.

There also has a method to achieve the reservoir nodes using wavelength. A dual time- and wavelength-multiplexed coherent photonic reservoir is capable of supporting hundreds old neurons. And in the method a frequency comb is created and allow for spectral mixing of non-adjacent nodes to enrich the reservoir states, as shown in Fig. 2.15 [108].

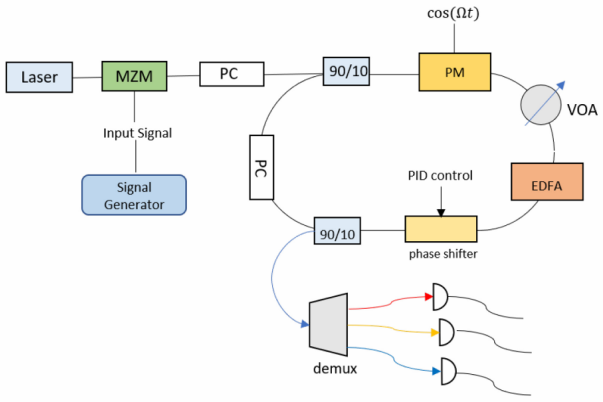

Fig. 2.15: Schematic of the Time- and wavelength-multiplexed reservoir computing.[108]]

This approach significantly increases the reservoir's effective size and complexity, thereby improving its ability to handle complex classification and prediction tasks. Simulation studies have demonstrated the efficacy of this design, showcasing its superior performance in time-series prediction and IP packet filtering tasks. The increased dimensionality and complexity of the reservoir enable enhanced accuracy for sophisticated AI applications, positioning this architecture as a strong candidate for high-efficiency, low-latency photonic AI processors.

B: Virtual Nodes in PRC:

Although PRC with a physical node array offers advantages in processing efficiency and structural simplicity, it also has notable drawbacks. Because of the limitation of physical nodes using discrete optical components, the performance of the RC system is also limited. Since each node consists of separate optical components, fabrication complexity and high costs are major concerns. Additionally, scalability is limited by physical size constraints, and the fixed network structure makes reconfiguration challenging.

Hence, to improve the performance and to reduce the reply on the physical nodes or optical carrier, a method based on a nonlinear node and a delay loop is proposed, call delay-based reservoir computing. The concept of delay line-based RC, first introduced by Appeltant et al. [113] and Pacquot et al. [114], utilizes a single nonlinear node with delayed feedback to reduce hardware complexity in photonic systems. In a delay-based RC system, a single nonlinear optical node (e.g., a semiconductor laser or optical modulator) generates a sequence of virtual nodes over time through delayed feedback. Instead of using multiple physical nodes, time-multiplexing simulates neurons in the reservoir layer. The system relies on a delay loop, typically implemented with an optical fiber or feedback laser cavity, where signals propagate to form a reservoir.

A typically schematic of the delay-based reservoir computer is shown in Fig. 2.16 [109]. This configuration allows the delay line to effectively emulate a high-dimensional reservoir, achieving simplicity and scalability with minimal hardware requirements. A one-dimensional input signal (in red) is first pre-processed using the masking function m(t). The introduction to the input mask will be provided in Chapter 4. Virtual nodes are defined along the delay line and form the reservoir (in green). The output layer (in blue) is unaltered from the standard RC structure.

At each delay interval τ, a new output value $y_{mathrmout}(n)$ is generated. This value is computed as a linear combination of the θ -spaced taps along the delay

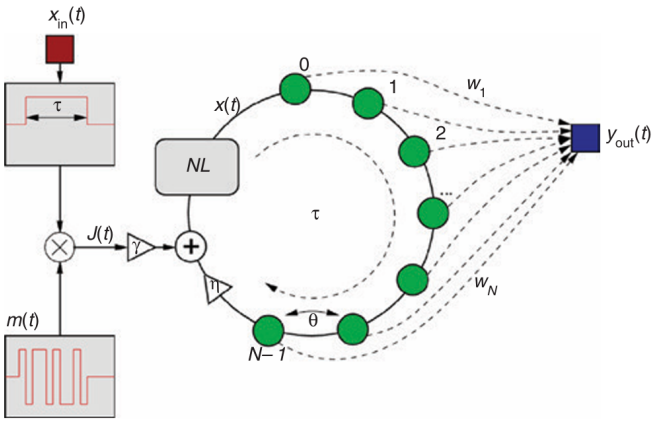

Fig. 2.16: Structure of a delay line-based reservoir computer.[109]

line, which represent the virtual neurons. The output remains constant over the entire delay time τ. While each virtual node corresponds to a measurement point or tap along the delay line, physical realization of these taps is unnecessary. Since the signal $x(t)$ revolves unchanged within the delay line, a single measurement point suffices to gather all necessary data.

For training purposes, the reservoir state $x(t)$ is sampled at each time step θ. These samples are reorganized into a state matrix $\mathbf{S}$, with dimensions determined by the number of virtual nodes N (width) and the number of input samples T (length). The i_{th} column of $\mathbf{S}$ contains the time series of the i_{th} virtual node, influenced by the input signal, masking, and the nonlinear node's dynamical behavior. The state matrix $\mathbf{S}$ is constructed iteratively, one input sample at a time.

Unlike physical nodes, virtual nodes utilize the system's dynamic temporal properties to construct a high-dimensional computational space, enhancing processing efficiency. There are two primary methods for implementing virtual nodes based on different data injection strategies: Opto-Electronic Reservoir Computing (OERC) and All-Optical Reservoir Computing (RC) [115].

OERC integrates analog-to-digital converters (ADCs) between the reservoir and readout layers, bridging optical processing with electronic signal processing. This method is suitable for scenarios where electronic control over the reservoir

system is required. However, Unlike opto-electronic RC, all-optical RC eliminates ADCs, ensuring that both the reservoir and readout layers operate entirely within the optical domain. The absence of optical-electrical conversions significantly enhances processing speed, making it ideal for high-speed applications. I will provide a detailed comparison of the advantages and limitations of these two implementation methods, analyzing their performance, efficiency, and suitability for different applications.

(i): Opto-electronic reservoir computing (OERC)

Optoelectronic systems have been widely utilized in reservoir computing (RC), achieving state-of-the-art performance in classification, prediction, and system modeling tasks. Optoelectronic Reservoir Computing (OERC) is a hybrid system that combines both optical and electronic components for computation, which can be implemented in the input layer, reservoir layer, or readout layer [116].

In general, OERC utilizes optical components for nonlinear processing, while electronic devices or circuits handle feedback processes or are used in the readout layer. Compared to purely electronic systems, OERC offers higher processing speeds, improved energy efficiency, and seamless integration with existing electronic hardware (for example, FPGA). Additionally, it leverages electronic techniques for enhanced compatibility and scalability in practical applications.

OERC has been enhanced through FPGA-based architectures, leveraging their high-speed, reconfigurable nature to improve processing efficiency and adaptability across various tasks. The integration of field-programmable gate arrays (FPGAs) with electro-optic modulators (EOMs) enables real-time signal processing with flexible dynamics, high connectivity, and scalable reservoir nodes.

An experimentally validated optoelectronic reservoir computing (RC) system utilizing an electro-optic modulator (EOM) and a field-programmable gate array (FPGA) demonstrates the feasibility of digital implementation of delay lines and filters, ensuring stable delay logic and controllable timing [117]. The system was

tested on three benchmark tasks: NARMA-10 (NRMSE: 0.142), Santa Fe laser data prediction (NMSE: 6.73×10^{-3}), and isolated spoken digit recognition (WER: 0.34%), achieving competitive performance in nonlinear sequence prediction and pattern recognition.

However, current speed limitations arise from analog-to-digital (ADC) and digital-to-analog (DAC) conversion rates, suggesting that future improvements in hardware integration—such as faster ADCs and DACs—could significantly enhance real-time processing capabilities. This FPGA-based optoelectronic approach presents a promising avenue for advancing high-speed reservoir computing applications.

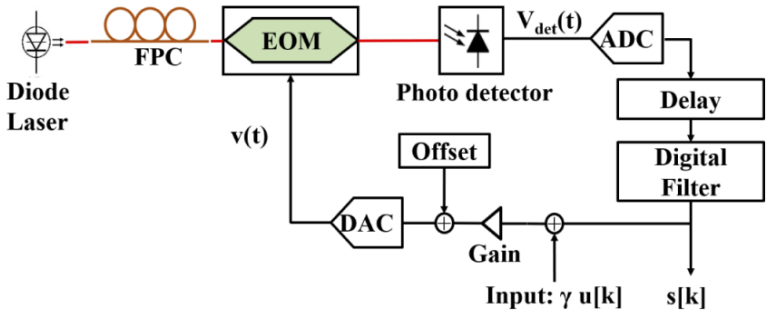

Fig. 2.17: Schematic diagram of a digital opto-electronic reservoir computing (RC) system. The setup consists of a diode laser, fiber polarization controller (FPC), electro-optic modulator (EOM), photodetector, analog-to-digital converter (ADC), digital delay and filter, and digital-to-analog converter (DAC) forming a feedback loop with adjustable gain and offset. reference [117].

(ii): All-optical reservoir computing

In optoelectronic reservoir computing, signal conversion between optical and electrical domains is required, which introduces delays and reduces processing speed. To overcome this limitation, all-optical reservoir computing has been proposed. This approach eliminates optical-to-electrical conversion, ensuring that all operations, including feedback, occur entirely within the optical domain.

By maintaining signals within the optical domain throughout computation, all-optical reservoir computing enables ultra-fast processing, high energy efficiency,

and the potential for massive parallelism. These advantages make it particularly well-suited for neuromorphic computing applications.

A bidynamical all-optical RC system—meaning a system that simultaneously exploits two independent dynamical mechanisms, namely intensity dynamics and polarization dynamics—is proposed, as shown in Fig. 2.18, utilizing a semiconductor optical amplifier (SOA) fiber loop to enable parallel task processing [118]. The system exploits two independent dynamical responses—intensity dynamics (via intensity modulation) and polarization dynamics (via phase modulation)—to process multiple tasks simultaneously. This is the first implementation of using both dynamical responses in an all-optical RC system as independent computational channels for parallel processing, offering improved efficiency with lower system cost.

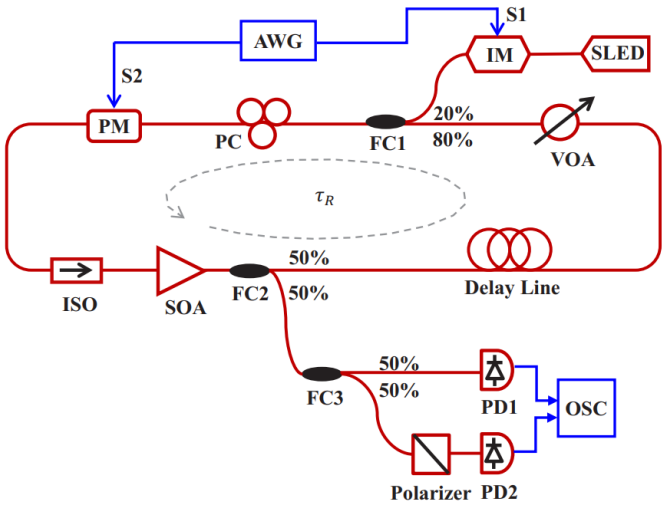

Fig. 2.18: Experimental setup of a bidynamical all-optical reservoir computing (RC) system based on a semiconductor optical amplifier (SOA) fiber loop. AWG: arbitrary waveform generator; IM: intensity modulator; SLED: superluminescent diode; PM: phase modulator; PC: polarization controller; FC: fiber coupler; VOA: variable optical attenuator; ISO: optical isolator; PD: photodetector; OSC: oscilloscope [118].

To evaluate performance, the system was tested on two benchmark tasks:

Santa Fe time-series prediction in the intensity dynamic channel; Signal classification in the polarization dynamic channel. Experimental results confirm that the system effectively processes two independent tasks in parallel, with optimal performance achieved when the scaling factor for the polarization channel is at least 1. Additionally, the intensity channel is better suited for time-series prediction, while the polarization channel performs better for classification tasks.

This approach simplifies multi-task processing architectures, reduces hardware complexity, and enhances the practical applicability of all-optical reservoir computing. By fully utilizing polarization dynamics in SOA fiber loops, this work introduces a novel direction for advancing high-speed, low-cost optical computing systems.

C: Quantum Photonic Reservoir Computing (QPRC):

In recent years, beyond traditional hardware implementations, new advancements, such as quantum field techniques, have emerged as a cutting-edge advancement driven by quantum technologies, introducing novel applications for reservoir computing, particularly in the domains of quantum and photonic systems [119] Researchers have begun exploring these approaches due to their promising advantages.

PQRC leverages quantum superposition and entanglement, introducing a novel computational paradigm that vastly expands the capabilities of classical PRC. By harnessing quantum parallelism, PQRC enables a single computation to explore multiple solutions simultaneously, improving efficiency in solving complex problems [120]. Unlike classical PRC, which relies on nonlinear optical transformations, PQRC benefits from an exponentially expanding state space as the number of quantum modes (qubits) increases, enabling advanced high-dimensional feature mapping [119]. As shown in Fig. 2.19, a QPRC based on identical optical pulses as reservoirs, recirculating through a closed-loop architecture.

In the reservoir layer, optical pulses interact with nonlinear ($\chi^{(2)}$) crystals to

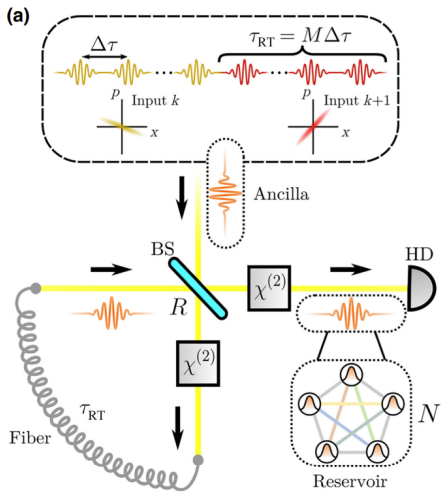

Fig. 2.19: schematic diagram of the whole platform based on QPRC.[119]

generate entanglement and nonlinear transformations. In the readout layer, beam splitters (BS) and homodyne detection are employed to extract reservoir states without the need for external memory storage.

Compared with traditional reservoir computing (RC), this structure uses an optical pulse-based reservoir, where each pulse contains N quantum modes, effectively increasing computational dimensionality without additional hardware complexity. This higher-dimensional computation improves the reservoir's capacity to process complex tasks, such as chaotic time-series prediction.

In additional, this research is the simulation about the feasibility of the proposed QPRC scheme. The feasibility of photonic QRC has been supported by advancements in state-of-the-art photonic technologies, external memory storage and repetitive measurements, photonic QRC real-time processing capabilities by non-temporal classification problems, as demonstrated.

These findings contribute to the broader discourse on scalable quantum computing architectures, providing a pathway toward efficient real-time quantum machine learning applications. The large-scale signal processing and AI-driven decision-making.

2.3.6 Summary

As mentioned earlier, various types of Photonic Reservoir Computing (PRC) exist; however, existing PRC models are not well-suited for integration with PTS, as many rely on delay-based or feedback architectures that are difficult to synchronize with the ultrafast, single-pass signal processing scheme of PTS. In this thesis, we present an example of integrating Reservoir Computing (RC) with PTS, leveraging their unique characteristics to achieve high-throughput detection and classification. The proposed structure is designed to be simpler, more efficient, and easier to implement in real-world applications, making it a practical solution for high-speed optical data processing.

2.4 Summary

This chapter has reviewed the theoretical foundations relevant to this thesis, including photonic time-stretch systems, machine learning paradigms, artificial neural networks, and recurrent architectures for temporal processing.

Among various learning frameworks, supervised learning provides the methodological basis for reservoir computing. While conventional recurrent neural networks offer strong capabilities for modeling time-dependent signals, their training complexity and gradient instability limit practical implementation in high-speed and hardware-oriented systems.

Reservoir computing emerges as a simplified recurrent framework that preserves temporal processing capability while significantly reducing training requirements. By decoupling dynamic state generation from output optimization, it enables efficient and scalable implementations, particularly in physical and photonic systems.

These theoretical insights establish the foundation for the optical reservoir computing architectures developed in the subsequent chapters.

Chapter 3

Reservoir Computing for High-throughput Signal Analysis

3.1 Introduction

As discussed in Chapter 2, reservoir computing can be implemented in various forms and has been widely applied due to its simple architecture and high efficiency in processing temporal and high-dimensional data. Its capability to process large volumes of time-gated data in real time without extensive preprocessing makes reservoir computing particularly suitable for high-throughput detection tasks. Such tasks are critical in fields such as genomics, proteomics, image analysis, and chemical sensing, where rapid data processing and decision-making are essential.

In this chapter, we present our research on the application of reservoir computing in wireless communication. Leveraging its capability for processing temporal data, reservoir computing is employed for indoor user localization. Specifically, it is used to process signals reflected by users in conjunction with a 45° tilted fiber Bragg grating (TFBG). In addition, reservoir computing is applied to frequency-hopping detection, which is a critical task in wireless communication systems.

Simulation results demonstrate that reservoir computing can effectively detect frequency changes while achieving faster processing speeds compared to conventional methods. These results highlight the potential of reservoir computing for improving both the efficiency and accuracy of wireless communication systems.

3.2 Reservoir Computing Assisted Ultrafast User Localization in Beam Steering Optical Wireless System

3.2.1 Introduction

With the rapid development of wireless communication, the available radio-frequency spectrum has become increasingly limited. The increasing demand for high-speed wireless and on-demand applications has pushed the available radio-frequency (RF) bandwidth to its limits. Therefore, alternative solutions are required to meet the increasing demand for wireless bandwidth. Optical wireless communication (OWC) has emerged as a promising alternative due to its large modulation bandwidth and license-free spectrum [121]. Two major OWC strategies have been investigated widely: visible light communication (VLC), and OWC using steered narrow infrared beams [122]. Beam steering enables energy-efficient transmission of information to individual users [123]. This approach enables the establishment of high-speed links directed specifically to individual devices, ensuring that the optical beam is delivered only where it is required. It can even have a seamless integration into the future FTTH (fiber to the home) and FITH (fiber in the home) infrastructure [124]. Hence, the beam steering approach has attracted great attention due to its advantages such as direct user-specific links with high privacy, and seamless integration into the existing home infrastructure.

Beam steering provides an effective solution for serving multiple users in the

"last meters" of the network, bridging the gap between end-users and fiber infrastructure. Therefore, beam steering has attracted increasing research interest for various wireless communication applications. Multi-beam steering is an important technique for covering large areas and serving multiple users, as well as tracking mobile users and routing signals to different receiving devices simultaneously [125]. An all-optically controlled, non-mechanical multi-beam steering method based on wavelength sweeping and optical diffraction devices has recently been reported for wide-area coverage and multi-user communication. This concept was later implemented using an all-fibre diffraction grating, which provides high diffraction efficiency, compactness, fibre compatibility, and bias-free polarization modulation [126].

Beam-steered OWC has achieved high-capacity wireless links, with a data rate of up to tens of Gb/s per user [127]. Accurate user localization is also a highly demanded function in indoor OWC systems. Existing localization methods for OWC such as those based on cameras [128], reflections [129], LED beacons [130], and LED-tag system [131] cannot be easily applied to wavelength-controlled beam steering OWC systems [123, 124, 125]. A promising solution using retro-reflecting optical corner cubes to identify the angle of reflected signals has been recently demonstrated for beam steering OWC [132]. However, the system is complex and suffers from high coupling loss between free space and fibre links. An ultrafast user localization approach using in-fibre diffraction grating with passive wavelength sweeping based on photonic time stretch has been reported for beam steering OWC [133]. Challenging real-time identification of instantaneous optical wavelength in nanosecond scale has been addressed via chirped microwave frequency encoding and detection. However, a computationally intensive short-time Fourier transform (STFT) is typically required to identify the instantaneous microwave frequency.

In this section, we investigate the use of reservoir computing (RC) for ultrafast wavelength-encoded user localization. Our results have shown that the RC

approach is more efficient compared to STFT to detect instantaneous microwave frequency in real-time user localization. In previous studies, only the angular separation between users could be characterized. Here we show that our approach can simultaneously extract angle and linear distance information for each user from the same scanning measurement. A proof-of-concept experiment was conducted to validate the proposed approach. The results demonstrate that accurate user localization can be achieved.

3.2.2 Principle

The schematic diagram of the proposed ultrafast user localization system is shown in Fig. 3.1a. The system consists of four subsystems: time stretching, optical spectrum chirp encoding, in-fibre diffraction beam steering, and localization processing. Firstly, ultrashort optical pulses from a mode-locked laser (MLL) are time-stretched by a dispersion compensating fibre (DCF). After being amplified by an erbium-doped fibre amplifier (EDFA), the time-stretched pulses are spectrally shaped by a dispersion unbalanced Mach-Zehnder interferometer (MZI), which has a chirped optical spectral response [64]. The stretched and spectrally shaped optical pulse acts as a passive wavelength-sweeping source with a wavelength-dependent free spectral range (FSR). A 45° TFG functions as a highly efficient in-fibre diffraction grating [42] to emit the spectral rainbow into different locations in free space to achieve ultrafast beam steering. The speed of steering is determined by the repetition rate of the MLL, which is 50 MHz in this work. The reflected optical signal from a remote user is only a fraction of the stretched optical pulse. After photodetection at the localization processor, a time-gated signal with its unique microwave carrier frequency is obtained. The optical wavelength of the reflected pulse that tells user location can be determined from its instantaneous microwave frequency according to the relation between time stretch and spectral shaping.

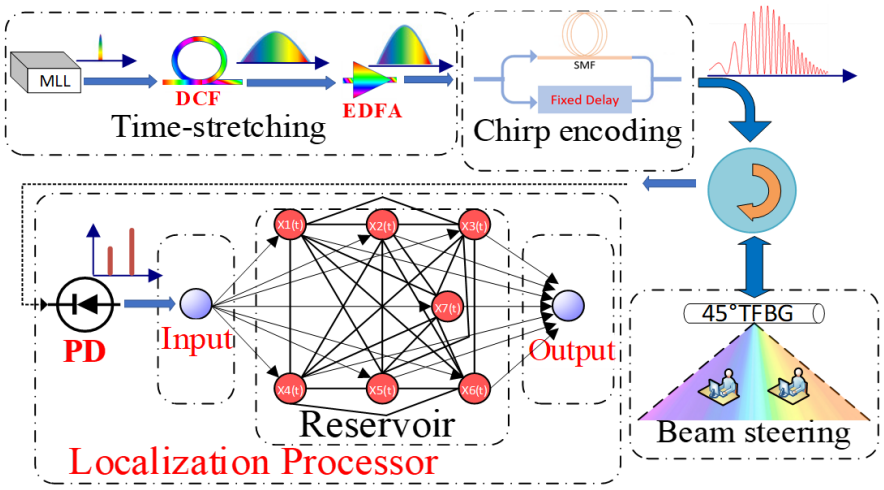

(a)

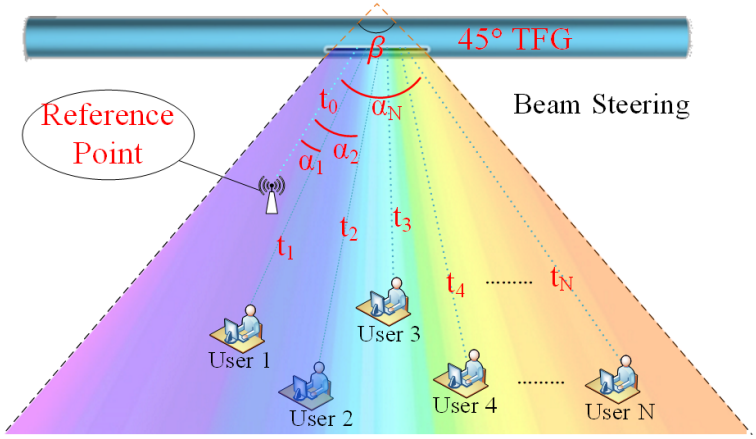

(b)

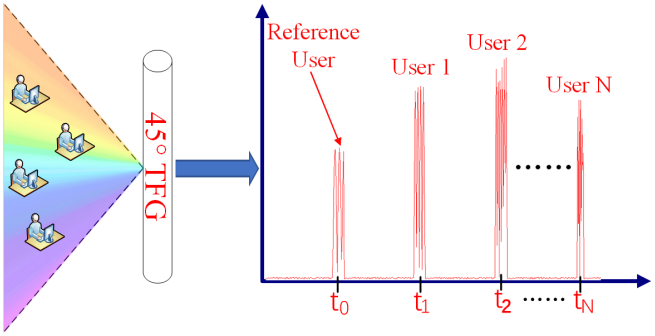

(c)

Fig. 3.1: Schematic diagram of the proposed approach. (a) Setup for ultrafast user localization system. MLL: Mode Locked laser, DCF: Dispersion compensation fibre, SMF: Single-mode fibre; (b) Beam scanning using a 45° TFG; (c) Received optical pulses corresponding to different uses [134].

In this work, we aim to achieve indoor user localization with the assistance of reservoir computing. The key challenge in this approach is capturing the reflected signal from indoor users, as indoor reflections are typically weak, multipath-distorted, and easily masked by environmental interference, making reliable extraction of frequency and positional information difficult. After photonic time stretching and chirp coding, a mapping between wavelengths is established. A 45 TFBG is used to distribute frequencies across different spatial positions, with the dispatch principle detailed later. As a result, the reflected pulses contain both frequency and position information, requiring rapid frequency identification. To address this, reservoir computing is employed to encode different frequencies into distinct labels and identify the central frequency, ultimately determining the user's position in free space.

To determine users' localization in free space, the absolute distance and relative angle need to be measured. The absolute distance between a remote user and the access point is determined by the time-of-flight in free space (t_F). The total delay time of a time-gated signal includes both t_F and the wavelength-dependent time delay within the original chirped optical pulse (t_W), as shown in Fig. 3.1c.

$$t_N = t_F + t_W \tag{3-1}$$

where t_N is the time delay of user N ($N = 1, 2, 3, \dots$) as shown in Fig. 3.1b, and t_W can be determined once the central frequency of the time-gated signal is identified. t_W and t_F can be obtained by Eq.(3-2) and Eq.(3-3):

$$t_F = \frac{2 \cdot D_L}{c} \tag{3-2}$$

$$t_W = D\lambda_L \cdot \frac{F_{CN}}{F} \tag{3-3}$$

where c is the speed of light in vacuum, D_L is the absolute distance between

the users and the access point. D is the total dispersion in the system, λ_L is the overall optical bandwidth of the laser pulse. $D\lambda_L$ denotes the duration time of the whole stretched optical pulse, F is the total microwave chirp bandwidth carried by the stretched optical pulse, and F_{CN} denotes the central frequency of the reflected pulse.

The 45° tilted fiber Bragg grating (TFBG) functions as the beam-steering component in the proposed system. Owing to its tilted refractive index modulation, part of the guided optical power is coupled from the core mode to radiation modes, resulting in wavelength-dependent diffraction in free space.

Unlike a conventional FBG, where the refractive index fringes are perpendicular to the fiber axis and primarily produce wavelength-selective reflection, the tilted structure enables directional radiation. As illustrated in Fig. 3.2a and Fig. 3.2b, the grating tilt introduces angular dispersion, allowing different wavelengths to propagate at distinct angles. This wavelength-to-angle mapping forms the basis for spatial beam scanning and multi-user localization in the proposed system.

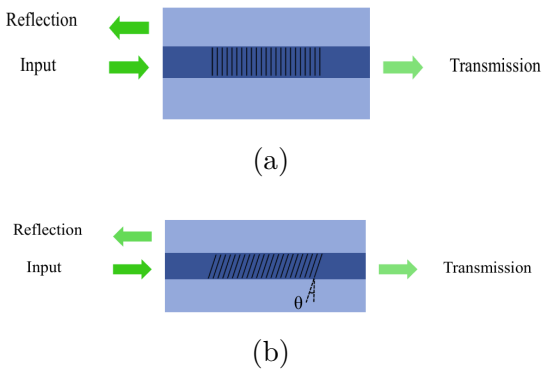

Fig. 3.2: (a) Structure of a typical uniform Fiber Bragg Grating (FBG). (b) Structure of a Tilted Fiber Bragg Grating (TFBG).

As illustrated in Fig. 3.2a, a typical uniform Fiber Bragg Grating (FBG) consists of periodic refractive fringes perpendicular to the fibre axis. This configuration allows only a specific wavelength to be reflected when a broadband optical

spectrum propagates through it, while the remaining wavelengths pass through the grating.

Different from the normal FBG, as shown in Fig. 3.2b, the grating fringes in a Tilted Fiber Bragg Grating (TFBG) are tilted at an angle relative to the fibre axis. This configuration allows specific wavelengths in the broadband light to couple into backward core and cladding modes from the forward core mode. Additionally, TFBGs exhibit high sensitivity to the surrounding refractive index (SRI) due to the interaction of light with the cladding region.

The mode coupling mechanism in TFBGs is governed by the phase matching condition, which determines the strongest wavelength coupling between core and cladding modes. Similar to FBGs, the transmitted resonance wavelengths that satisfy the Bragg condition in the core mode are also determined by the phase matching condition, expressed as [135]:

$$\lambda_B = 2n_{e,\text{core}}\Lambda_g \tag{3-4}$$

where Λ_g represents the grating period of the TFBG. In this case, Λ_g is defined as:

$$\Lambda_g = \Lambda \cdot \cos\theta \tag{3-5}$$

where θ denotes the tilted angle of the TFBG.

Due to light reflection in the cladding mode of the TFBG, the cladding mode resonance wavelength ($\lambda_{\text{clad},i}$) must also satisfy the phase matching condition. It can be expressed as:

$$\lambda_{\text{clad},i} = (n_{e,\text{core}} + n_{e,\text{clad},i}) \cdot \Lambda_g \tag{3-6}$$

where $n_{e,\text{clad},i}$ represents the effective refractive index of the fiber cladding mode in the TFBG, and i denotes the order of the cladding mode. However, the bandwidth of the cladding mode resonance wavelength ($\Delta\lambda_{\text{clad},i}$) in the TFBG is

given by:

$$\Delta\lambda_{\text{clad},i} = \frac{(\Delta n_0 \eta_{\text{core}} + \Delta n_{e,\text{clad},i}\eta_{\text{clad}})}{\pi} \cdot \lambda_{\text{clad},i} \tag{3-7}$$

where η_{clad} represents the fraction of power in the cladding mode.

The angular emission of the beamed light has a mapping relationship with the sequence of beam wavelengths and frequencies. Fig. 3.3 illustrates the structure of a 45° TFBG, where the grating structure is tilted at an angle θ. This configuration enables different wavelengths of light to radiate out of the fiber at distinct angles [136].

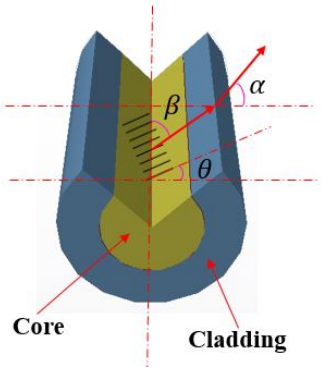

Fig. 3.3: The structure of 45° TFBGs. [136]

According to the vector algorithm, the scattering angle of the radiation mode inside the fiber can be determined using [137]:

$$\cot\beta = \cot\theta - \frac{n\Lambda}{\lambda \sin\theta} \tag{3-8}$$

where β represents the scattering angle with respect to the fibre axis, θ is the tilt angle of the fibre grating, and λ denotes the wavelength of the light.

When light exits into the air, refraction occurs at the interface between the fibre cladding and air. The scattering angle of the radiation mode outside the fibre is described by:

$$\sin\alpha = \frac{n \cdot \left(\cot\theta - \frac{n\Lambda}{\lambda \sin\theta}\right)}{\sqrt{1 + \left(\cot\theta - \frac{n\Lambda}{\lambda \sin\theta}\right)^2}} \tag{3-9}$$

In [126, 138], the diffractive characteristics of 45° TFBGs have been theoretically analyzed using the vector algorithm and phase matching condition. These studies established the relationship between the scattering angle of the radiation mode and the parameters of the grating and incident light. For a wavelength range between 1530 nm and 1570 nm, the theoretical angular dispersion of a 45° TFBG in free space is calculated to be 0.054°/nm [139]. In practical operation, the effective bandwidth is typically limited by the source spectrum and the grating's coupling efficiency, and spans several tens of nanometers (approximately 30–40 nm), within which different wavelengths can be spatially separated with distinguishable diffraction angles. This characteristic is pivotal for enabling indoor user localization in our research.

In this work, the relative angle of emitted beams for remote users has a mapping relationship with the sequence of beam wavelength and frequency, as shown in Fig. 3.1b. A fixed reference point is set in this localization system. The relative angle of other users with respect to the reference can be confirmed easily. The relative angle difference between user N and the reference point can be obtained from:

$$\Delta\alpha_N = \frac{c}{(F_{CN} - F_{C0})} \cdot \beta_{\text{TFBG}} \tag{3-10}$$

where F_{CN} is the central microwave frequency carried by the optical pulse reflected from user N, F_{C0} is the central frequency for the reference point, and β_{TFBG} is the angular dispersion of the 45° TFBG.

It can be seen from the above analysis that identification of the central microwave frequency carried by the reflected optical pulse is the key to identify both the angle and distance information of a certain user. In this work, a new

frequency identification method based on reservoir computing (RC) is proposed. RC is a recurrent machine learning framework based on several recurrent neural network (RNN) models [82]. It has been successfully applied in high-throughput cell screening and classification of instantaneous microwave frequency.

Here, RC is used to recognize the instantaneous frequency of the captured time-gated signals as it can transform the input data into spatiotemporal patterns in the reservoir. In this work, ridge regression, also called regression with Tikhonov regularization, was used to train the readout weights. The RC is implemented in software as an ESN with fixed, randomly generated sparse recurrent connections, while only the linear readout layer is trained. The reservoir states are updated using a nonlinear activation function with fading memory dynamics. The reservoir dimension is set to 100 as a trade-off between computational complexity and classification accuracy, since larger reservoirs provided only marginal performance improvement in our preliminary tests. The whole chirped waveform at the output of the MZI is used as the training dataset, as it contains all the possible reflected signals from remote users. For each training waveform, the reservoir state vectors are recorded over time and arranged into a state matrix. The corresponding frequency labels are assigned to each sample, and the readout weights are obtained in a single step by solving a ridge-regularized least-squares problem. During inference, the trained readout weights are applied to the reservoir states to predict the carrier frequency. When the reflected light beam from a remote user position is injected into the reservoir, the readouts (carrier frequency) can be computed by employing the trained output weights. Ridge regularization reduces overfitting and improves robustness, particularly given the high dimensionality of the reservoir state matrix. Note that the training is only a one-off process for a given optical setup, as the wavelength-time-space mapping is fixed.

3.2.3 Results and Discussion

A: Simulation setup and discussion

Utilizing beam steering with a 45° TFG and reservoir computing to verify the proposed ultrafast user localization was carried out. A numerical simulation is first conducted to verify the feasibility of real-time microwave frequency classification using RC. Optical pulses from the 50 MHz MLL are time-stretched to a pulse width of 12 ns. After chirped spectral shaping, the stretched pulse carries chirped microwave frequency with a total bandwidth of 40 GHz. In the 45° TFG based beam steering system, as shown in Fig. 3.2a, each user only receives and reflects a fraction of the stretched optical pulse based on the location. The spectral window of each user is set as 0.8 nm. The duration of each optical pulse reflected from users is 0.3 ns. This value is selected to ensure temporal separation between adjacent user reflections within the 40 GHz system bandwidth, while remaining compatible with the time-stretch resolution of the system. The simulation considers one reference point and three remote users. The reference point has a fixed distance of 1 m and a fixed diffraction angle corresponding to a microwave carrier frequency of 12 GHz. The three users have different distances from the fibre access point: 1.3 m, 1.5 m, and 1.7 m for User 1, User 2 and User 3, respectively. These distances are chosen as representative indoor user positions with sufficient spatial separation to generate distinguishable time-of-flight delays within the simulated scenario. The following angle differences with respect to the reference point have been set for the three users: 0.2°, 0.32°, and 0.45°. These angular differences are selected to ensure resolvable wavelength-dependent diffraction shifts according to the angular dispersion of the 45° TFBG.

In the simulation, the reflected pulses are generated according to the time-of-flight corresponding to each user distance and the wavelength–angle mapping of the 45° TFBG. The stretched waveforms are then injected into the software-implemented ESN reservoir, and the resulting reservoir states are processed by

the trained readout layer to identify the carrier frequency associated with each user.

Fig. 3.4a shows the reflected optical pulses from three users (red). The following time delays can be observed: 9 ns for the reference point, 14.12 ns, 17.4 ns, and 22.81 ns for User 1, User 2 and User 3, respectively. When the reflected pulses are injected as an input, the reservoir can identify the individual waveforms by matching the frequency with the previously trained waveforms. The blue line in Fig. 3.4b presents the instantaneous microwave frequency identified by RC. The central frequencies for the reflected optical carrier pulses are identified from the trained RC readout layer and correspond to the wavelength-dependent diffraction mapping of the 45° TFBG combined with the time-of-flight delay. Specifically, the angular dispersion of the TFBG determines the wavelength shift associated with each user position, which is then converted into a microwave carrier frequency through the time-stretch mapping. As a result, the extracted central frequencies are 12.02 GHz, 15.36 GHz, 17.78 GHz, and 20.08 GHz for the reference, User 1, User 2, and User 3, respectively. The slight deviation from nominal integer values arises from the finite spectral resolution and dispersion characteristics of the simulated system. The angle separation for each user from the reference point can be calculated instantaneously as 0.186° (User 1), 0.347° (User 2), and 0.541° (User 3).

Additionally, to compare and validate the classification results from reservoir computing (RC), Short-Time Fourier Transform (STFT) is performed as a benchmark standard [140]. In the context of instantaneous microwave frequency measurement, STFT can provide valuable insights into the time-frequency characteristics of the signal.

In practice, the STFT is computed by dividing a longer time-domain signal into shorter segments of equal length. The Fourier transform is then applied to each segment individually, revealing the frequency spectrum for each section

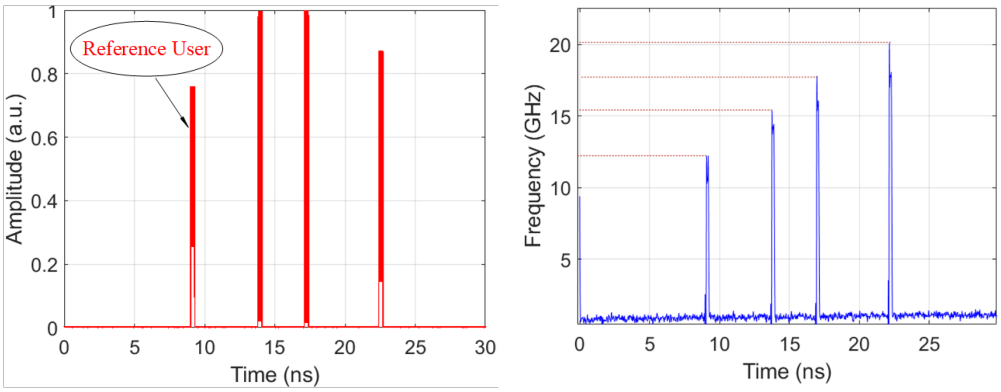

(a) (b)

Fig. 3.4: (a) Simulated reflected optical pulses from the reference and three users (red), showing different time-of-flight delays. (b) Instantaneous microwave frequencies identified by the trained RC (blue), obtained by mapping the RC output to the carrier frequencies defined by the 45° TFBG wavelength–angle model.

of the signal. This segmented approach enables the analysis of how frequency components vary over time.

In the discrete-time case, the data to be transformed is divided into chunks or frames, which typically overlap to minimize boundary artifacts. Each frame undergoes a Fourier transform, and the resulting complex values are stored in a matrix. This matrix captures the magnitude and phase of the signal for each point in time and frequency. Mathematically, this can be expressed as:

$$\mathrm{STFT}\{x[n]\}(m,\omega) \equiv X(m,\omega) = \sum_{n=-\infty}^{\infty} x[n]w[n-m]e^{-i\omega n} \tag{3-11}$$

Similarly, in the discrete-time case, the signal $x[n]$ is multiplied by a window $w[n]$. Here, m represents the discrete time index, and ω denotes the continuous frequency. However, in most practical applications, the Short-Time Fourier Transform (STFT) is computed digitally using the Fast Fourier Transform (FFT), meaning both m and ω become discrete and quantized.

The magnitude squared of the STFT produces the spectrogram, which represents the power spectral density of the function:

$$\text{spectrogram}\{x(t)\}(\tau,\omega) \equiv |X(\tau,\omega)|^2 \tag{3-12}$$

In this work, a conventional STFT approach has been applied to calculate the carrier microwave frequencies as a golden standard, with results shown in Fig. 3.5. The recognized central frequencies are 12 GHz, 15 GHz, 16.8 GHz, and 19.7 GHz for the reference point, User 1, User 2 and User 3, respectively. Removing the initial wavelength-dependent time delay due to time stretch from the overall time delay, the actual time-of-flight values for the reference and three users are estimated as 7.26 ns, 8.92 ns, 9.6 ns, and 11.86 ns, respectively.

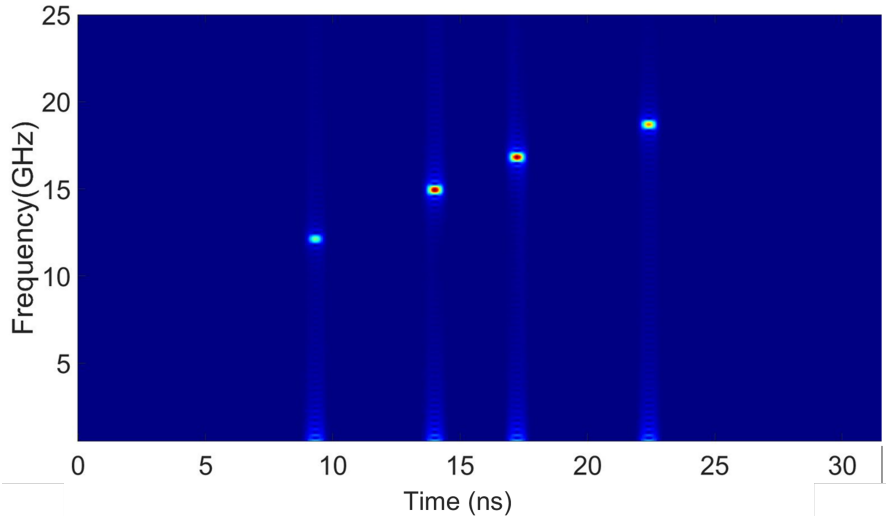

Fig. 3.5: Instantaneous microwave frequency measurement using STFT.

B: Experiment setup and discussion

A proof-of-the-concept experiment was also carried out. A passive mode-locked laser (MLL, Calmar Mendocino FP laser) produces a 50 MHz optical pulse train with 800 fs pulse width and a 12 nm optical bandwidth. A dispersion compensating fibre (DCF) with a total dispersion value of -1.04 ns/nm stretches optical

pulses to 12 ns. The stretched optical pulses are spectrally encoded with the Mach-Zehnder interferometric (MZI) setup with an optical delay line and 500 m SMF to get a high chirp rate. The 500 m SMF introduces significant chromatic dispersion, which converts wavelength variations into time delays. This dispersion-induced time stretching determines the effective chirp rate of the stretched optical pulse. The mapping is established between optical wavelength and instantaneous microwave frequency, as shown in Fig. 3.6. Therefore, challenging real-time optical wavelength identification within the reflected optical pulses (sub-ns range) can be achieved via instantaneous microwave frequency measurement.

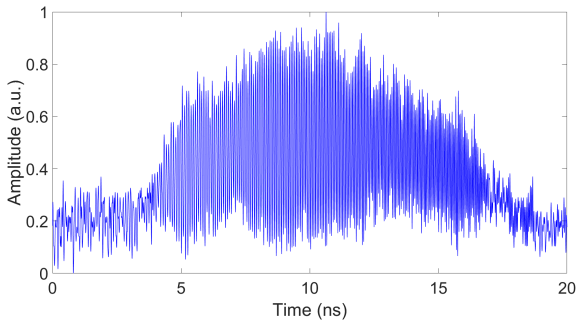

(a)

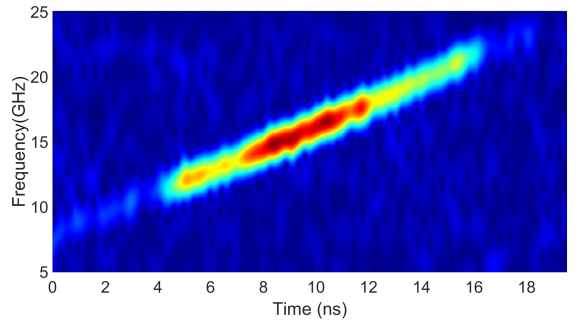

(b)

Fig. 3.6: (a) The measured time stretched optical pulse after spectral chirp encoding. (b) Corresponding spectrogram showing mapping relation between optical wavelength and instantaneous microwave frequency.

In the experiment, three reflective targets were used to emulate users: one served as the reference position, while the other two acted as remote targets placed

at different distances. In Fig. 3.7, the red curve shows the measured optical pulses reflected by all the users using a real-time oscilloscope (Tektronix DPO72304DX, , 23 GHz bandwidth). The blue line in Fig. 3.7 presents the identified carrier frequency of the detected pulses using the trained RC model. It estimates 12.58 GHz for User 1 and 16.95GHz for User 2, which matches well with the STFT results of 12.04 GHz and 17.16 GHz. The waveform with higher microwave frequency shows poor visibility due to bandwidth limitation of the photodetector and oscilloscope. RC works well even with poor visibility.

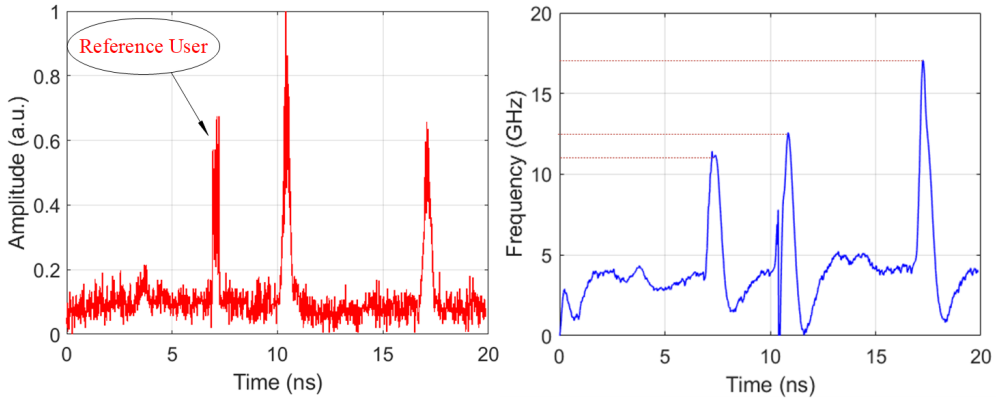

Fig. 3.7: Reflected pulses from two users with each carrying different chirp frequencies (red line) and classified using RC (blue line).

The localization accuracy of the approach depends on the accuracy of microwave frequency measurement. STFT is a very precise frequency analysis approach. RC-based frequency estimates are compared against the reference frequencies obtained from STFT analysis, which is treated as the ground truth due to its high spectral resolution. The frequency accuracy is calculated as the relative error between the RC-predicted carrier frequency and the STFT-derived frequency, averaged over all detected pulses. Using this metric, the average relative error is 3.37% for simulation data and 4.94% for experimental data.

Compared with STFT, the RC approach has much lower computational complexity because it only requires linear multiplications, making it a more efficient

method. For example, to process the same input optical pulses with 200,000 sampled data points, RC costs only 2.51 s (including training and classification), while it takes STFT an average time of 23.9 s. Both RC and STFT processing times were measured in software on the same desktop computer (Intel Core i5 CPU, 16 GB RAM) using MATLAB implementation, without hardware acceleration. Moreover, STFT needs to collect all the data within the short-time window before FT calculation starts, and the short-time window cannot be too short to maintain a good frequency resolution. The trained RC creates a sliding window and calculation starts right away when the temporal data arrives, as shown in Fig. 3.4 and Fig. 3.7. Therefore, RC holds high potential in real-time user localization with a fast response time.

RC is a special variant of RNN. As only the readout weights need to be trained with linear regression, RC is more efficient and computationally faster in both training and calculation processes compared to general RNN models, while maintaining similar identification performance.

3.2.4 Conclusion

In this work, an ultrafast multi-user free-space localization technique was proposed based on beam scanning and reservoir computing. This offers a promising solution for real-time user localization in OWC. We proposed and demonstrated that the users' localization can be calculated by the beam angular and the absolute distance. The beam scanning can up to 50 million per second, which can realize the real-time user localization. RC was used to processing and classifying the reflected signal from users. Optical wavelength detection was achieved by RC by calculating instantaneous microwave modulation frequency. Compared with the short-time Fourier transform (t = 23.9s), the RC have a faster calculation speed (t = 2.51s). The proposed real-time localization approach provides great promise in OWC with unique features of high speed, inherent compatibility with

the existing beam steering system, and complete free-space positioning.

3.3 Real-time identification of frequency-hopping millimeter-wave signals using photonic time stretch and reservoir computing

3.3.1 introduction

Frequency-hopping spread spectrum (FHSS) is a method of transmitting signals on multiple carriers [141]. Due to its advantages, such as its strong anti-interference ability, good security, resistance to a multipath propagation environment, and convenience for networking [142], the frequency hopping (FH) system has been applied in military communication and civilian mobile communication [143]. The classification of FHSS signals is a challenging and important task in communication systems. However, detecting and tracking FHSS signals remains challenging due to their wide bandwidth and hardware limitations. [144].

Nowadays, Frequency Hopping Recognition has become a promising technology, and great attention is put on the detection and parameter estimation of FHSS signals. The estimation method leads to the successful estimation of the FHSS carrier frequency. Hence, numerous methods have been used for FHSS recognition [145], such as the short-time Fourier transform (STFT), compressive sampling (CS), and other algorithms. FHSS recognition based on discrete Fourier transform, skewness [146], and kurtosis has been demonstrated, showing that the system is robust and achieves high performance even at low SNR. Based on compressive sensing, frequency-hopping signals can be effectively identified using a small number of measurements [147]. However, this needs to be given the hop interval.

On the other hand, frequency hopping recognition speed is important, especially in systems that rely on FHSS technology. In FHSS systems, the transmitting and receiving devices change frequencies rapidly in a pre-defined pattern. If the receiver cannot recognize and synchronize with the changing frequencies quickly enough, the signal may be lost, resulting in data loss and communication delays, which reduce the efficiency of the communication system. Hence, the faster a system can recognize the hopping pattern and the header for The better it can maintain communication in hostile environments. It becomes harder for attackers to disrupt the signal. An effective approach to address this challenge is photonic time stretch, which enables real-time processing of high-bandwidth signals that are too fast for conventional electronic systems to handle. PTS can slow down the fast-changing signals in real time and make it possible for further digital processing and classification.

Over the past decade, machine learning based on artificial neural networks (NNs) has developed rapidly. Among various machine learning methods, reservoir computing (RC), a special variant of RNN, has emerged as an alternative to gradient-descent-based training of recurrent neural networks [28]. It is a lightweight, energy-efficient, and computationally efficient machine learning technique. It is particularly suitable for processing time-gated one-dimensional data. It significantly reduces computational cost compared with traditional RNNs during both training and inference. Up to now, RC has been used in cell classification and indoor real-time user localization.

Hence, in this work, A novel real-time mm-wave signals frequency-hopping identification approach that combined PTS and RC for detecting and classifying fast-changing frequency-hopping signals over long-distance fibre links is developed. RC is used to identify the blind signals in the receiver. Through comparison with STFT, RC can recognize frequency-hopping mm-wave signals in real-time, instead of getting all the measured data. The numerical simulation shows that RC-assisted

frequency identification is suitable for hopping time estimation and recognizing the central frequencies of the received hopping signals. This approach demonstrates the ability to maintain high classification accuracy even after long-distance transmission, offering a scalable and efficient solution for real-time detection of fast-varying signals in applications such as wireless communications, radar, and distributed sensing.

3.3.2 Principle and Methodology

In our proposed system, as shown in Fig. 3.8a, in the transmitter, ultrashort optical pulses from a Mode-Locked Laser (MLL) with a repeating of 50MHz, are time-stretched to 12ns by a dispersion compensating fibre (DCF), using a single-mode fibre with 25km. Then the modulated pulses are amplified by an Erbium-doped fibre amplifier (EDFA). The mm-wave signal under test is modulated on the time-stretched optical pulses using a Mach-Zehnder Modulator. Therefore, the optical signal with blind signal carried will propagate using a standard single-mode fibre. Noted that the time-stretched optical pulses should avoid overlap after two long DCF.

Next, modulated optical signals will be sent to a Photodetector (PD) to achieve optical-electric conversion. After PD, the received signal is processed and identified by a reservoir computer, as the input data.

As known to all, training RNN is inherently difficult, while RC has simplified the training process. In an RC model, the input layer and interconnections within the reservoir are fixed. The reservoir is randomly generated. The reservoir is a nonlinear dynamical system that recurrently couples the internal states to each other, and it performs a nonlinear mixing of the input signals into a high-dimensional feature space.

In this work, reservoir computing (RC) is employed in the final stage to process the converted information. As shown in Fig. 3.8b, the converted signal, which

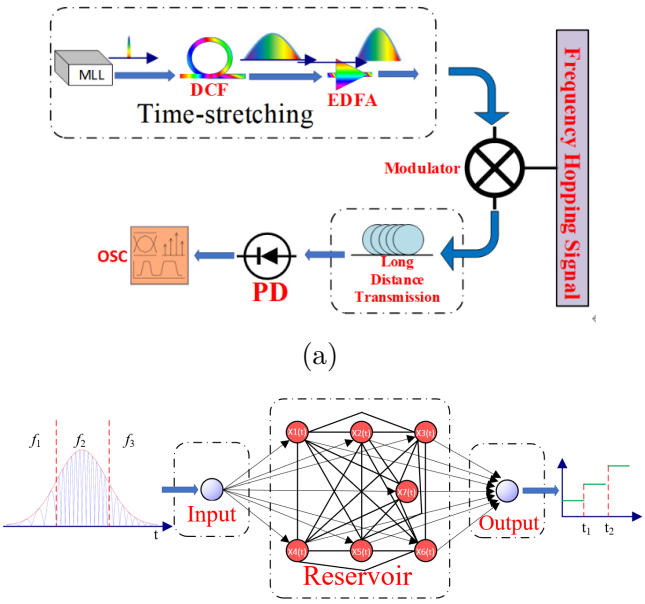

Fig. 3.8: (a)The proposed frequency hopping recognizing system. MLL: Mode-Locked Laser; DCF: Dispersion Fibre; EDFA: Optical Amplifier; SMF: Single-mode Fibre; PD: Photodetector. (b) Topology of the reservoir computer. [[148]]

contains frequency information, is fed into the reservoir for processing.

In this simulation, the full training set, encompassing all potential frequencies, is pre-trained. The input signals to be classified contain different frequencies, which are processed by RC to generate classified labels. Each label corresponds to a specific frequency, with this encoding established during the training phase. Consequently, at the output layer, the identified signal exhibits a predefined output amplitude corresponding to its assigned label.

3.3.3 Simulation results

In the simulation, the reservoir computing system is implemented as a software-based ESN. The reservoir consists of 100 internal nodes with randomly generated sparse recurrent connections. The spectral radius is set to 0.9 to ensure fading memory dynamics, and a tanh activation function is used for nonlinear state

update. Only the linear readout layer is trained using ridge regression.

The input to the reservoir is the time-stretched microwave waveform obtained from the wavelength-to-time mapping process. For each hopping configuration, the waveform is sampled into 200,000 time points and sequentially injected into the reservoir. The internal reservoir states are recorded over time and arranged into a state matrix. During training, labeled carrier frequencies are assigned to each hopping segment, and the readout weights are computed using ridge-regularized least squares.

During testing, the trained readout layer maps the reservoir states to output values corresponding to predefined frequency labels. The final identified frequency is determined by selecting the output neuron with the maximum response within the 3 dB detection region.

In this simulation, we have set different mm-wave signals with different hopping times, as shown in Fig. 3.9 (a-d). Fig. 3.9 (a-d) has shown 4 different hopping combinations, mainly 30G, 40G, 60G, and 80G. The mm-wave signals under the Gaussian envelope have different amplitudes. This may influence the accuracy of the recognizing. Hence, to get a more precise identification accuracy, in this simulation, the detection region within 3db is mainly conducted.

This simulation is conducted using VPI Photonics and MATLAB. The frequency hopping signal is generated by MATLAB script, and then modulated to the light in VPI Photonics. The received mm-wave signals are classified by RC to get the instantaneous frequency and the hopping timing in the receiver. As for the process of RC identification, it contains two parts: training and testing. In this simulation, a one-shot training is adopted. All the potential frequencies are trained in advance. The linear output matrix has also been calculated. As for the testing part, the update status calculated by testing data and the trained output weight can get the final output. The testing data sheet is about a 1x350000 matrix. According to the simulation setting, we have set the frequency hopping

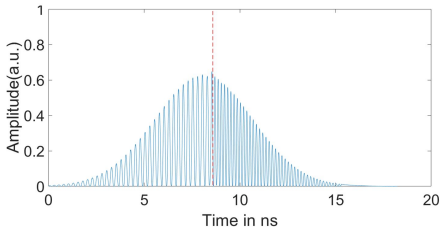

(a) Two-frequency hopping between 40 GHz and 60 GHz.

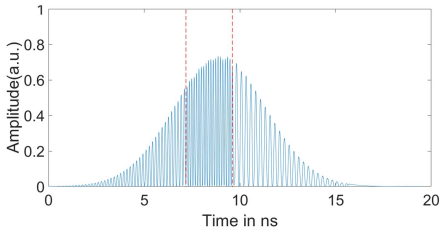

(b) Three-frequency hopping among 60 GHz, 80 GHz, and 40 GHz.

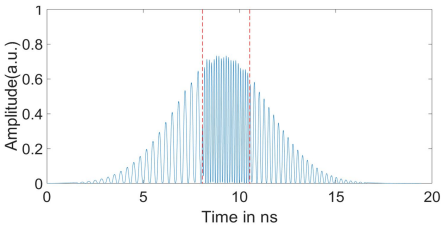

(c) Three-frequency hopping among 30 GHz, 80 GHz, and 40 GHz.

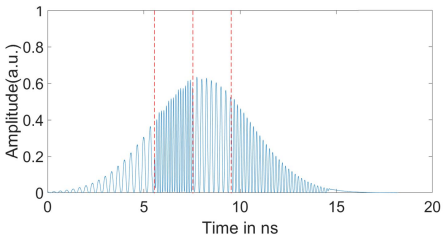

(d) Four-frequency hopping among 30 GHz, 80 GHz, 40 GHz, and 60 GHz.

Fig. 3.9: Time-stretched frequency hopping signals under different configurations.

model with different frequencies, shown in Fig. 3.9.

Two methods have been adopted to identify the instantaneous frequency of the mm-wave signal, RC identification and STFT. The identified result has shown in Fig. 3.10 (a-h).

Fig. 3.10 has shown the result identified by RC and STFT. We can get the frequencies of the mm-wave signals easily. In addition, we can also get the frequency duration time from the hopping time, among these four occasions. The hopping time can get as follows: Fig. 3.10a. 8.5193ns; Fig. 3.10c. 7.1982ns, and 9.6107ns; Fig. 3.10e. 8.0786ns, and 10.5609ns; Fig. 3.10g. 5.5587ns, 7.6348ns, and 9.5847ns. In contrast, the frequency hopping time recognizing by STFT: Fig. 3.10b. 8.5312ns; Fig. 3.10d. 7.4375ns, and 9.5625ns; Fig. 3.10f. 8.3125ns, and 10.6875ns; Fig. 3.10h. 5.3125ns, 7.4375ns, and 9.5625ns. The STFT has been adopted as a golden standard for recognizing frequencies, as it has a high accuracy

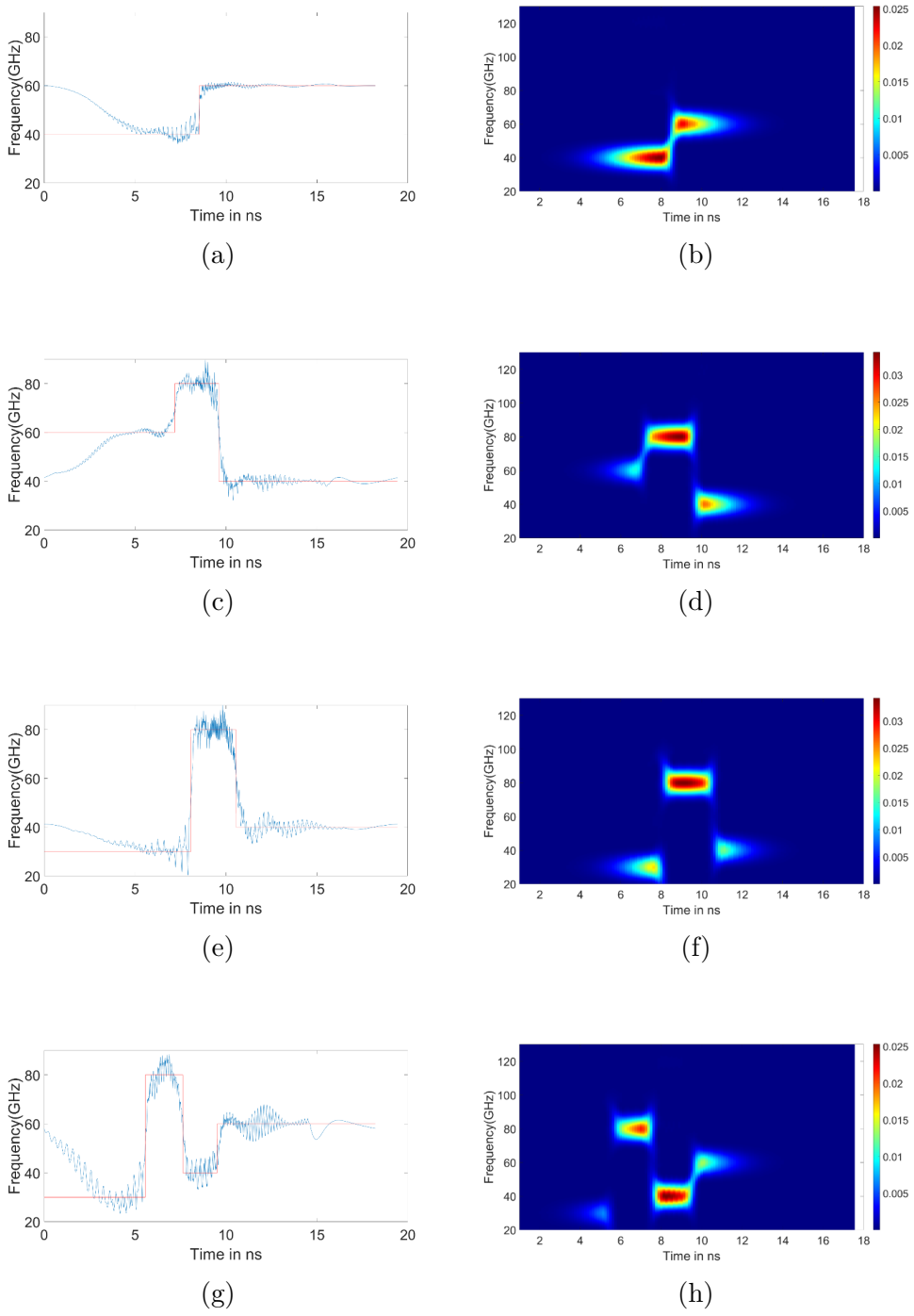

Fig. 3.10: Comparison of hopping time and duration identified by RC and STFT. (a,c,e,g) RC outputs and (b,d,f,h) corresponding STFT spectrograms for different frequency-hopping cases: two-frequency (40, 60 GHz), three-frequency (60, 80, 40 GHz), three-frequency (30, 80, 40 GHz), and four-frequency (30, 80, 40, 60 GHz).

in frequency recognizing. By contrasting frequency hopping time recognizing by STFT and RC, we can get whether the hopping point is accurate or not, and it can also get the accuracy of the identification. Due to the principle of STFT, it needs to get all the data and a sliding time window is created when working. Due to the limitation of the time window length, this may cause a slight error in frequency identification. RC-assisted frequency recognizing method can provide a more fast and precise identification as it can calculate right away when the temporal data arrives.

In addition, according to the simulation results, we can get the central region of the time-stretched pulses has a high sensitivity to the frequency hopping identification. Hence, the envelope amplitude has a major influence on the identification results, and the results have shown that the signal with a higher amplitude has a better identification accuracy. As the mm-wave signal is modulated under a gaussian envelope, and the width of the gaussian envelop is about 12ns. Hence, RC can achieve real-time frequency recognizing at a sub-nanosecond speed.

3.3.4 Discussion and conclusion

In this part, a frequency hopping recognizing method based on the temporal time-stretch concept and reservoir computing is demonstrated. From the simulation results, we can get that the proposed method can recognize the frequency hopping instants and the hop duration timing. By comparing with STFT, we can get the accuracy of the classification by RC. Compared with STFT, RC can achieve real-time classification as it did not need to get all the data before identification. And it has the advantage over other ANN algorithms, it has a linear readout so it has a simpler training method. Therefore, in this work, we have verified the feasibility of the proposed mm-wave signal frequency hopping identification.

3.4 Summary

In this chapter, we present the application of reservoir computing (RC) in wireless communication. First, we introduce a novel RC-assisted ultrafast user localization system for beam-steering optical wireless communication. Utilizing photonic time stretch of ultrashort optical pulses, this system enables ultrafast, wavelength-controlled beam steering. Instantaneous optical wavelength detection within the sub-nanosecond range is achieved through chirped optical spectral coding and RC-assisted microwave frequency identification. Our results demonstrate that RC is a more efficient and robust approach for ultrafast signal identification. Next, we present a frequency hopping system, where the performance in frequency hopping recognition is compared to the golden-standard short-time Fourier transform (STFT). The results highlight the superior performance of RC, further illustrating its potential applications in wireless communication. These two applications reveal that data is first collected and then processed by RC in a host computer during post-processing, a method referred to as digital RC, as the signal is not processed directly in the optical link. To further enhance processing speed and efficiency, an all-optical RC system is proposed in Chapter 4.

Chapter 4

All-optical Reservoir Computing based on Spectral Mixing and Photonic Time-stretch

In Chapter 3, I introduced and demonstrated two applications of reservoir computing (RC) for processing data collected by an optical system: an indoor user localization system and frequency hopping recognition. RC was utilized in the post-processing stage, demonstrating its capability to efficiently process time-gated data with low computational cost. However, in these applications, RC was implemented on a host computer for data processing and classification, relying on offline computation. This approach, referred to as digital RC (as discussed in Chapter 3), can be time-consuming and computationally inefficient.

To overcome the processing speed limitations of digital RC, this chapter presents a novel all-optical RC system that integrates photonic time stretch (PTS) and spectrum mixing techniques. The high-speed processing capability of PTS enables real-time computation by performing operations entirely in the optical domain. This novel approach, termed PTS-based RC, significantly enhances processing efficiency.

This chapter begins by introducing the proposed all-optical RC system, followed by an overview of the fundamental concepts of spectrum mixing, along with both theoretical and experimental validation. Next, the methodology—comprising simulation and experimental verification—is detailed to assess the feasibility and effectiveness of the proposed approach across various tasks. The simulation study also explores parameter optimization to achieve improved performance. This work represents a significant step toward faster and more efficient reservoir computing for real-time applications.

4.1 Introduction

With the advancement of photonic technologies [17, 18, 22], increasing interest has emerged in photonic-based information processing. Photonic Time Stretch (PTS) enables the capture and processing of rapid events in real-time [41]. However, it generates vast amounts of data, creating an urgent need for more efficient processing methods. RC has emerged as a promising solution due to its low energy consumption, inherent parallelism, and rapid processing capability [31, 85]. Unlike conventional recurrent neural networks (RNNs), which suffer from vanishing or exploding gradients [26, 82], RC offers a simpler structure with fixed reservoir weights, which significantly reduces training time and enhances processing speed.

RC is categorized into two main types: Spatially Distributed RC [98] and Delay-Based RC [101]. While Spatially Distributed RC provides robust processing capabilities, it requires numerous physical devices, resulting in increased system cost. In contrast, Delay-Based RC is more practical because it leverages time-delay mechanisms to create large-scale reservoirs with fewer physical nodes, as discussed in Chapter 2. Due to its computational simplicity, Delay-Based RC has been successfully implemented in optoelectronic and all-optical systems, demonstrating strong performance in tasks such as time-series prediction and classification.

PTS enables analog slow-motion processing of optical temporal data by stretching ultrashort optical pulses through a dispersive element, establishing a mapping between wavelength and time [41]. This capability makes PTS a promising framework for integrating RC. However, existing reservoir computing approaches, including delay-based and spatially distributed methods, cannot be directly integrated with PTS because of limitations in node scalability and computational efficiency [59].

To address these limitations and meet the demands of high-throughput and ultrafast processing, this chapter proposes a novel framework: All-Optical Reservoir Computing Based on Spectrum Mixing (PTS-based RC). This approach represents the core methodological contribution of this thesis. Unlike conventional delay-based or spatially distributed reservoir architectures, the proposed system directly exploits the wavelength-to-time mapping mechanism of photonic time stretch (PTS), enabling wavelength channels to function naturally as scalable reservoir nodes.

This design is particularly important because it removes the node-scaling bottleneck that restricts traditional photonic RC systems. By leveraging spectral mixing, strong interactions are introduced among wavelength components, effectively increasing the computational richness of the reservoir without requiring complex feedback loops or large physical node arrays. As a result, the architecture achieves high parallelism, improved scalability, and compatibility with ultrafast PTS operation.

Therefore, the proposed PTS-based RC framework not only simplifies the reservoir structure but also enables real-time, high-throughput signal classification in scenarios where conventional RC approaches struggle to integrate efficiently with photonic time-stretch systems. Further technical details are provided in the following sections.

4.2 Principle of All-optical Reservoir Computing based on Spectral Mixing and Photonic Time-stretch

4.2.1 Principle of All-optical Reservoir Computing

Reservoir Computing (RC) offers a streamlined training process, alleviating the time and computational constraints typical of traditional RNNs. This approach efficiently processes time series data with minimal computational overhead and training costs. Fundamentally, RC maps inputs into a high-dimensional space for pattern analysis and applies a readout mechanism to these high-dimensional states.

In this study, optical techniques are utilized to implement RC with the incorporation of photonic time stretch. Fig. 4.1 outlines the proposed photonic reservoir computing method, which relies on time stretch and spectral mixing. Initially, a short pulse is generated by a mode-locked laser (MLL) and then temporally stretched using a dispersion compensating fiber (DCF). The time-stretched optical signal is then amplified by an Erbium-doped fiber amplifier (EDFA) before being fed into a Mach-Zehnder modulator (MZM).

A typical RC consists of three layers: the input layer, the reservoir layer, and the readout layer. In the input layer, the signal to be classified is masked using an arbitrary waveform generator (AWG) and then modulated onto the optical link. The random mask matrix determines the coupling weights between the input and reservoir layers, and the masked input sequence is repeated at each time interval.

In the reservoir layer, a ring-topology structure updates the reservoir states. Spectral mixing and nonlinearity are introduced via a semiconductor optical amplifier (SOA). After that, the optical signal is then split into two paths: one is collected by a photodetector (PD) for readout, and the other serves as optical

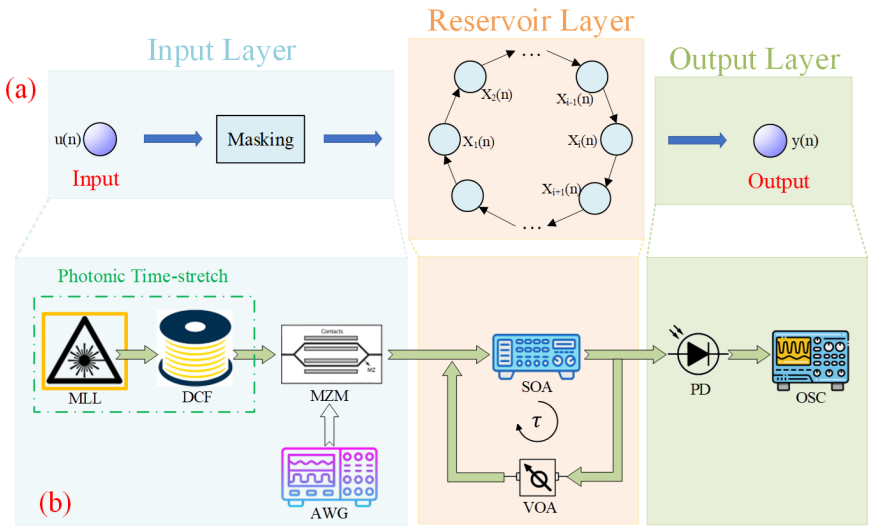

Fig. 4.1: (a) Conceptual architecture of the photonic reservoir computing system with all-optical input masking. (b) Experimental implementation based on photonic time-stretch. Pulses from a mode-locked laser (MLL) are dispersed by a DCF and modulated by a MZM driven by an AWG. The signal is injected into an SOA-based feedback loop and detected by a PD and oscilloscope (OSC). VOA: variable optical attenuator.

feedback. This feedback mechanism acts as the short-term memory function in RC, with its strength controlled by a tunable attenuator.

In the proposed RC architecture, importantly, there exists a direct correspondence between the wavelength and time domains post time-stretching, allowing wavelengths to serve as reservoir nodes. Although an additional phase modulation device was considered at an earlier simulation stage, it was not included in the final architecture because the SOA alone was sufficient to generate the necessary wavelength coupling and nonlinear state evolution.

In this work, to address the limitations of existing photonic reservoir computing (RC) systems with a restricted number of nodes, we propose a novel structure that utilizes wavelength/optical comb lines as nodes, significantly increasing the number of available nodes. This enhancement is made possible by the photonic time stretch technique, which maps wavelength to time.

In the reservoir layer, nonlinear processing is achieved through a semiconductor

optical amplifier, with all nonlinear effects contributing to spectral mixing, thereby enhancing the system's computational capability.

4.2.2 Pre-processing input signal and modulation in the input layer

Typically, before input data is sent to the reservoir, a pre-processing procedure is applied. In the proposed Photonic Reservoir Computing (PRC) system based on spectrum mixing, optical comb lines are selected as reservoir nodes. The system features a ring-topology structure and a delay line, enhancing its processing capabilities.

Typically, in delay-based Reservoir Computing (RC) systems, the conventional masking procedure involves generating and adding masks using arbitrary waveform generators [95]. Here is the Mechanics of Delay Line-Based RC. In a delay line-based RC system, the input signal $x_{in}(t)$ undergoes a sample-and-hold operation every τ, matching the delay duration in the feedback loop. Each input sample is then multiplied by a masking signal m(t), a periodic piecewise constant function with a fixed sequence of N values. These values, selected from a predefined set $m1, m2, \ldots$, define the virtual nodes or virtual neurons spaced by θ, known as the virtual node separation. The schematic is shown in Fig. 2.16 [109]. Hence, the masking procedure is equivalent to a multiplication performed at each time interval.

The masking signal, combined with the nonlinear node's inertia, establishes a virtual interconnection structure that diversifies the virtual nodes' responses to the input signal. This mechanism resembles the role of input weights in traditional neural networks. The optimal design of masking values depends on the specific task and system, although research on their selection remains limited. Some studies suggest using maximum-length sequences for constructing non-random masks [96].

In our work, after PTS, the signal is enveloped by a Gaussian profile. Before

information modulation, the signal to be classified is masked using a binary matrix, as shown in Fig. 4.2. In our system setup, with a pulse period of approximately 20 ns, each Gaussian pulse modulates a single bit, and the masked signal is then used to modulate the optical link.

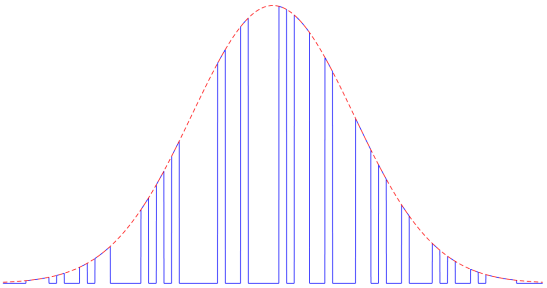

Fig. 4.2: A stretched Gaussian pulse modulated by a binary mask.

4.2.3 Spectrum mixing in the reservoir layer

In this work, to enhance the ability to process real-time time-gated data in reservoir computing without relying on post-processing in a host computer, we have proposed an all-optical reservoir computing scheme. This approach integrates photonic time stretch with spectrum mixing. An introduction to the principles, advantages in real-time information processing, and diverse applications of photonic time stretch has been provided in earlier sections.

To explain spectrum mixing, a brief overview of Four-Wave Mixing (FWM) is necessary. FWM is a nonlinear optical phenomenon where interactions between two or three wavelengths result in the generation of one or two new wavelengths. This effect arises from a third-order optical nonlinearity, described by the $\chi^{(3)}$ coefficient. FWM occurs when at least two distinct optical frequency components propagate simultaneously in a nonlinear medium, such as an optical fibre.

In our implementation of wavelength conversion, we primarily utilize semiconductor optical amplifiers (SOAs). To model FWM in SOAs, we refer to the

work of Zhou et al. [149], who proposed a simplified approach based on coupled-amplitude equations. Their model provides an expression for the output power resulting from FWM in an SOA, which we adopt for this study. The mathematical details of this model will be presented to elucidate the process further:

$$P_{\text{out}}(2\omega_L - \omega_S) = S(\omega_S) \cdot L^2(\omega_L) \cdot G^3 \cdot R(\omega_L - \omega_S) \tag{4-1}$$

Here, S denotes the input power of the modulated signal at the optical frequency ω_S; L represents the input power of the continuous wave (CW) pump (or local oscillator) at the optical frequency ω_L; G is the gain of the semiconductor optical amplifier (SOA), which is assumed to be spectrally flat; R refers to the relative conversion efficiency function; and the pump and signal are assumed to be copolarized.

Assuming two copropagating input frequency components, ν_2 and ν_1 (with $\nu_2 > \nu_1$), a refractive index modulation at the difference frequency occurs, resulting in the generation of two additional frequency components:

$$\nu_3 = 2\nu_1 - \nu_2 \quad \text{and} \quad \nu_4 = 2\nu_2 - \nu_1$$

These newly generated frequencies are illustrated in Fig. 4.3.

Alternatively, other frequency components could be generated, such as:

$$\nu_5 = 2\nu_1 + \nu_2 \quad \text{and} \quad \nu_6 = \nu_1 + 2\nu_2$$

However, these components are less common due to the difficulty of achieving phase matching, particularly in a medium like optical fiber.

Additionally, a pre-existing wave at frequency ν_3 or ν_4 can undergo parametric amplification, where the wave experiences an increase in amplitude through interaction with the pump waves [150].

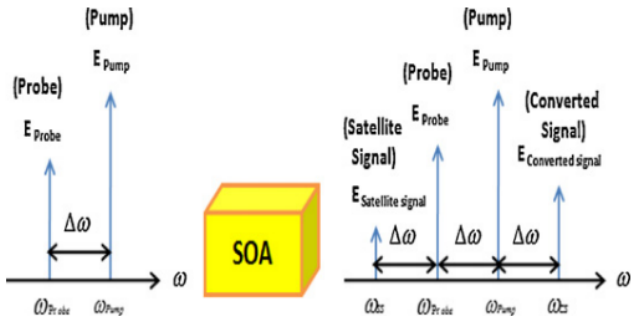

Fig. 4.3: Four-wave mixing (FWM) process in the SOA. A strong pump and a probe wave with frequency spacing $\Delta\omega$ interact in the SOA, generating a new converted (idler) component symmetrically located with respect to the pump. The right panel shows the resulting spectral components after nonlinear mixing.

Four-wave mixing (FWM) plays a crucial role in various applications. For instance, parametric amplification enabled by FWM is employed in fiber-based optical parametric amplifiers (OPAs) and oscillators (OPOs). In these systems, the signal and idler frequencies often coincide. Unlike OPOs and OPAs that utilize nonlinear crystals, fiber-based devices position the pump frequency between the signal and idler frequencies.

In optical fiber communications, FWM can have significant detrimental effects, particularly in wavelength division multiplexing (WDM) systems. It can cause cross-talk between different wavelength channels or lead to imbalances in channel power. A common mitigation strategy is to avoid equidistant channel spacing, which reduces the likelihood of FWM-induced interference.

Conversely, FWM can also be leveraged in WDM telecom systems for wavelength channel translation. In this application, an input signal and a continuous-wave pump at a different wavelength are introduced into a fiber, often a highly nonlinear one. This interaction generates an output signal at a new optical frequency, effectively mirroring the input frequency around the pump frequency. Four-wave mixing can also be applied for phase conjugation, holographic imaging, and optical image processing.

Within the reservoir layer, the selection of wavelengths as nodes is guided by the mapping relations established between time and wavelength in photonic time-stretch. The interconnection of these nonlinear wavelength nodes is facilitated through a semiconductor optical amplifier (SOA) [151]. Spectrum mixing within the reservoir layer is realized through the adoption of the Four-Wave Mixing (FWM) principle. Within the SOA, wavelength conversion is accomplished through FWM. Due to the nonlinear processes in the SOA, two conjugate converted signals (C_1, C_2) are generated (among other products) at wavelengths λ_{C1}, $\lambda_{C2}, \ldots, \lambda_{Cn}$, satisfying the conditions:

$$\frac{1}{\lambda_{C1}} = \frac{1}{\lambda_{P1}} + \left(\frac{1}{\lambda_{P1}} - \frac{1}{\lambda_S}\right), \quad \frac{1}{\lambda_{C2}} = \frac{1}{\lambda_{P2}} + \left(\frac{1}{\lambda_{P2}} - \frac{1}{\lambda_S}\right)$$

Hence, this makes the adjacent wavelengths undergo energy conversion, resulting in spectrum mixing.

To test the consistency and nonlinear changes before and after spectrum mixing, we conducted an experiment. The results, shown in Fig. 4.4, demonstrate that the same injection bits produce consistent responses across periods and maintain the same response before and after nonlinear amplification. Additionally, different bit modulations indicate that nonlinear amplification affects the amplitude output after spectrum mixing.

To further improve the dynamics in the reservoir layer during spectrum mixing, we chose the asymmetric solution for feedback in our experimental setup. The period of the ultrafast pulse and time-stretched pulses is typically 20 ns, with a feedback length set to approximately 40 ns. We also tested the memory capacity, as shown in Fig. 4.5.

As a characteristic of the asymmetric solution, the previous circle information is added to the third period with a 40 ns delay. This memory capacity can extend feedback fading by about two more periods, enhancing the nonlinear process performance in the reservoir layer.

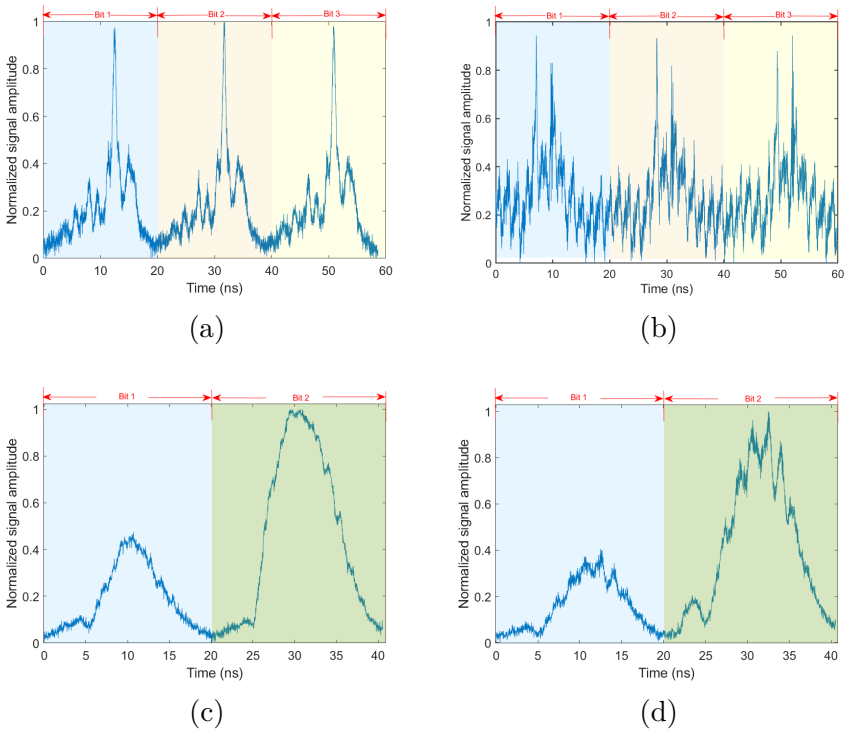

Fig. 4.4: Experimental measurements demonstrating system consistency and nonlinear influence in the photonic reservoir computing system. (a), (b) Measured time-domain responses for identical input bit sequences before and after spectrum mixing, demonstrating the consistency of the system. (c), (d) Measured responses for different input bit sequences before and after spectrum mixing, illustrating the nonlinear influence introduced by the SOA-based spectral mixing. The shaded regions indicate individual bit durations. All waveforms are normalized to their maximum amplitude.

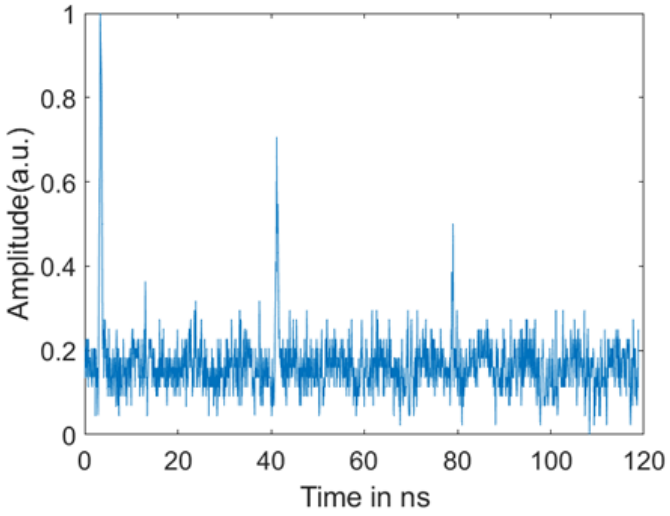

Fig. 4.5: Measured memory capacity of the photonic reservoir computing system, where the feedback loop period is fixed at 20 ns. The memory capacity characterizes how long the input information is retained in the reservoir layer in terms of the number of feedback loop round trips.

However, this conventional masking method often requires higher equipment bandwidth due to the addition of masks via arbitrary waveform generators. As previously mentioned, the mask matrix remains constant to enrich the dynamic states within the reservoir layer. Typically, in conventional implementations, digital masks such as binary random signals and six-level signals are added using arbitrary waveform generators [152].

In the following section, we will provide more details on how this method operates across different tasks. Additionally, the impact of various parameter settings on performance optimization in simulations will be analyzed.

4.3 Simulation Investigation

4.3.1 simulation with different tasks

In this section, we employ three tasks to validate the feasibility of the proposed all-optical RC system: basic waveform classification, frequency classification, and

spoken-digit classification. Each of these tasks involves time-series analysis, and their performance is quantitatively evaluated using the Normalized Mean Square Error (NMSE) between the reservoir output and the expected values for the test data. The NMSE is defined as follows:

$$\mathrm{NMSE} = \frac{\left\langle (y(n) - \hat{y}(n))^2 \right\rangle_n}{\left\langle (\hat{y}(n) - \langle y(n) \rangle)^2 \right\rangle_n} \tag{4-2}$$

where $y(n)$ is the reservoir output, and $\hat{y}(n)$ is the target output. $\langle \cdot \rangle_n$ denotes the average over the discrete time steps. The NMSE is always a positive value, with lower NMSE values corresponding to better performance.

The basic waveform classification is to distinguish between rectangle waves and triangular waves. This classification is vital for various practical applications like signal processing, medical diagnosis, and detection. High-accuracy classification facilitates valuable information extraction and decision-making, crucial for advancing wave-based reservoir computing.

In this simulation, we generate 30 waveform data sets for each type, totaling 60 waveform data sets. For training, we utilize 20 rectangle waves and 20 triangular waveform data sets, reserving the remaining 10 groups for testing, as depicted in Fig. 4.6. Given the relatively straightforward nature of the basic waveform, our selected training and testing datasets suffice to evaluate the proposed system's performance.

In machine learning and deep learning, classification tasks are typically categorized as either single-output or multi-output. In single-output tasks, the model generates a scalar prediction or decision, whereas multi-output tasks require the model to produce multiple values or labels simultaneously. In our work, we adopt a single-output strategy for basic waveform and frequency classification tasks, and a multi-output strategy for spoken-digit classification.

For basic waveform classification, the single-output approach is used during

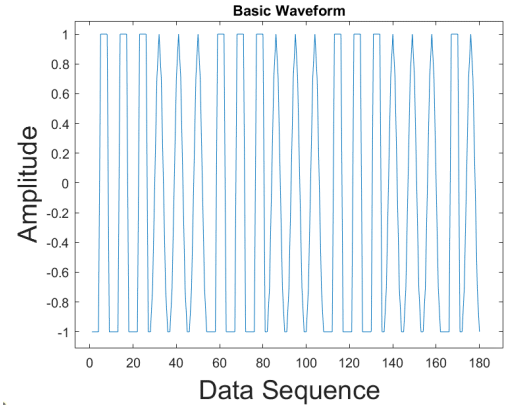

Fig. 4.6: The testing data of basic waveform classification task.

training to compute the output weights, as illustrated in Fig. 4.7. These weights can take on both positive and negative values, which is a natural consequence of various influencing factors, including the underlying principles of reservoir computing, the training methodology, and the mathematical characteristics of the model. For example, in linear regression, the output weights (i.e., regression coefficients) may be positive or negative depending on the data distribution—a negative weight indicates that the corresponding input feature is inversely correlated with the target output.

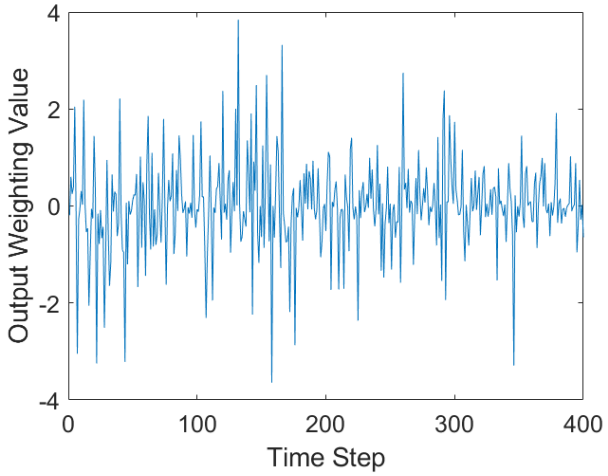

Fig. 4.7: Output weights obtained after training the reservoir computing model for the waveform classification task.

Before presenting the classification results, the procedure used to obtain these results is briefly described. The input waveforms are first encoded into the reservoir through the photonic time-stretch system. After time stretching, the optical signal is sequentially sampled, where each sampling point corresponds to a virtual node in the reservoir. In this way, the temporal waveform is transformed into a high-dimensional sequence of reservoir states. During the training stage, labelled waveform data (square waves and triangle waves) are injected into the reservoir. The resulting reservoir states are recorded and used to determine the output weights through a supervised learning process. Once the output weights are obtained, the trained system can process new input signals and generate predicted outputs.

Fig. 4.8 shows the classified output of the trained reservoir computing system. The blue curve represents the classified values, while the orange curve indicates the ground truth. In this binary classification task, two classes—A and B—are distinguished based on the system output $y(t)$. If $y(t)$ exceeds a predefined threshold (e.g., 1.5), it is classified as Class A (assigned a value of 1); otherwise, it is classified as Class B (assigned a value of 2). As shown in Fig. 4.8, the predicted values closely cluster around 1.0 and 2.0, corresponding to the two target classes. The Normalized Root Mean Square Error (NRMSE) is calculated to be approximately 0.0594, indicating strong classification accuracy.

In this simulation, 200 random values from a binary set (0, 1) are used as the input mask. In the reservoir layer, the driving signal frequency plays a critical role in spectral mixing. A 20 GHz sinusoidal signal is employed to drive the phase modulator, while the optical feedback ratio is set to 3 dBm, controlled via an optical attenuator. In the readout layer, 200 updated states are collected, and linear regression is applied to generate the final output.

In this simulation, the input mask consists of 200 random values drawn from

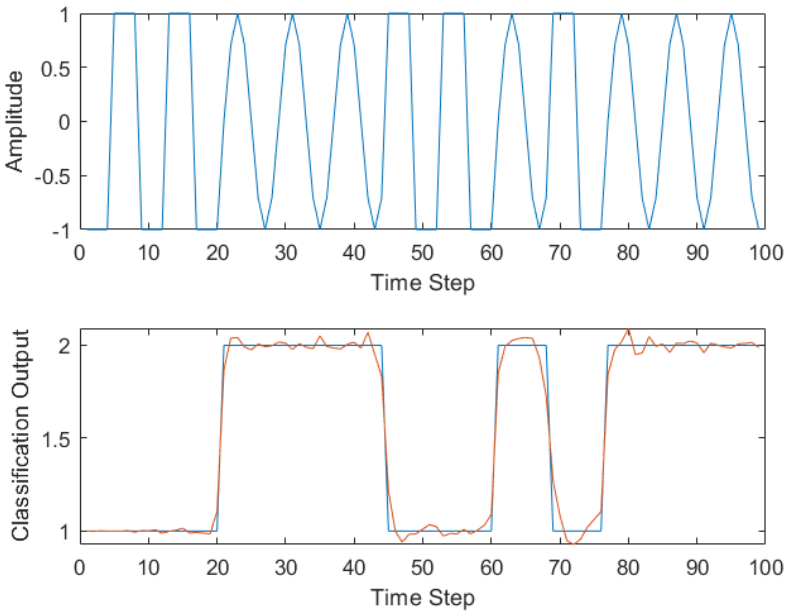

Fig. 4.8: Results obtained for the waveform classification by RC. (a) Square Wave and Triangle Wave.

a binary set (0,1). Each mask value corresponds to one virtual node in the reservoir, resulting in a reservoir size of 200 nodes. This node number was selected as a trade-off between computational complexity and performance in the simulation. Using fewer nodes reduces the reservoir dimensionality and degrades classification accuracy, while increasing the node number beyond this value provides only marginal improvement while significantly increasing computational cost. In the reservoir layer, the driving signal frequency plays a critical role in spectral mixing. In the simulation, a 20 GHz sinusoidal signal is used to drive the phase modulator, which defines the temporal modulation scale of the system. The stretched waveform spans approximately 20 ns in the time domain. With 200 virtual nodes used in the reservoir, the temporal spacing between adjacent nodes is about 100 ps, corresponding to an effective node update rate of approximately 10 GHz. After passing through the reservoir, 200 sequential reservoir states are collected in the readout layer, and linear regression is applied to generate the final output.

Using the procedure described above, waveform signals with different frequencies (50 Hz, 100 Hz, and 200 Hz) are injected into the reservoir to evaluate the classification performance of the proposed RC system. The Normalized Root Mean Square Error (NRMSE) is calculated to assess accuracy, yielding a value of 0.06076. The results demonstrate that the proposed reservoir computing system can successfully classify waveform signals with different frequencies.

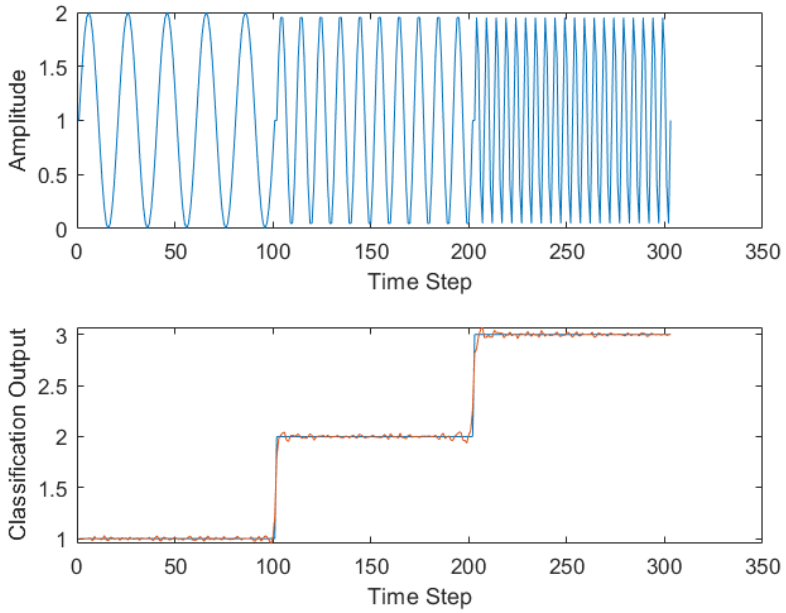

Fig. 4.9: Results obtained for the waveform classification by RC. (a) Square wave and Triangle Wave. (b) Sine wave with different frequencies.

4.3.2 Simulation result with different parameters

Several parameters influence the performance of a reservoir computing (RC) system. In this section, we introduce the key factors that contribute to optimizing system performance. In the proposed all-optical RC system, these include the number of nodes, the drive current of the SOAs, the feedback strength, and the type of input mask. We describe the role of each parameter and present simulation results obtained using VPI Photonics to evaluate their impact on system

behavior.

A fundamental concept in RC—applicable to both physical and delay-based systems—is the number of virtual nodes in the reservoir layer. This parameter defines the reservoir's size and directly affects its computational capacity. Traditionally, the reservoir is viewed as a large, randomly connected fixed network, where each node functions as an independent dimension—similar to neurons in the hidden layer of a neural network—allowing parallel processing across nodes and their interconnections.

Each node dynamically generates and updates reservoir states in response to input signals. During both training and inference, the collective responses of all nodes form the overall reservoir state, effectively projecting input data into a high-dimensional space. Therefore, the number of nodes plays a critical role in determining the complexity and accuracy of the RC system.

To assess the performance of our proposed all-optical RC system based on photonic time-stretching (PTS) and spectrum mixing, simulations were conducted with varying numbers of nodes. The study investigated node counts ranging from 100 to 2000, as illustrated in Fig. 4.10.

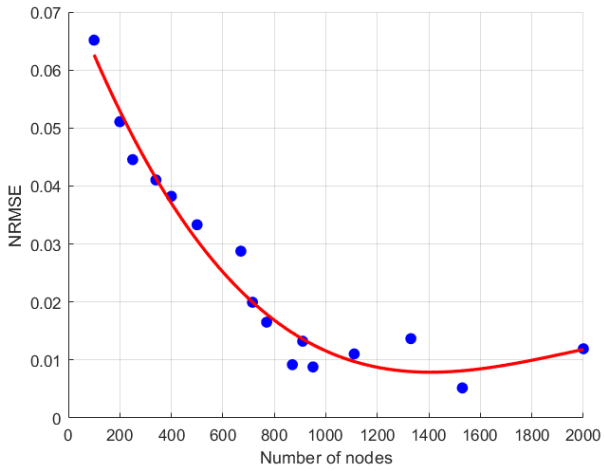

Fig. 4.10: Variation of NRMSE with Number of Nodes.

Fig. 4.10 shows the variation of the normalized root mean square error

(NRMSE) as a function of the number of reservoir nodes. The results were obtained from numerical simulations performed using the VPI Photonics simulation platform. In this study, the reservoir computing system was evaluated using a waveform classification task, where different input waveforms are processed and classified based on the reservoir states.

To investigate the influence of reservoir size on system performance, the number of virtual nodes was gradually increased while keeping other parameters unchanged. For each configuration, the reservoir states were collected and the output weights were trained using a linear regression method. The NRMSE was then calculated to evaluate the prediction performance of the reservoir.

As shown in Fig. 4.10, the NRMSE decreases as the number of nodes increases, indicating that a larger reservoir provides richer dynamical states and improves the system's ability to capture temporal features of the input signal. However, when the number of nodes becomes sufficiently large, the improvement gradually saturates and the curve exhibits a plateau. This behavior occurs because increasing the number of nodes beyond a certain level does not significantly introduce additional independent dynamical information, while the task complexity remains unchanged. As a result, the performance gain becomes marginal.

In general, increasing the reservoir size improves system performance but also leads to higher computational resource consumption. As shown in Fig. 4.10, the NRMSE decreases as the reservoir size increases. To strike a balance between accuracy and computational efficiency, a reservoir size of approximately 400–600 nodes is found to offer optimal performance.

In the simulation, the nonlinearity of the reservoir is introduced by the SOA. A commercial SOA model in VPI Photonics is used to investigate the effect of the SOA drive current. The results in Fig. 4.11 were obtained by varying the SOA drive current while keeping other parameters fixed, and the system performance is evaluated using the NRMSE.

As shown in Fig. 4.11, the NRMSE decreases as the SOA drive current increases. This is because a higher drive current enhances the nonlinear response of the SOA, enriching the reservoir dynamics and improving the computational capability. However, when the current becomes too large, gain saturation occurs and the improvement becomes limited. Therefore, the optimal performance is obtained when the drive current is around 0.8–0.9 A.

Although this study is simulation-based, a rough estimation of the photonic reservoir core power consumption can be made from typical device parameters. The dominant electrical power consumption is expected to arise from the SOA, which would consume approximately 1–2 W for a drive current of 0.8–0.9 A and a bias voltage of 1–2 V. Hence, the reservoir core is expected to operate at the watt level. This estimate does not include the additional power consumption of the laser source or external electronic instrumentation required in a practical experimental implementation.

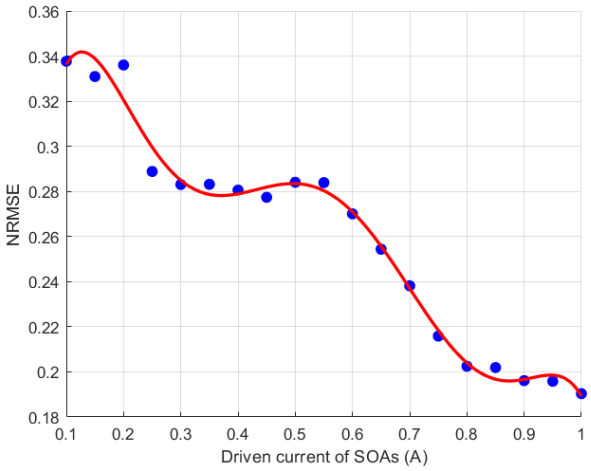

Fig. 4.11: Variation of NRMSE with Driven current of SOAs.

Feedback strength is a critical factor influencing the performance of the system [89]. In delay-based reservoir computing, memory functionality is essential—past reservoir states affect future states within the reservoir layer. This temporal dependency is enabled by optical feedback, which provides a form of short-term

memory known as fading memory.

The strength of this feedback directly affects the reservoir's dynamic behavior and is typically adjusted using an optically tunable attenuator. In this section, we examine the effect of feedback strength on the performance of the proposed all-optical reservoir computing system, as illustrated in Fig. 4.12.

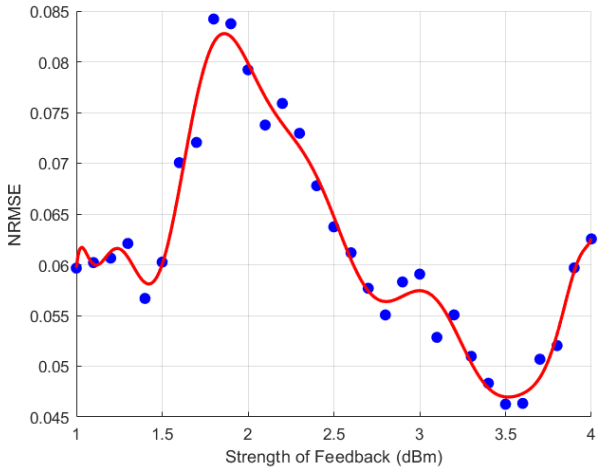

Fig. 4.12: Variation of NRMSE with Strength of Feedback.

The results in Fig. 4.12 were obtained by varying the optical feedback strength in the VPI Photonics simulation while keeping other parameters unchanged. The system performance is evaluated using the NRMSE.

As shown in Fig. 4.12, the feedback strength significantly affects the reservoir dynamics. When the feedback is weak, the memory effect of the system is limited, resulting in poorer performance. As the feedback increases, stronger temporal correlations are introduced, thereby improving the computational capability of the reservoir. However, excessive feedback may introduce instability in the system dynamics. Therefore, the optimal performance is achieved at a feedback strength of approximately 3.5 dBm.

In conclusion, multiple parameters play critical roles in determining system performance. Through careful optimization, both system performance and classification accuracy can be significantly improved. These optimized settings also

provide practical guidelines for system design and experimental implementation.

4.4 Experimental Investigation

4.4.1 Experimental Setup

Following the simulation study that explored the performance of the proposed all-optical system, this section presents the experimental setup used to validate the system for different tasks. Several key devices were employed in the experiment.

For the mode-locked laser (MLL), we selected a commercial model from CALMAR Laser (Product Model: FPL-03CFFUKC), as shown in Fig. 4.13. This device emits invisible laser radiation at a central wavelength of approximately 1550 nm, with an average output power of around 38 mW. It is a compact, user-friendly, passively mode-locked fiber laser that employs a semiconductor saturable absorber to ensure excellent stability and turnkey operation.

The FPL series is a C-band bench-top femtosecond fiber laser offering both tunable (throughout the C-band) and fixed-wavelength versions. It provides front-panel control knobs for flexible adjustment of wavelength, pulse width, and output power. The pulse width is factory-selectable between 0.1 and 15 ps, delivering near transform-limited pulse shapes with a pedestal suppression greater than 20 dB. Timing jitter can be as low as 60 fs. The repetition rate is configurable from 10 to 100 MHz and is available with either polarization-maintaining (PM) or non-PM fiber outputs. With up to 20 mW output power, the FPL series is an economical solution for low-power applications such as amplifier seeding. An RF synchronization output is also available for external triggering.

In our experiment, we use a commercial SOA (Thorlabs SOA1117). The performance is illustrated in Fig. 4.14, which shows both the spectral response and the gain versus output power. From Fig. 4.14a, it can be seen that the SOA operates over a wavelength range of 1410–1660 nm, with a peak at around 1560

Fig. 4.13: C-band Femtosecond Fiber Laser Bench Top.

nm—consistent with typical C-band SOA design. In our setup, the mode-locked laser (MLL) has a central output wavelength of 1550 nm, with a spectral width of approximately 8–15 nm.

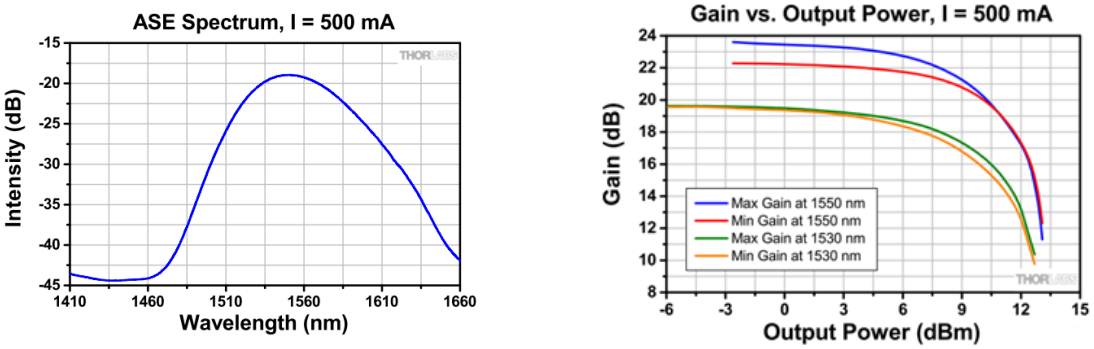

(a) (b)

Fig. 4.14: (a) Amplified Spontaneous Emission (ASE) of SOAs, with 500 mA driven current. (b) Gain vs. Output Power of SOAs, with 500mA driven current.

In addition, other optical components commonly used in commercial systems include EOMs, attenuators, and photodetectors (PDs). Optical amplifiers are also employed in the link when signal amplification is required.

4.4.2 Experimental Results with Different Tasks

In this section, a proof-of-concept experiment has been designed and implemented based on conceptual schematic shown in Fig. 4.1. To verify the proposed RC

scheme, the basic waveform tasks (interleaved square and triangle waves classification) is performed. The corresponding expected output label is set to -1 and 1. The target waveform and output label is shown in Fig. 4.15.

In the experiment, the input waveforms are generated using an AWG and modulated onto the optical pulses produced by the mode-locked laser. The modulated optical signal is then injected into the photonic reservoir system, where nonlinear processing is introduced by the SOA and the temporal dynamics are formed through the optical feedback loop.

The reservoir states are detected by a photodetector and recorded using a oscilloscope. The recorded signals are then transferred to a computer for offline processing. During the training stage, a set of input signals and their corresponding labels are used to train the output weights using linear regression. In the testing stage, the trained weights are applied to new input signals to evaluate the classification performance of the proposed reservoir computing system.

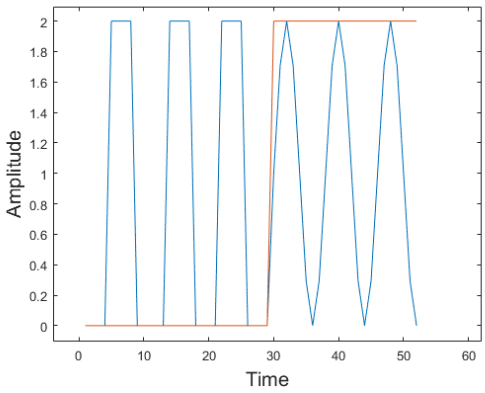

Fig. 4.15: The input data and corresponding output label.

A mode-locked laser (Calmar Mendocino FP laser) is used as the optical source to generate a series of ultrashort (800 fs) broadband (12nm) pulses with a repetition rate of 50MHz. The pulses are time-stretched with -1.04ns/nm dispersion compensating fibre from 800fs to 12ns. In the input layer, 400 random values chosen from a binary set (0,1) are used as the input mask. The binary mask

sequence is first generated digitally and uploaded to the arbitrary waveform generator (AWG). The AWG then applies the mask to the electrical driving signal, which modulates the optical pulses through the phase modulator, thereby implementing the masking operation experimentally. A 20 GHz sinusoidal signal is used to drive the phase modulator. The driven current of SOA is set to 500 mA. In the readout layer, 400 reservoir statuses are collected for each stretched optical pulse is shown in Fig. 4.16a. The linear regression approach is used to calculate the output.

In general, the performance of RC is indicated by the Normalized Mean Square Error (NMSE) between the reservoir output and the expected values for the test data. The NMSE can be described as Eq. (4-2). The NMSE is always a positive value, with lower NMSE values corresponding to better performances. In training phase, 24 waveforms are used. In the testing phase, 4 waveforms are used. The classification result is shown in Fig. 4.16b.

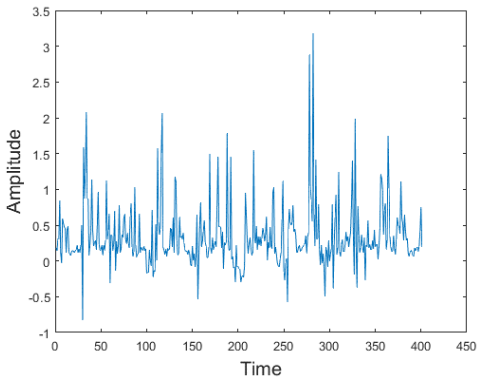

(a) Reservoir output weight.

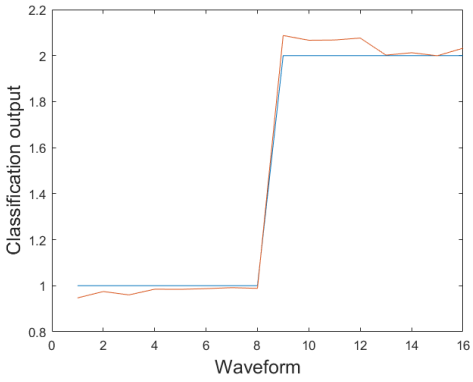

(b) Experiment results for waveform classification.

Fig. 4.16: Reservoir computing waveform classification results.

Fig. 4.16b shows the result of waveform classification for the task. The blue curve represents the target output level. The red curve represents the classified output level. As can be observed in the figure, different waveforms can be classified correctly (Output Label 1 represents square waves, and Output Label 2 represents

triangle waves). The NMSE for this task is 0.14, which is mainly attributed to the limited number of virtual nodes used in the reservoir.

As shown in Fig. 4.17, increasing the number of nodes significantly reduces the NMSE, indicating that a larger reservoir can better capture the temporal features of the input signals and improve the overall performance. The optimal value lies around N = 600. When N is larger, this would cause many more computational resources cost. When N is smaller, the classification performance is decreased. The minimal NMSE is as low as NMSE = 0.098.

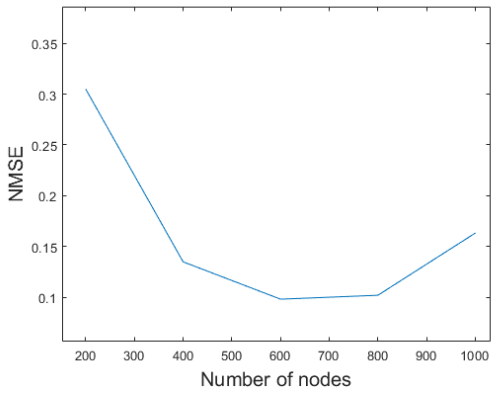

Fig. 4.17: Performance of waveform classification task as a function of number of nodes.

For verifying the performance of the machine learning methods, there may using some standard datasets for training, validation and testing. The datasets have MNIST Handwritten digit recognition, spoken-digit classification and so on. Datasets are an integral part of the field of machine learning. In our work, we choose the spoken-digit classification task to verify the performance of our proposed system. As for this database, a simple audio dataset consisting of recordings of spoken digits in wav format sampled at 8 kHz. The recordings are trimmed so that they have near minimal silence at the beginnings and ends. Free Spoken Digit Dataset (FSDD) is an open dataset, which means it will grow over time

as data is contributed. We conducted a task on isolated spoken-digit recognition, utilizing the widely acknowledged spoken-digit database for evaluating RC system capabilities, sourced from the NIST TI-46 corpus [153]. This dataset encompasses ten spoken digits (0-9), each recorded with ten distinct voices, with temporal waveforms depicted in Fig. 4.18. During the experiment, the spoken-digit signals were first converted into electrical waveforms and played back using an arbitrary waveform generator (AWG). The electrical signals were then used to drive the optical modulator, encoding the speech information onto the optical pulses before being injected into the reservoir. The resulting reservoir states were subsequently recorded in the readout layer.

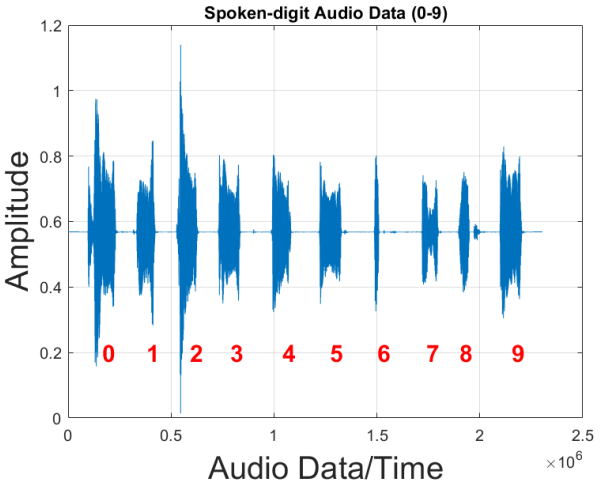

Fig. 4.18: Original audio spoken-digit data (from 0 to 9).

In this experiment, the reservoir size is set to 400 nodes. A symmetric scheme is adopted, that is, the period of the delay is adjusted to be the same as the repetition period of the MLL. The SOAs are adjusted to operate in the nonlinear amplification region. The signal to be classified is the spoken-digit audio data, with ten labels corresponding to digits from 0 to 9. During the experiment, the speech signals are first converted into electrical waveforms and encoded onto the optical pulses through the optical modulator before being injected into the reservoir.

After propagating through the reservoir, the system generates time-series responses corresponding to the reservoir states. These temporal states are detected by the photodetector and recorded for each input sample. The collected reservoir states are then used to train a linear regression readout layer, which performs the final classification. The resulting classification performance is summarized by the confusion matrix shown in Fig. 4.19.

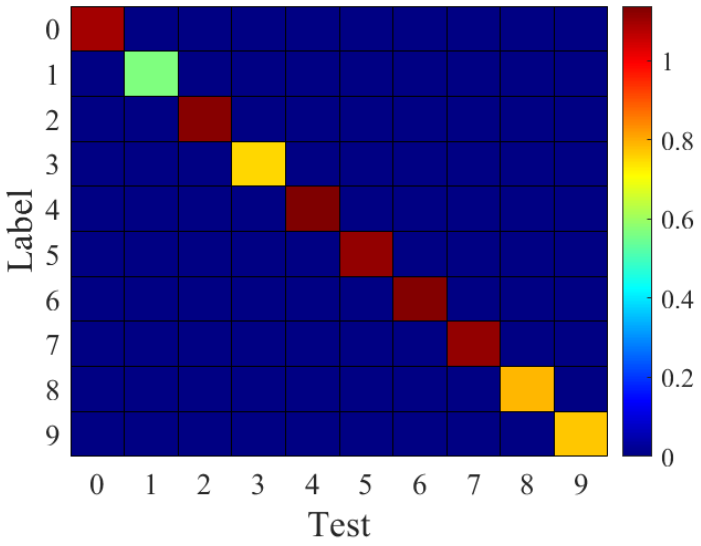

Fig. 4.19: Confusion matrix of spoken-digit classification with a binary mask.

The confusion matrix was computed utilizing the winner-takes-all decision strategy, displayed in Fig. 4.19. This matrix illustrates the proportion of various possible values, with the color spectrum ranging from blue (0) to red (1), indicating better recognition results with higher values on the color bar. From this figure, we can get that the different audio can be classified correctly. The classification accuracy is approximately 95.97%.

In our spoken-digit classification strategy, only the maximum value is chosen for output during the classification stage, disregarding other information. Fig. 4.20 provides further details regarding the distribution of classified outputs among different spoken digits. Analysis of Fig. 4.20 reveals that for digits '0', '1', '2', and

'8', there exists a notable disparity compared to other distributions, suggesting these digits are relatively easier to recognize. Conversely, for digits '1', '4', '5', '6', '7',and '8', the distribution shows less disparity with other digits, indicating a higher difficulty in correct classification. The ease of classification correlates with the values on the color bar in Fig. 4.20.

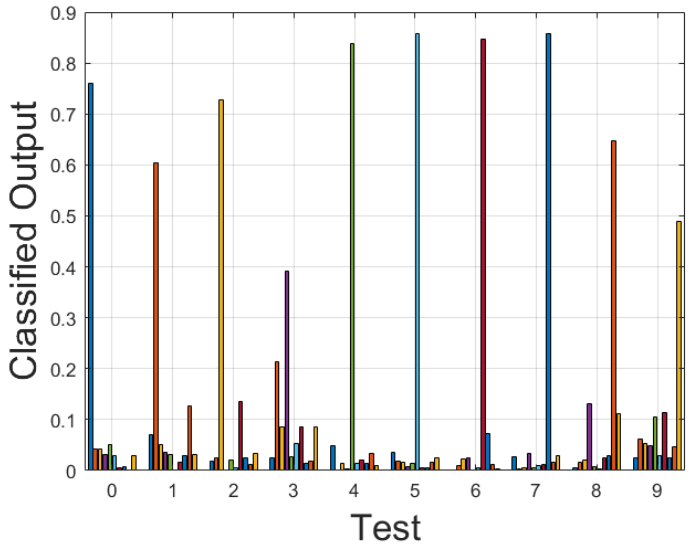

Fig. 4.20: Distribution of the classified spoken-digit audio with a binary mask.

4.5 Summary

This section presents a novel all-optical RC method based on PTS for high-throughput data processing. Simulations demonstrate the effectiveness of this approach, leveraging a SOA in the reservoir layer, where spectral mixing occurs among different wavelength nodes. The proposed all-optical RC scheme achieves strong performance in waveform classification and spoken-digit classification tasks.

Additionally, simulations explore performance optimization by adjusting key parameters such as SOA drive current, the number of nodes, and different masking strategies.

Furthermore, an experimental demonstration of all-optical RC based on time stretch and spectral mixing validates this approach. By integrating photonic reservoir computing with spectral mixing, wavelength nodes are generated within the reservoir layer. A proof-of-concept experiment confirms that the proposed RC architecture enhances waveform classification performance. The relationship between the number of nodes and the NMSE has also been analyzed.

Chapter 5

Photonics Time Stretch Reservoir Computing with an Optical Mask Input

As discussed in the previous chapter, the input masking procedure is a crucial component in delay-based photonic reservoir computing systems because it creates virtual nodes and enhances the dynamic complexity of the reservoir layer.

Traditionally, input masking is performed in the electrical domain using an arbitrary waveform generator (AWG) to add or multiply a mask matrix. However, this method limits the modulation speed and imposes bandwidth constraints on the system.

To overcome these limitations and further enhance processing speed, this chapter introduces a novel all-optical input masking scheme termed the Optical Input Mask Scheme. By shifting masking operations entirely to the optical domain, this approach enables higher-speed processing and removes the bandwidth bottlenecks associated with electronic modulation.

5.1 Introduction

This chapter introduces a novel photonic reservoir computing (RC) framework based on photonic time stretch (PTS) and spectrum mixing, supported by both numerical and experimental validation. The proposed RC structure addresses key challenges in physical implementations, particularly the reliance on numerous physical devices as nodes, which results in increased complexity and costs. To mitigate these challenges, a time-delayed feedback loop with a single nonlinear element is employed, enabling the construction of large-scale reservoirs with precise control over delay times.

In delay-based RC systems, a temporal mask is typically applied to input data to induce complex transient responses before feeding them into the reservoir. This preprocessing step enhances the computational capability of the RC system by disrupting system symmetry and enriching the dynamic states within the reservoir layer. Various masking strategies have been developed to improve system performance, including digital masks—such as binary random signals and six-level digital masks—as well as analogue masks, such as chaotic and colored-noise masks.

Hardware implementations of these masking techniques often require expensive, high-bandwidth electronic devices, which limit their practical scalability. To address this constraint, an all-optical masking approach based on time-stretching and spectral mixing is proposed in this chapter. By leveraging optical spectral encoding, the mask can be incorporated without the need for digital sequence generation or electronic modulation, thereby circumventing electronic bandwidth limitations.

For real-time sequential data processing, high-accuracy and high-speed methodologies are essential. RC has emerged as a powerful tool for real-time, all-optical object recognition in PTS systems, offering significant advantages over conventional electronic computing approaches. In continuous-time input scenarios typical of RC applications, the preprocessing step applies a temporal mask

to generate a complex transient response before inputting data into the reservoir layer.

While digital and analogue masks improve the computational efficiency of RC systems, their hardware implementations necessitate expensive, high-speed electronics, restricting their widespread adoption. The proposed all-optical masking approach, based on time-stretching and spectral mixing, integrates the mask directly into the optical system. This optical approach eliminates electronic bottlenecks, reduces the demand for high-bandwidth electronic components, and enhances processing efficiency. Simulation results demonstrate superior performance in waveform classification using optically implemented masking strategies.

By introducing the optical mask before modulation, the effective bandwidth is significantly increased, as optical processing inherently supports higher bandwidths compared to electronic processing. Additionally, optical-domain operations generally consume less power than their electronic counterparts, leading to improved energy efficiency. The spectral-domain masking technique eliminates the need for power-intensive, high-speed electronic multipliers, further optimizing system performance. Optical spectral processing, operating at the speed of light, enables real-time, ultra-fast data processing with minimal latency.

This chapter is structured as follows: First, I introduce the importance of the optical mask in enhancing processing speed compared to traditional digital masks. Next, I outline the mask's role in the pre-processing stage of photonic reservoir computing, detailing the numerical model and procedure. The core of this chapter explores three optical masking methods. I then describe the experimental implementation of these methods, including parallel diffraction gratings, the MZI-based optical mask, and the SMS fiber structure optical mask. Their effectiveness is evaluated through a spoken-digit classification task to demonstrate the feasibility of optical mask-enabled photonic reservoir computing (RC). Finally, the chapter concludes by summarizing key findings and emphasizing the significance of optical

mask-enabled RC in enhancing photonic time-stretch systems.

5.2 Optical Mask

As discussed in Chapter 4, photonic time stretch, combined with spectrum mixing, serves as a novel all-optical reservoir computing (RC) approach. In the proposed RC scheme, the masking procedure occurs before modulation, posing challenges for electronic devices such as bandwidth limitations and sampling rates. To further enhance processing speed, we optimize the masking procedure by modulating the mask matrix before information is transferred to the optical domain. This method aims to reduce electronic signal delays while leveraging the high-speed processing capabilities of optics.

Due to its advantages, photonic time stretch is widely used in ultrafast signal processing and transient spectroscopy measurements, as it enables high-precision optical spectrum analysis. In general, time stretching establishes a mapping between time and wavelength. This relationship allows optical filtering to be performed in the time domain, which is equivalent to frequency-domain operations—enabling spectral masking. In our work, time stretching is achieved using a mode-locked laser and a dispersive fiber, followed by a tunable optical filter to apply the optical mask.

To analyze this process, the mode-locked laser emits ultrafast pulses, typically in the femtosecond or picosecond range. Ideally, these pulses exhibit a Gaussian shape and a broad spectral range. The dispersive fiber introduces group velocity dispersion, stretching the optical pulse in the time domain. Due to dispersion effects, different frequency components propagate at different speeds, causing high- and low-frequency components to separate over time.

$$t = \beta\lambda \tag{5-1}$$

where t is the signal arrival time, λ is the wavelength (or equivalent frequency component), and β is the dispersion coefficient (related to the fiber length and dispersion parameters).

In the frequency domain, the spectrum shape remains unchanged without nonlinear effects and is still the original broadband spectrum. But the phase characteristics of the light have changed, becoming a linear chirp spectrum, that is:

$$\phi(\omega) = \beta_2 L \frac{(\omega - \omega_0)^2}{2} \tag{5-2}$$

where β_2 is the second-order dispersion parameter, L is the fiber length, and ω_0 is the center frequency.

Then, we introduce a tunable optical filter (TOF) to conduct the spectral masking. It helps selectively preserve or suppress specific spectral components and is equivalent to applying a spectral mask that influences time-domain characteristics.

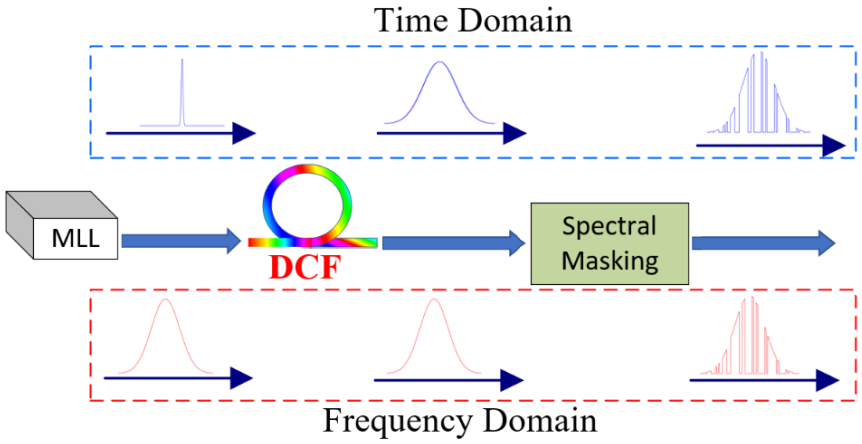

Fig. 5.1: Mapping between the time-domain and frequency-domain.

In the frequency domain, the TOF acts as an optical windowing function, and the shape of its transmission function $H(\omega)$ is determined by the filter settings. After passing through the TOF, the resulting spectrum can be described as:

$$S'(\omega) = S(\omega)H(\omega) \tag{5-3}$$

where $S(\omega)$ is the spectrum after the dispersion fiber and $H(\omega)$ is the transmission function of the TOF. Under this condition, the pulse shape in the time domain is also changed. Fig. 5.2 shows the corresponding response in the frequency domain and time domain.

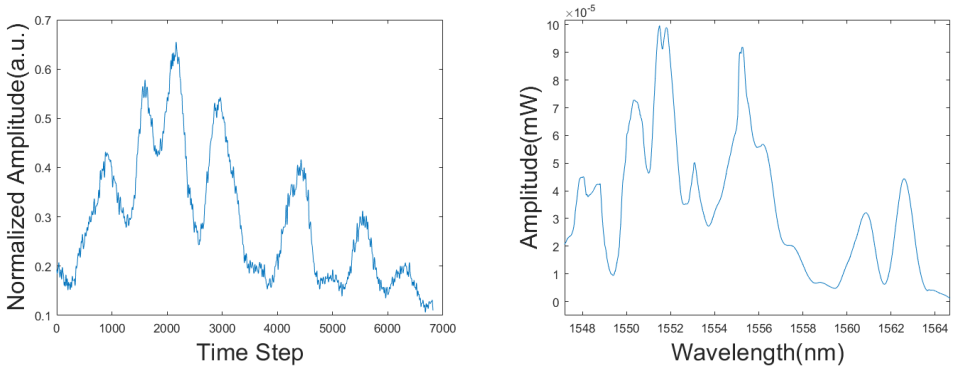

(a) (b)

Fig. 5.2: Spectrum response in time-domain and frequency domain.

This method overcomes the bottleneck of electronic processing by eliminating the need for conversion to the electrical domain, allowing all operations to be performed optically. This enhances processing speed and efficiency.

In the next section, we will introduce three methods for implementing the proposed programmable optical filter.

5.3 Experiment Setup with Different Optical Mask

In this section, we introduce the fundamental experimental setup of our photonic reservoir computing (RC) system, which integrates an optical input mask, as

shown in Fig. 5.3. An optical masking block is placed before the information is modulated. To implement this optical masking procedure, we propose three methods: parallel diffraction gratings, an MZI-based structure, and an SMS fiber structure. For each method, we evaluate the performance of the proposed photonic RC system with the optical mask scheme using different tasks, including basic waveform classification and spoken-digit classification.

In this experimental setup, we utilize an all-optical reservoir computer employing time-stretching and spectral mixing. Our photonic RC scheme employs a mode-locked laser (Calmar Mendocino FP laser) as the optical source, generating ultrashort broadband pulses (800 fs) at a 50 MHz repetition rate. These pulses undergo time-stretching to approximately 12 ns using a dispersion compensating fiber with -1.04 ns/nm dispersion. Subsequently, an optical input mask is applied to the signal after time-stretching. The signal to be classified is modulated via an MZM. Nonlinear interaction occurs within the SOA (Thorlabs SOA1117P), known for its low noise figure and broad spectral bandwidth with significant gain. In this experiment, the driven current of the SOA is set to 350 mA.

5.4 Photonics Reservoir Computing with an Optical Mask

5.4.1 Optical Mask with a Parallel Diffraction Gratings

The core design of the optical mask relies on developing a programmable optical filter. While commercial optical filters such as WaveShaper were considered, their high insertion loss and cost made them less viable. Therefore, we opted for a custom solution based on a parallel diffraction grating structure. This approach converts the in-fiber optical signal into spatial light and uses two diffraction gratings to map wavelength to spatial position.

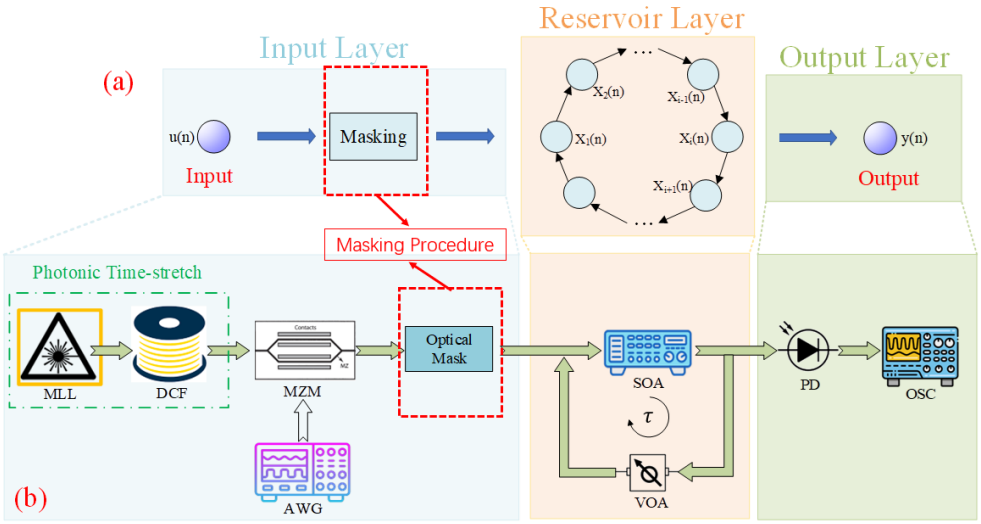

Fig. 5.3: Schematic of the photonic reservoir computer with an all-optical input mask. MLL: Mode-Locked Laser, DCF: Dispersion Compensating Fibre, MZM: Mach-Zehnder Modulator, AWG: Arbitrary Waveform Generator, VOA: Variable Optical Attenuator, SOA: Semiconductor Optical Amplifier, PD: Photodetector, OSC: Oscilloscope.

In our proposed photonic RC scheme, the direct mapping between wavelength and time domains enables an alternative method for implementing temporal masks. According to sampling rules, the optical filter enhances dynamic states within the reservoir layer. One way to apply an optical mask is by using an optical spectral filter with a random binary response to shape the optical spectrum, effectively embedding the binary random mask into the temporal signal. Although we considered a programmable optical filter like Finisar, its high cost and insertion loss made it impractical.

Instead, we propose an optical spectral filter that employs a pair of optical diffraction gratings to spatially disperse the optical spectrum, combined with a spatial mask featuring random binary slots, as illustrated in Fig. 5.4. The broadband optical pulse is dispersed into a rainbow pattern, passing through a fabricated metal platform with slots of varying sizes. These slots correspond to

different sampling intervals in the time or spectral domain. Leveraging the photonic time-stretch effect, this method increases spectral complexity, enhancing the dynamic capabilities of the photonic time-stretch-based RC system. Finally, the mask information is incorporated into the optical domain after passing through the binary metal mask.

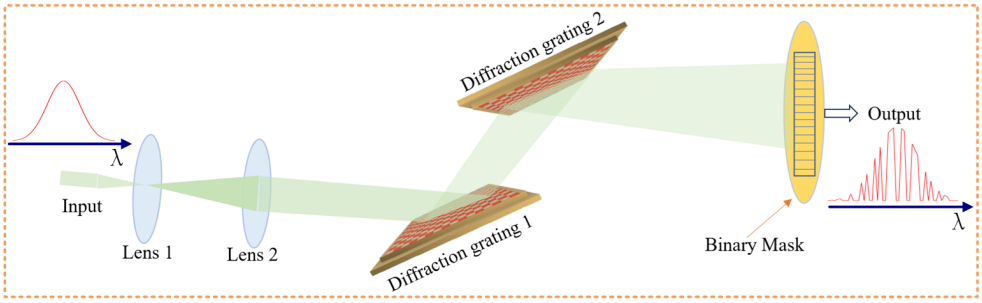

Fig. 5.4: Optical input mask using parallel diffraction gratings.

A diffraction grating is a periodic surface that separates an incident electromagnetic wave into two or more beams [154]. In optics, it is an optical component with a structured periodic pattern that diffracts light or other electromagnetic radiation into multiple beams traveling at different angles, as illustrated in Fig. 5.5 [155]. This property allows diffraction gratings to separate light into its component wavelengths.

There are two types of diffraction gratings: transmission and reflective, both of which can be used across a broad spectral range from the ultraviolet (UV) to the mid-infrared (MIR) [156]. In this work, we utilize reflective diffraction gratings. The diffraction angles of the resulting beams depend on several factors, including the angle of incidence, the periodic spacing between adjacent diffracting elements (e.g., parallel slits in a transmission grating), and the wavelength of the incident light.

A diffraction grating consists of a large number of equally spaced parallel slits [157]. When incident light interacts with the grating, the resulting diffracted light is formed by the interference of wave components emanating from each slit.

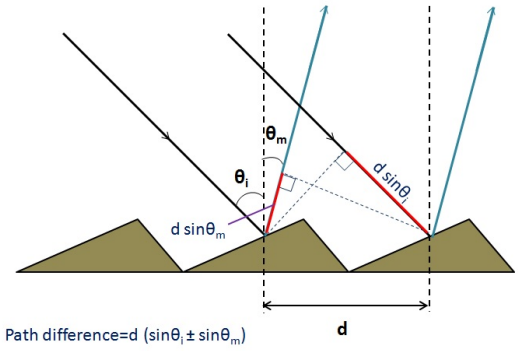

Fig. 5.5: Principle of diffraction gratings for optical masking. Diffraction from a grating with period d generates beams satisfying $d(\sin\theta_i \pm \sin\theta_m) = m\lambda$. The wavelength-dependent angular dispersion spatially separates spectral components, enabling optical masking.

At any given point in space—commonly referred to as the observation point—the path length from each slit to that point varies. Consequently, the phase of the wave emerging from each slit at that location also differs, leading to constructive or destructive interference [158].

When a plane light wave is normally incident on a grating with a uniform period d, the diffracted light exhibits maxima at diffraction angles θ_m, given by a special case of the grating equation [159]:

$$\sin\theta_m = \frac{m\lambda}{d} \tag{5-4}$$

If a plane wave is incident at an angle θ_i relative to the grating normal, in the plane orthogonal to the grating periodicity, the grating equation is given by:

$$\sin\theta_i + \sin\theta_m = \frac{m\lambda}{d} \tag{5-5}$$

This equation describes in-plane diffraction as a special case of the more general phenomenon known as conical, or off-plane, diffraction. The generalized grating

equation for conical diffraction is given by:

$$\sin\theta_i + \sin\theta_m = \frac{m\lambda}{d\sin\gamma} \tag{5-6}$$

Here, γ is the angle between the direction of the incident plane wave and the direction of the grating grooves. This angle is orthogonal to both the grating periodicity and the grating normal. Various sign conventions for θ_i, θ_m, and m exist, and any consistent choice is valid as long as it is maintained throughout diffraction-related calculations.

When solved for the diffraction angle θ_m at which the diffracted wave intensity is maximized, the equation simplifies to:

$$\theta_m = \arcsin\left(\sin\theta_i - \frac{m\lambda}{d\sin\gamma}\right) \tag{5-7}$$

The diffracted light corresponding to direct transmission in a transmissive diffraction grating or specular reflection in a reflective grating is called the zero-order diffraction and is denoted as $m = 0$. The other diffraction maxima occur at angles θ_m for nonzero integer diffraction orders m. The order m can be either positive or negative, corresponding to diffraction on both sides of the zero-order beam.

In our work, the second-order diffraction ($m = 2$) is adopted. The diffraction gratings used in our experiment have 300 grooves per millimeter, resulting in a groove spacing of 3.3 um.

In our setup, a binary random mask is applied by multiplying a Gaussian pulse with the mask in the optical domain. The signal to be classified is then modulated by a Mach-Zehnder modulator (MZM). Nonlinear wavelength node coupling within the reservoir layer is achieved through a semiconductor optical amplifier (SOA), where spectral comb lines act as virtual nodes, facilitating interactions between different neurons.

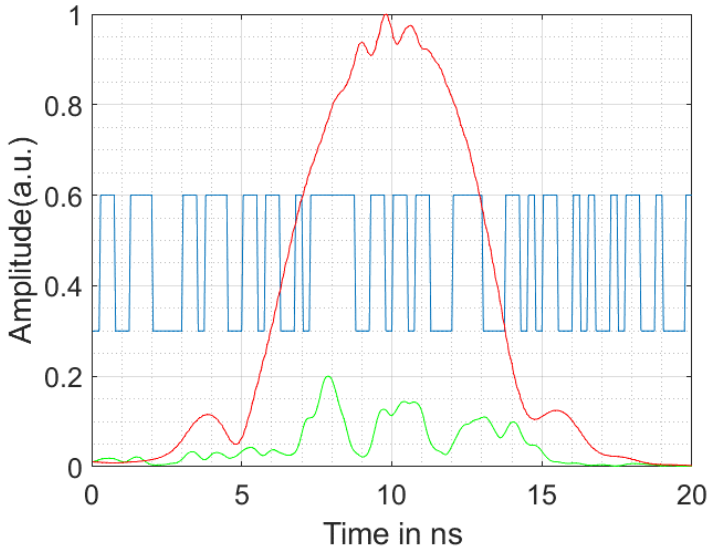

Fig. 5.6: Designed binary optical mask with non-uniform slot widths (blue curve), the time-stretched optical spectrum before masking (red curve), and the resulting spectral response after photonic time-stretching and filtering using parallel diffraction gratings (green curve).

Utilizing a pair of diffraction gratings and a spatial mask, as illustrated in Fig. 5.6, the optical mask has a minimum width of 0.3 mm and is manufactured with high precision. Consisting of 179 binary random values, the mask enhances the dynamic responses within the reservoir layer. The spectral response, also shown in Fig. 5.6, indicates that the spectrum is reshaped through parallel diffraction gratings, effectively functioning as a programmable optical filter.

In the experiment, the setup is depicted in Fig. 5.7. Two diffraction gratings with 300 grooves per millimeter are used, with each groove spaced 3.3 um apart. The mask is fabricated from a thin aluminum sheet. Further details of the mask and its spectral response are provided in Fig. 5.8.

To evaluate the performance of the proposed system, spoken-digit classification was first performed using parallel diffraction gratings. In this setup, we allocated 600 samples for training and 100 samples for testing. An optical mask was introduced into the optical link after the photonic time-stretch stage, as illustrated in

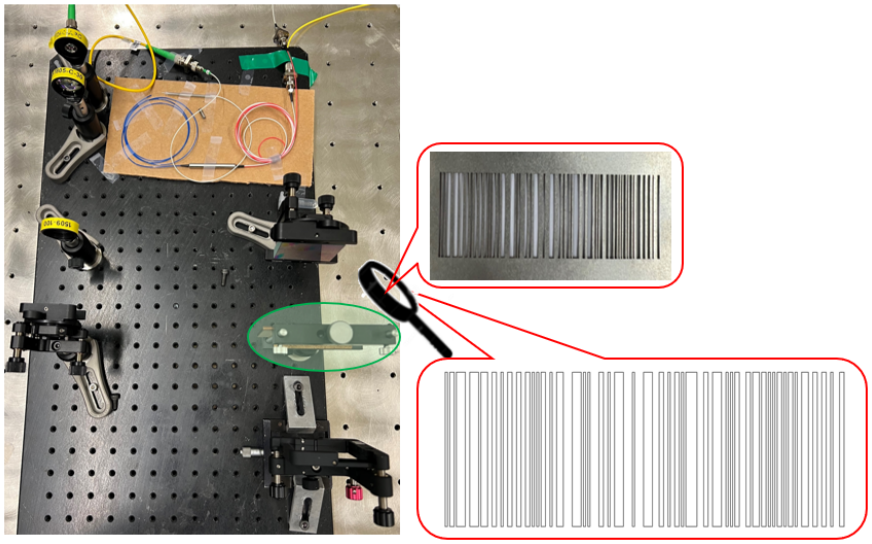

Fig. 5.7: Experimental setup of the parallel diffraction gratings.

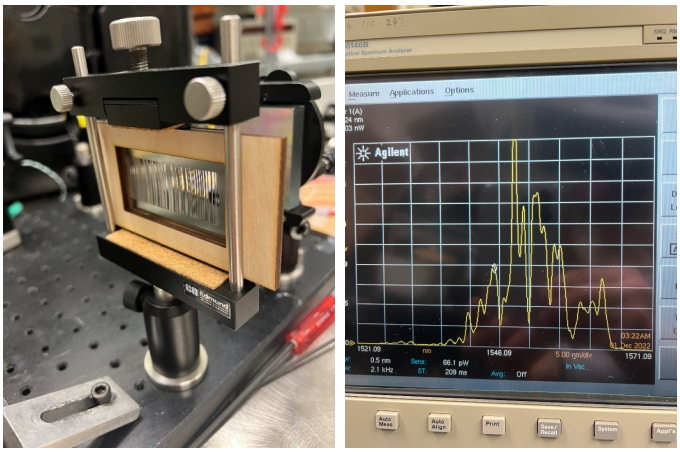

(a) (b)

Fig. 5.8: (a) Photograph of the fabricated optical mask mounted in the experimental setup. (b) Measured spectral response of the optical mask obtained using an optical spectrum analyzer (OSA), showing the wavelength-dependent transmission characteristics.

Fig. 5.4.

For each spoken-digit sample, the corresponding audio waveform is encoded and injected into the photonic reservoir system through the optical mask and parallel diffraction gratings. The reservoir processes the input signal and generates a high-dimensional temporal response consisting of 400 virtual nodes.

The resulting reservoir states are collected and used as features for the linear readout layer. During the training stage, the output weights are obtained using a linear regression method. The trained output weights corresponding to the reservoir nodes are shown in Fig. 5.9. The distribution of positive and negative weights indicates that different reservoir nodes contribute differently to the classification task.

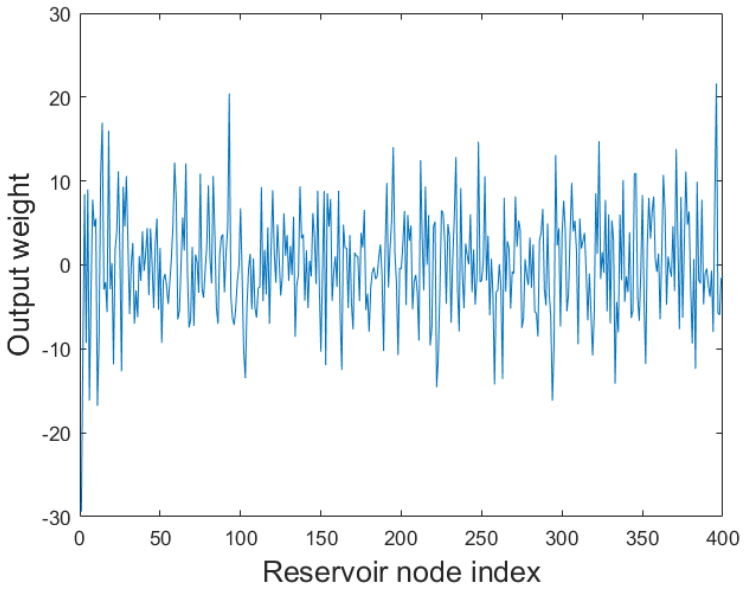

Fig. 5.9: Trained output weights of the 400 reservoir nodes using the diffraction grating optical mask (shown here for digit "1" as an example).

In the testing stage, the trained model is applied to unseen samples, and the final classification decision is obtained using a winner-takes-all strategy. The classification performance is summarized by the confusion matrix shown in Fig. 5.10, where the color scale from blue (0) to red (1) represents the proportion of correctly

recognized samples.

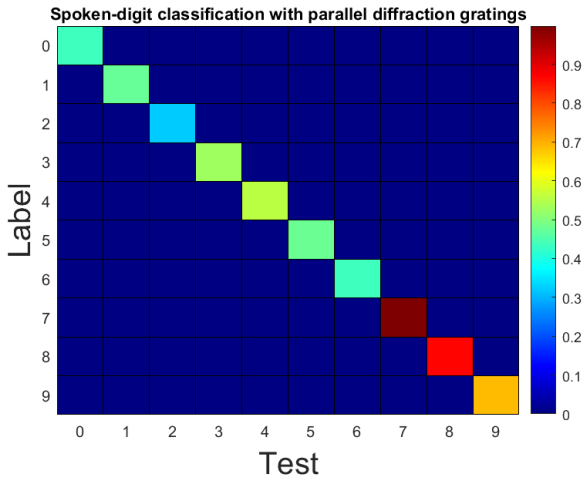

Fig. 5.10: Confusion matrix of spoken-digit classification with parallel diffraction gratings.

In our spoken-digit classification strategy, only the maximum value is chosen for output during the classification stage, disregarding other information. Fig. 5.11 provides further details regarding the distribution of classified outputs among different spoken digits.

Analysis of Fig. 5.11 reveals that for digits '0', '4', '7', and '8', there exists a notable disparity compared to other distributions, suggesting these digits are relatively easier to recognize. Conversely, for digits '1', '2', '5', and '6', the distribution shows less disparity with other digits, indicating a higher difficulty in correct classification. The ease of classification correlates with the values on the color bar in Fig. 5.10.

5.4.2 Optical Mask based on Mach–Zehnder Interferometer (MZI) Structure

However, parallel diffraction gratings are bulky and complex. To simplify the process of applying the optical mask and enhancing dynamics within the reservoir

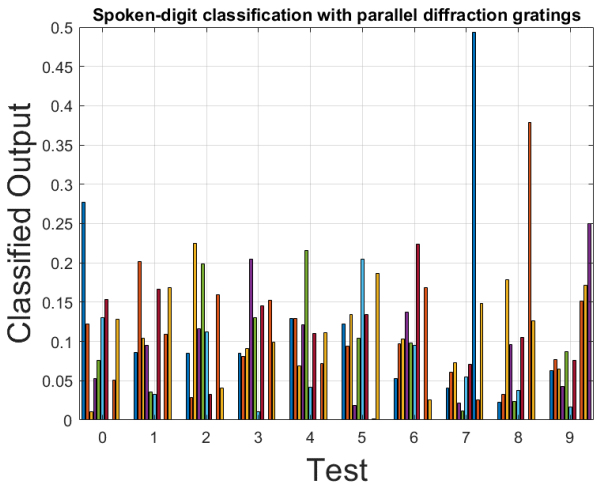

Fig. 5.11: Distribution of the classified spoken-digit audio with a parallel diffraction gratings.

layer, we propose generating the required analog mask using an unbalanced Mach-Zehnder Interferometer (MZI) structure. This non-uniform mask, created by the MZI, significantly improves dynamic states within the reservoir layer, leading to enhanced performance. The MZI-based optical mask plays a crucial role in augmenting the computational capabilities and accuracy of the photonic reservoir computing system.

Building on the previous method, we employ an MZI structure as the optical mask in this study, as illustrated in Fig. 5.12. The MZI structure offers the advantage of generating a high chirp rate by controlling the time delay in one of its arms. As a result, the mask functions as an analog optical signal, further enriching the dynamic states within the reservoir layer. This innovative approach enhances both the computational power and performance of the photonic reservoir computing system.

We assume that the values of the third-order dispersion (TOD) of the two dispersive elements (DEs) are small and can be ignored [161, 162], and only the second-order dispersion (SOD) or group velocity dispersion (GVD) is considered in our analysis. A mode-locked laser is used as the light source. We assume that

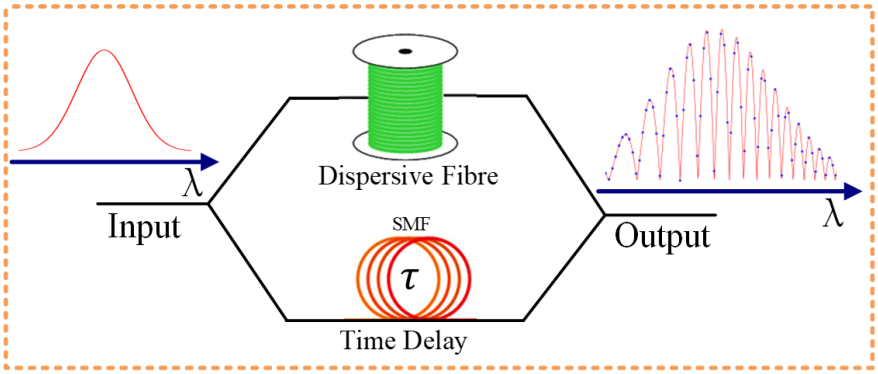

Fig. 5.12: Optical input mask using MZI structure [160].

the peak power of the input pulse is low enough to avoid any nonlinear effects in the DEs. Assume that the input optical pulse is a transform-limited Gaussian pulse expressed as:

$$x(t) = A \exp\left(-\frac{t^2}{2\tau^2}\right) \tag{5-8}$$

where τ is the half pulse-width at maximum. Its Fourier transform is given by [163]:

$$X(\omega) = \tau A\sqrt{2\pi} \exp\left(-\frac{\tau^2\omega^2}{2}\right) \tag{5-9}$$

In this model, a dispersion compensating fiber (DCF) with dispersion value D is used to achieve time-stretch. The ultrashort optical pulse is temporally stretched and spectrally dispersed by passing through the DE. At the output of the DE, the optical signal is expressed accordingly.

To generate a frequency-chirped pulse, we utilize an unbalanced MZI incorporating a single-mode fiber in one arm. Mathematically, the transfer function of an unbalanced MZI incorporating a delay line in one arm can be expressed as [164]:

$$H_2(\omega) = \frac{1}{2}\left[\exp\left(-j\omega t_1 + j\frac{\ddot{\Phi}_v}{2}\right) + \exp(-j\omega t_2)\right] \tag{5-10}$$

where t_1 and t_2 represent the time delays in the two MZI arms, $\ddot{\Phi}_v$ is the second-order dispersion coefficient, and $\Delta t = t_2 - t_1$ denotes the time delay difference. Given that higher-order dispersion is negligible, only second-order dispersion is considered. Hence, an all-optical masking process is integrated into the input layer using an MZI-based optical mask.

Another advantage of employing the MZI-based structure is that it generates a continuous chirped waveform through interference between the two arms with a controlled delay difference. This wavelength-dependent phase modulation produces a smooth frequency-swept temporal profile after dispersion, rather than a discrete binary modulation. Compared to conventional binary masking schemes, the chirped waveform introduces gradual and non-periodic variations in amplitude and phase, which increases the diversity of virtual node responses.

Because the reservoir samples the input according to fixed time intervals, the continuous chirp effectively provides a quasi-random temporal masking without requiring additional electronic modulation. This enhances the richness of the internal dynamic states and improves separability in the readout layer. As shown in Fig. 5.13, the chirp-coded waveform leads to more complex and informative reservoir responses compared to binary masks or diffraction grating–based parallel masking schemes.

The experimental setup is shown in Fig. 5.14. After the stretched pulses were amplified, they underwent high-chirp encoding using an optical delay line (General Photonics VDL001) and a 500 m single-mode fiber (SMF) in a Mach-Zehnder interferometric setup. This process generated a microwave frequency chirp spanning approximately 7 GHz to 29 GHz within the stretched pulse window.

By introducing a dispersion imbalance in the MZI, i.e., creating a difference in chromatic dispersion between the two interferometer arms through unequal fiber lengths—and adjusting the optical delay line, a wideband chirped optical pulse with a tunable frequency offset was achieved. The chirp rate could be further

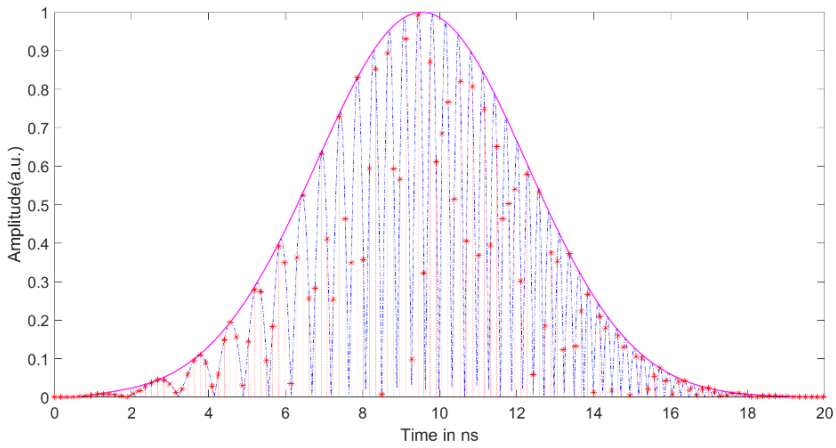

Fig. 5.13: The time-stretched optical pulse after spectral chirp encoding (blue dashed curve) and the uniformly sampled points selected using an optical filter (red dots). The wavelength-to-time mapping enables different spectral components to correspond to distinct temporal positions. A periodic optical filtering operation selects evenly spaced wavelength components, resulting in uniform temporal sampling of the chirped waveform.

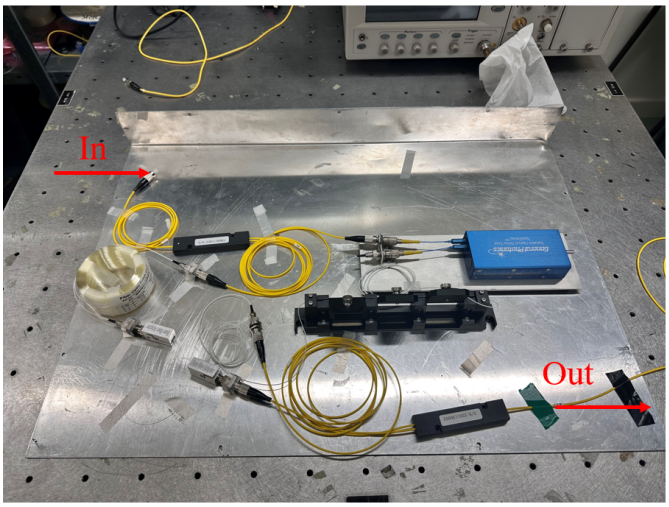

Fig. 5.14: Experimental setup of the Mach–Zehnder interferometer (MZI) used as a programmable optical filter. The input optical signal (In) is first coupled into a fiber splitter and then divided into two arms with a controllable path-length difference. One arm includes a tunable optical delay line, while the other serves as a reference path. The recombined output (Out) generates spectral interference, forming the programmable filtering response. Fiber couplers, connectors, and polarization controllers are used to ensure stable interference.

increased by extending the fiber length, though it was ultimately constrained by the responsivity of the detectors. This approach enabled the establishment of a monotonically increasing RF frequency profile, which was subsequently mapped to both the temporal and optical wavelength domains. As a result, a spectral mapping was created, linking optical wavelength to RF frequency.

The MZI setup encoded the optical pulses using a fixed delay line and a 500 m SMF to achieve a high chirp rate. The time-domain representation of the chirped pulse is shown in Fig. 5.15a, where the chirp slope was determined through spectrogram analysis. By further adjusting the dispersion imbalance and delay line, a tunable wideband chirped optical pulse was achieved. The MZI-based mask enriched the dynamic states within the reservoir. The distribution of sampling nodes is illustrated in Fig. 5.15b. Because the chirped waveform exhibits a monotonic frequency-to-time mapping, different temporal positions correspond to distinct instantaneous microwave frequencies. The MZI-based optical mask performs uniform spectral sampling, which is converted into uniform temporal sampling after dispersion. Therefore, the effective temporal sampling interval determines the resolvable frequency spacing of the chirped signal components.

Next, the stretched pulses are amplified and processed using a high-chirp encoding setup. The non-uniform MZI structure introduces irregular sampling intervals, enhancing the complexity within the reservoir layer.

In summary, this section describes the experimental setup for photonic reservoir computing (RC) and optical masking using diffraction gratings and an MZI structure. To assess the performance of the proposed photonic RC system with an optical mask, we conducted two classification tasks: waveform classification and spoken-digit classification. For both tasks, a "winner-takes-all" decision strategy was employed, selecting the highest value from the recognition confusion matrix as the classification result, representing the most probable class.

To initially validate the system's performance, we conducted basic waveform

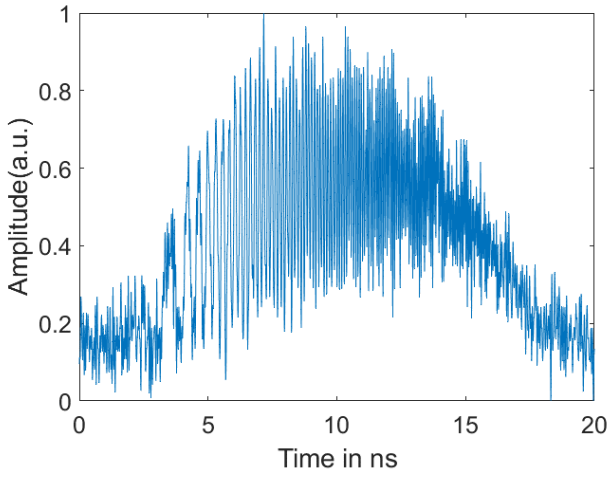

(a)

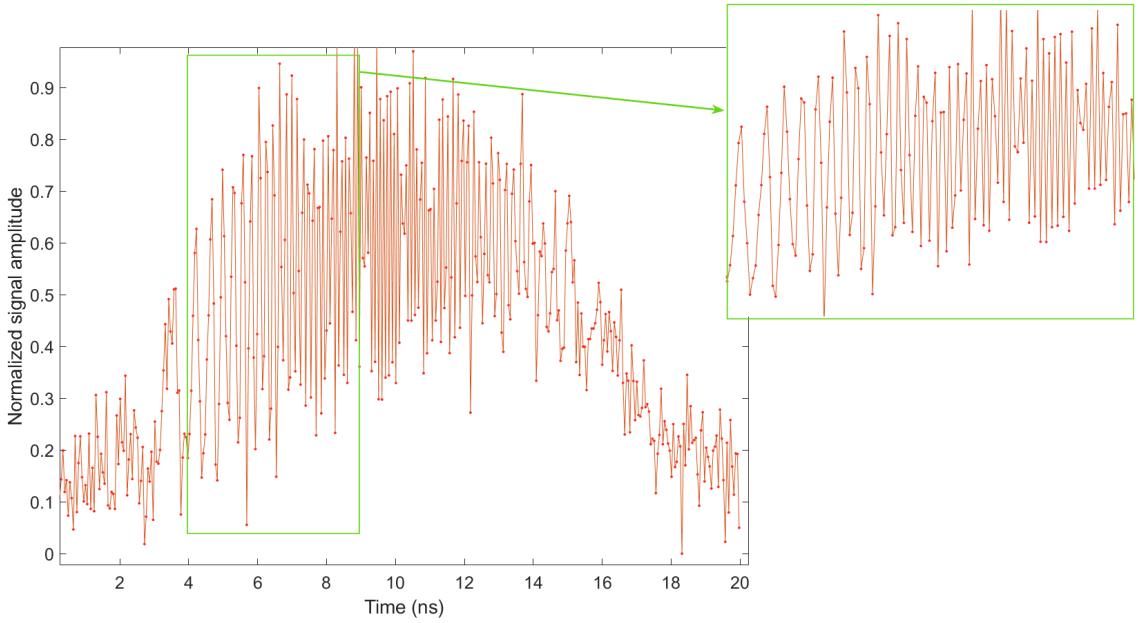

(b)

Fig. 5.15: (a) Measured time-stretched optical pulse after spectral chirp encoding using the unbalanced Mach–Zehnder interferometer (MZI). (b) Corresponding reservoir node states generated by the MZI-based optical mask, showing non-uniform sampling in time. The highlighted regions emphasize the irregular sampling intervals introduced by the unbalanced MZI, which enrich the reservoir dynamics.

classification. Fig. 5.16 illustrates the results, where the readout layer is configured with two output levels: output 1 for rectangular waves and output 2 for triangular waves. Despite minor fluctuations, the system accurately recognizes and correctly classifies both waveform signals, demonstrating its effectiveness. For the basic waveform classification task, square and triangular waveforms are used as input signals. After passing through the photonic reservoir system, the resulting reservoir states are collected and processed by a linear regression readout layer. The readout layer generates an output value corresponding to each input waveform, which represents the predicted class label. The reference output level represents the expected classification label for each waveform, while the classified output level corresponds to the predicted label obtained from the trained readout layer. By comparing these two curves, the classification performance of the proposed system can be evaluated.

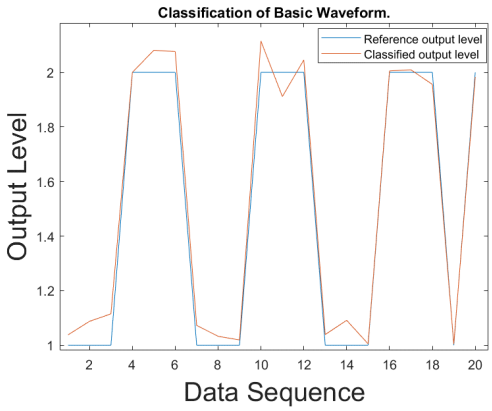

Fig. 5.16: Classification results of the basic waveform task using the parallel diffraction-grating-based optical mask. The blue curve represents the reference output levels for rectangular and triangular waveforms, while the orange curve shows the corresponding classified output levels obtained from the photonic reservoir.

Furthermore, we evaluated the performance of our proposed RC scheme with the MZI-based optical mask by calculating a classification confusion matrix, depicted in Fig. 5.18. From this figure, it is apparent that digits '3', '6', '8', and '9'

exhibit better performance based on the color bar readings. However, the values for spoken digits '5' and '7' are comparatively lower.

For the MZI-based optical mask configuration, the spoken-digit audio signals are first encoded and injected into the photonic reservoir system. The overall experimental setup and system parameters remain the same as those described in the previous section using the diffraction grating mask. In particular, the photonic time-stretch configuration, the feedback loop parameters, and the number of reservoir nodes are kept identical to ensure a fair comparison between different optical masking schemes.

In this system, the input optical signals propagate through the photonic time-stretch module, where chromatic dispersion maps the optical spectrum into the temporal domain. The masked optical signals are then injected into the reservoir with optical feedback, generating complex nonlinear dynamics. The temporal responses of the system are sampled and divided into 400 virtual nodes, which form the reservoir states.

These states are then used as features for the linear readout layer. During the training stage, the output weights are obtained using a linear regression method. The trained output weights corresponding to the reservoir nodes are shown in Fig. 5.17. The distribution of positive and negative weights indicates that different reservoir nodes contribute differently to the spoken-digit classification task.

In the testing stage, the trained model is applied to unseen samples, and the final class label is determined using a winner-takes-all decision strategy. The classification performance is summarized by the confusion matrix shown in Fig. 5.18.

To analyze the distribution of possibilities, we examined the performance for each spoken digit. Additional classification distribution information is provided in Fig. 5.19. From Fig. 5.19, it's evident that spoken digit audios '0', '2', '4', '6', '8', and '9' show more pronounced differences compared to other instances. Conversely, spoken digit audios '5' and '7' exhibit similar distributions to other

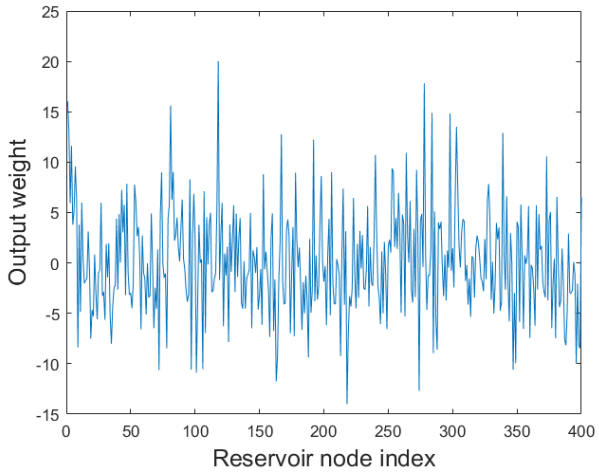

Fig. 5.17: Trained output weights of the 400 reservoir nodes obtained during the spoken-digit classification task using the MZI-based optical mask (shown here for digit "1" as an example).

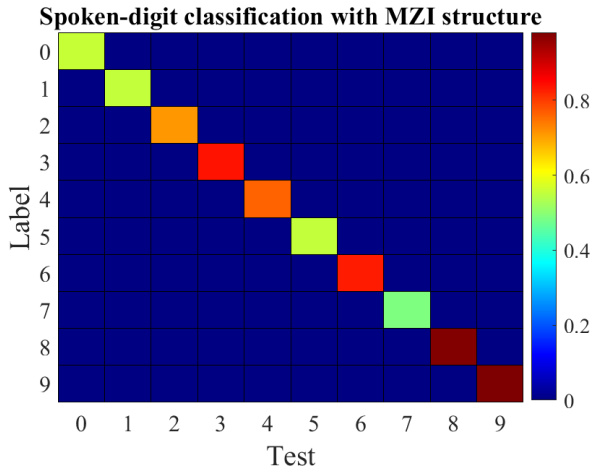

Fig. 5.18: Confusion matrix of spoken-digit classification with MZI structure.

digits, indicating comparatively weaker performance.

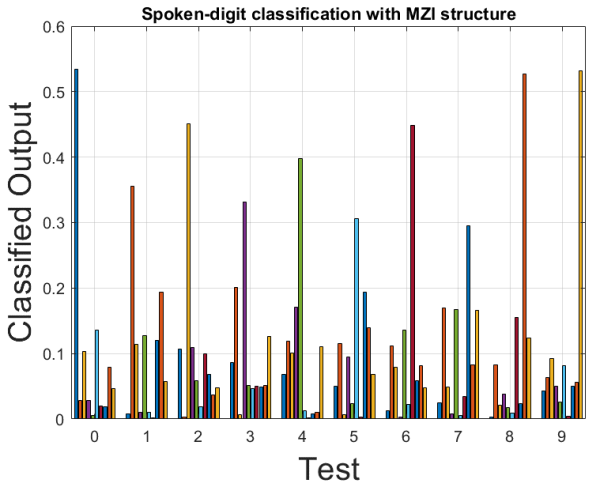

Fig. 5.19: Distribution of the classified spoken-digit audio with MZI structure.

5.4.3 optical mask with a single-mode-multimode-single-mode (SMS) fibre structure.

Previous research has explored methods such as parallel diffraction gratings and Mach-Zehnder Interferometers (MZI) for optically applying the mask. However, these approaches are complex and inefficient. In this section, we propose an optical mask based on the Single Mode-Multi Mode-Single Mode (SMS) fiber configuration. Acting as an optical filter for the Gaussian pulse after photonic time-stretching, this structure offers a simpler, more cost-effective alternative while remaining tunable for adjusting coupling regions. The SMS fiber-based optical mask is seamlessly integrated into the optical link.

The proposed photonic reservoir computing (RC) system, illustrated in Fig. 5.20, leverages time stretching and spectral mixing. Initially, an ultrashort pulse emitted from a mode-locked laser (MLL) is stretched using a dispersion-compensating fiber (DCF). Within the reservoir layer, wavelengths serve as nodes, exploiting the mapping relationship between time and wavelength in photonic

time stretch. Nonlinear coupling of these wavelength nodes is facilitated by a semiconductor optical amplifier (SOA), utilizing Four-Wave Mixing (FWM) for spectral mixing. This process occurs through wavelength conversion within the SOA, where adjacent wavelengths interact and exchange energy, leading to effective spectral mixing.

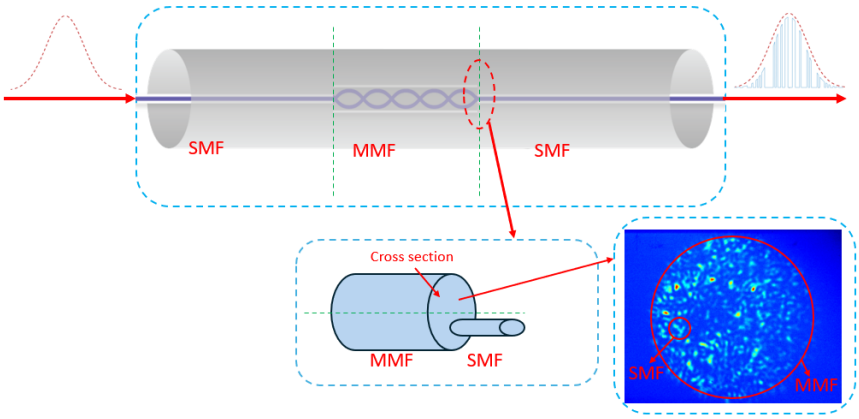

Fig. 5.20: Schematic of the photonic reservoir computer with optical input mask generator using an SMS structure [165].

Optical fiber offers several unique advantages over other transmission media, including compact size, lightweight construction, low transmission loss, and immunity to electromagnetic interference. Since the first low-loss silica optical fiber was proposed in the 1960s and fabricated in the 1970s, fiber optics have seen widespread applications and continuous innovations, particularly in communication and sensing technologies.

A typical optical fiber consists of a high-refractive-index (RI) core surrounded by a lower RI cladding. Among various optical fiber-based structures, the Single Mode-Multimode-Single Mode (SMS) fiber structure incorporates a short section of multimode fiber (MMF) spliced between two single-mode fibers (SMFs). Given its combination of different fiber types, the SMS structure is often referred to as a fiber heterostructure. SMS structures offer key advantages such as ease of fabrication, low cost, flexible design, and high sensitivity—making them highly

useful in real-world sensor development.

As shown in Fig. 5.20, when light is injected from the input SMF into the MMF, multiple modes (including fundamental and higher-order modes) are excited and propagate independently through the MMF section. Multimode interference (MMI) occurs among these modes within the MMF, dictating the transmission spectral response at the output SMF.

Assuming that both the SMF and MMF are circularly symmetric and perfectly aligned, only the LP_{0m} modes can be excited within the MMF when light is injected from the SMF. In both input and output SMFs, only the fundamental mode $E_S(r)$ is supported [166, 167]. When light enters the MMF, the fundamental mode can be decomposed into eigenmodes $\varphi_m(r)$ of the MMF:

$$E_S(r) = \sum_{m=1}^{M} b_m \varphi_m(r) \tag{5-11}$$

where b_m is the excitation coefficient given by:

$$b_m = \frac{\int_0^\infty E_S(r)\varphi_m(r)\, r\, dr}{\int_0^\infty \varphi_m^2(r)\, r\, dr} \tag{5-12}$$

At a distance z in the MMF, the field becomes:

$$E_M(r,z) = \sum_{m=1}^{M} b_m \varphi_m(r) e^{j\beta_m z} \tag{5-13}$$

The transmission power at the output SMF is then calculated via the overlap integral method [168, 169] :

$$P(z) = 10 \cdot \log_{10}\left(\frac{\left|\int_0^\infty E_M(r,z)E_S(r)\, r\, dr\right|^2}{\int_0^\infty |E_M(r,z)|^2 r\, dr \cdot \int_0^\infty |E_S(r)|^2 r\, dr}\right) \tag{5-14}$$

By substituting and using the orthogonality of MMF modes [170, 171]:

$$P(z) = 10 \cdot \log_{10}\left(\left|\sum_{m=1}^{M} b_m^2 e^{j\beta_m z}\right|^2\right) \tag{5-15}$$

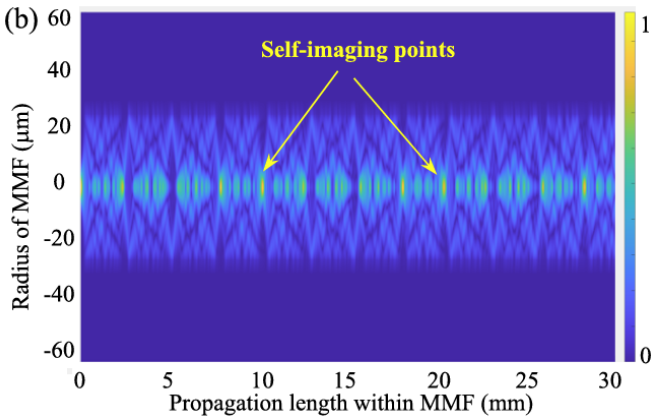

Fig. 5.21: Calculated multimode interference distribution along a 30 mm multimode fiber (MMF). The horizontal axis represents the propagation length, and the vertical axis denotes the radial position within the fiber core. The color scale indicates the normalized optical intensity. Periodic self-imaging points are observed due to coherent interference among guided modes, illustrating the spatial filtering mechanism of the SMS structure.

In this experimental setup, we use the SMS fiber structure as an optical spectral filter for temporal masking. Due to the mapping between wavelength and time domains after photonic time-stretching, spectral shaping translates into temporal masking.

The SMS structure shown in Fig. 5.20 uses a 450 mm MMF with a core diameter of 105 um and NA of 0.22. Only part of the speckle from the MMF is coupled into the second SMF. The output speckle pattern is shown in Fig. 5.23. The speckle patterns were experimentally captured using an infrared camera placed at the output facet of the MMF. The emitted light was collimated by a microscope objective and projected onto the camera sensor for intensity recording. All measurements were performed under stable input power and alignment conditions to ensure repeatability.

To allow tunability, a manual fiber fuser is used to align the SMS structure precisely, minimizing coupling loss. Fig. 5.24 shows the tunable SMS structure setup. Fig. 5.25 presents the captured spectral response.

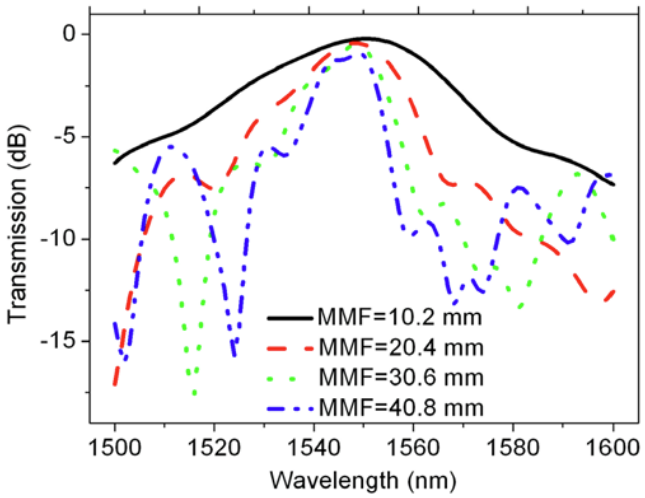

Fig. 5.22: Calculated spectral response of an SMS using Eq. (5-15).

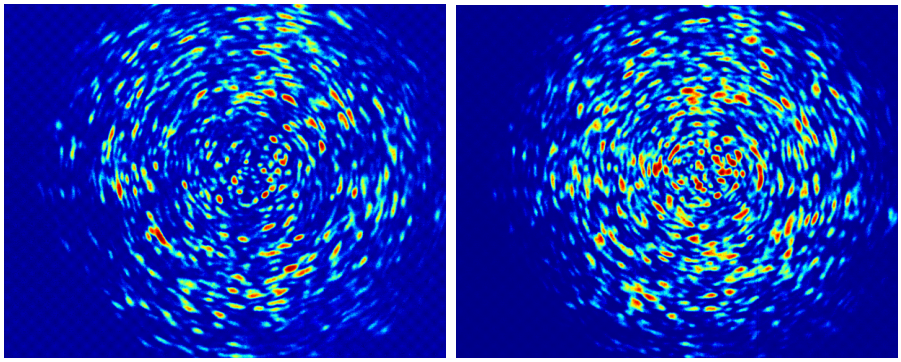

(a) (b)

Fig. 5.23: Experimentally captured speckle patterns at the output facet of the multimode fiber (MMF) using a camera. (a) Speckle distribution under the initial alignment condition. (b) Speckle distribution after slight adjustment of the SMS structure, demonstrating the sensitivity of the multimode interference pattern.

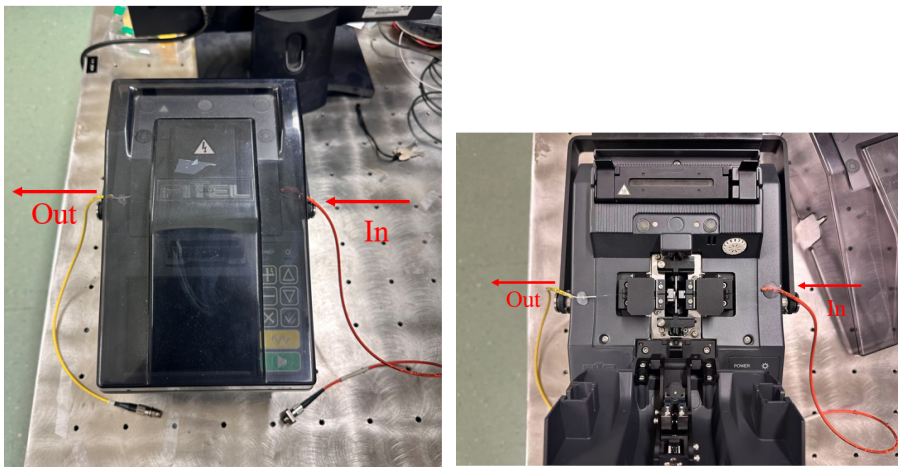

(a) (b)

Fig. 5.24: Experimental implementation of the SMS structure using a fiber fusion splicer operated in manual alignment mode. (a) External view of the fusion splicer with the input (In) and output (Out) fibers connected. (b) Internal view showing the manual alignment stage, where the single-mode fiber (SMF) is intentionally offset relative to the multimode fiber (MMF) output facet to selectively couple a portion of the speckle field into the SMF. This spatially selective coupling enables the SMS structure to function as a wavelength-dependent optical filter.

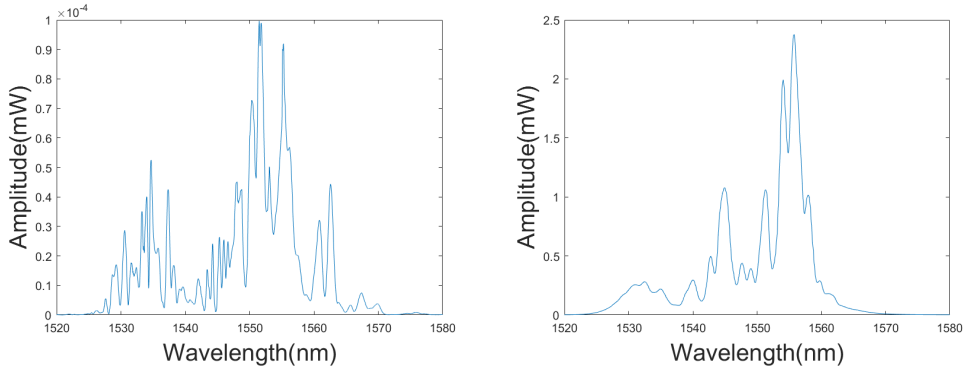

(a) (b)

Fig. 5.25: Measured spectral responses of the SMS-based optical mask for two different coupling positions on the MMF output facet: (a) position 1, (b) position 2. Different spatial sampling leads to different wavelength-dependent filtering profiles.

To assess system performance, we carried out isolated spoken-digit recognition using a standard dataset. The overall experimental setup and system parameters remain the same as those described in the previous sections, including the photonic time-stretch configuration, feedback loop parameters, and the number of reservoir nodes.

The RC system includes 400 virtual nodes generated through time-multiplexing of the stretched optical pulses. After the photonic time-stretch stage, an SMS-based optical mask is introduced to modulate the temporal waveform before it enters the reservoir. This masking process expands the input signal into a higher-dimensional state space, enabling effective reservoir processing, as illustrated in Fig. 5.26

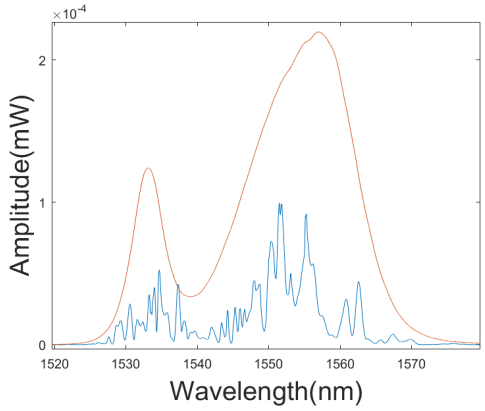

Fig. 5.26: Measured spectral response illustrating the effect of the added optical mask. The red curve represents the original input optical spectrum before masking, while the blue curve shows the wavelength-dependent filtering profile introduced by the SMS-based optical mask. The resulting modulated spectrum demonstrates how spatially selective multimode interference reshapes the spectral distribution in the wavelength domain.

The resulting reservoir responses are collected as reservoir states and used as features for the readout layer. During the training stage, the output weights are obtained using a linear regression method. The trained output weights corresponding to the reservoir nodes are shown in Fig. 5.27. The distribution of positive and negative weights indicates that different reservoir nodes contribute

differently to the spoken-digit classification task.

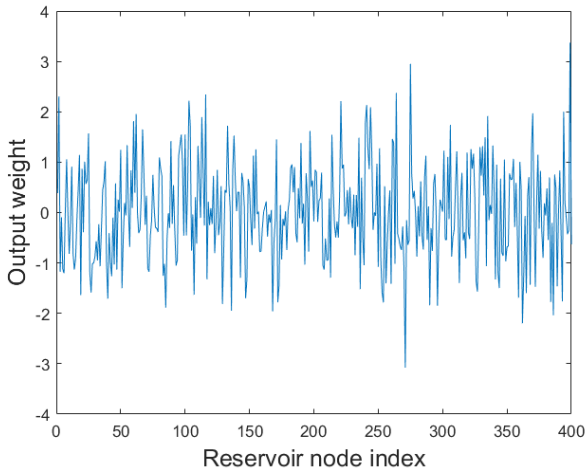

Fig. 5.27: Trained output weights of the 400 reservoir nodes obtained during the spoken-digit classification task using the SMS-based optical mask (shown here for digit "1" as an example).

In the testing stage, the trained model is applied to unseen samples, and the final class label is determined using a winner-takes-all decision strategy. The classification performance is summarized by the confusion matrix shown in Fig. 5.28.

We further analyzed recognition distribution per digit. The result is shown in Fig. 5.29. Digits '1', '4', '5', and '7' performed best, while '2' and '9' showed lower accuracy. The SMS-based mask improved accuracy to 99.97%, compared to 80.65% without the mask.

5.5 Classification Performance of Photonic Reservoir Computing with Different Optical Mask Schemes

In the previous section, we presented the experimental results and corresponding classification accuracy. To assess the impact of the Time-Delay Reservoir

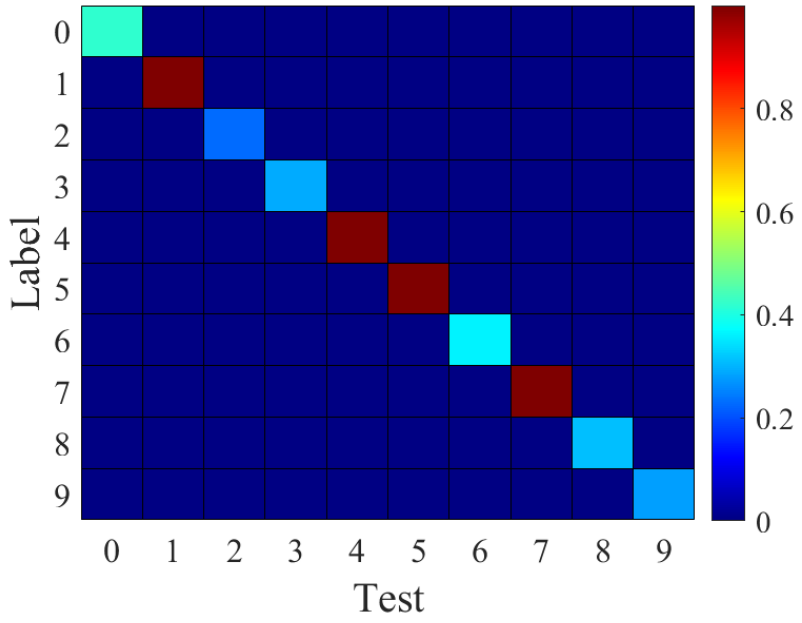

Fig. 5.28: Confusion matrix of spoken-digit classification with SMS fiber structure.

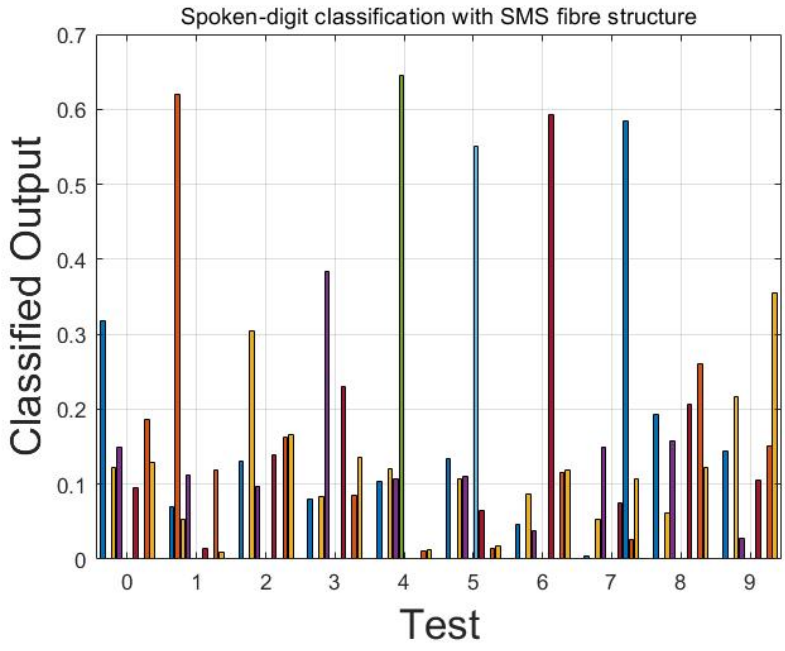

Fig. 5.29: Distribution of the classified spoken-digit audio with SMS fiber structure.

Computing (TDRC) system with different optical masks, we conducted waveform classification and spoken-digit classification as benchmark tests. The Normalized Mean Square Errors (NMSEs) for different optical input masks were calculated as follows: Parallel diffraction gratings: 0.59619; MZI-based optical mask: 0.4613.

The photonic RC system with an optical mask demonstrates superior performance, leading to improved classification accuracy. Without the optical mask, the classification accuracy is 80.65%. By introducing an optical mask, the accuracy increases to 97.19% with the MZI-based mask and 98.16% with the parallel diffraction grating mask.

To further quantify the effectiveness of spoken-digit classification using our proposed photonic RC with an optical mask, we evaluated and compared classification accuracy. Table 1 summarizes the results: MZI-based optical mask: 97.19% accuracy; Diffraction gratings mask: 98.16% accuracy; No optical mask: 80.65% accuracy. These results confirm that incorporating an optical input mask significantly enhances classification performance compared to the unmasked system.

The classification accuracy is calculated based on the final decision obtained using a winner-takes-all strategy. For each test sample, the output neuron with the maximum value is selected as the predicted class label. The classification accuracy is then defined as the ratio of correctly classified samples to the total number of test samples.

The NMSE is calculated using the difference between the reservoir output and the corresponding target output. It measures how closely the predicted output matches the expected output in a continuous sense. Therefore, NMSE and classification accuracy evaluate the system from two different perspectives: the former reflects the regression error between the predicted and target outputs, while the latter reflects the final classification correctness after decision making.

In general, a lower NMSE tends to correspond to a higher classification accuracy, because smaller output errors usually lead to more reliable class decisions.

However, the relationship is not strictly one-to-one, since the final classification accuracy depends on the winner-takes-all decision rule, whereas NMSE depends on the numerical difference between predicted and target values.

Table 1: Classification accuracy with different optical masks in the photonic RC system.

Optical Mask	**Classification Accuracy**
Optical Mask using Parallel Diffraction Gratings	98.16%
Optical Mask using MZI[a] Structure	97.19%
Optical Mask using SMS Structure	99.97%
Photonic RC System without Mask	80.65%

[a] MZI: Mach-Zehnder Interferometer.

5.6 Summary

In this chapter, we propose an all-optical reservoir computing (RC) scheme featuring an optical input mask, which is applied to the optical link before modulation. This approach circumvents electronic limitations, offering faster computation speeds and reducing the dependency on high-speed electronic components compared to digital masks.

We introduce three optical masking schemes: parallel diffraction gratings, MZI structure, and SMS fiber structure. Through experimental demonstrations, we successfully integrate these optical masks into the optical domain and evaluate their effectiveness in waveform classification and spoken-digit classification tasks. The results confirm that RC systems with optical masks outperform their digital counterparts, achieving high classification accuracy while addressing electronic bottlenecks. This innovation enables real-time classification using optical reservoir computing.

Additionally, we experimentally demonstrate a novel photonic reservoir computing system incorporating an SMS (Single Mode-Multimode-Single Mode) fiber-based optical mask, which shows promising results in spoken-digit recognition.

Furthermore, we investigate the relationship between different optical masks and classification performance in optical reservoir computing, comparing uniform, non-uniform, and linear chirp masks. Results indicate that a richer reservoir state leads to improved classification accuracy, reinforcing the significance of optical mask selection in enhancing system performance.

Chapter 6

CONCLUSION AND FUTURE WORK

6.1 Conclusions

High-throughput detection holds significant potential across various fields due to its ability to leverage the intrinsic high-speed characteristics of light. This capability enables exceptionally rapid data processing. When integrated with advanced techniques such as artificial intelligence (AI) or spike-inspired algorithms, high-throughput detection becomes an increasingly attractive and versatile tool for research and application development.

In summary, the main conclusions of this thesis are as follows:

• This thesis presents a groundbreaking indoor user localization system leveraging photonic time stretch and reservoir computing (RC), detailed in Chapter 3. A novel RC-assisted method for ultrafast user localization in beam-steering optical wireless systems (OWC) is introduced. The photonic time stretch of ultrashort optical pulses enables ultrafast, wavelength-controlled beam steering, achieving instantaneous optical wavelength detection within the sub-nanosecond range through chirped optical spectral coding and RC-based microwave frequency

identification. Our results demonstrate that RC is a more efficient and robust approach to ultrafast signal identification compared to conventional methods. The proposed system achieves real-time ultrafast user localization at a 50 MHz rate, using wavelength-encoded signals and a passive beam scanner with a 45° tilted fiber grating (TFG). This approach not only determines angular separation but also simultaneously calculates the linear distance from the access point. Importantly, the challenging task of instantaneous optical wavelength identification within nanoseconds is successfully accomplished through chirped microwave frequency encoding and RC-based frequency identification. A proof-of-concept experiment validates the system, showing superior performance of RC in frequency chirp identification compared to the conventional short-time Fourier transform method. This innovative method marks a significant advancement in optically controlled beam-steering wireless communication systems.

- Building on previous research into photonic time stretch (PTS) and reservoir computing (RC), this work addresses the challenges posed by the large datasets generated due to the characteristics of PTS. Specifically, the collected data comprises extensive serial time-domain information, which requires time-consuming processing on a host computer. To overcome this limitation, a novel method combining RC and PTS is proposed to enhance processing speed. The new approach integrates photonic time stretch with spectrum mixing. In the reservoir layer, wavelengths are selected as reservoir nodes, and nonlinearity is introduced via a semiconductor optical amplifier (SOA). The system's performance is evaluated using tasks such as basic waveform identification and frequency classification. Results demonstrate the ability of the system to distinguish between tasks effectively. Simulations conducted using VPI Photonics were employed to further optimize the system's performance. Key parameters, including optical feedback strength, SOA drive current, the number of nodes, and the number of masks, were adjusted to improve classification and identification accuracy. These simulations

revealed optimal configurations that significantly enhance system performance. Subsequently, a proof-of-concept experiment was carried out to validate the simulation results. The experimental findings confirm the feasibility of the proposed photonic RC scheme and exhibit strong consistency with the simulation results. This demonstrates the potential of the system for practical applications, achieving improved processing speed and

- This work introduces a novel method of incorporating an optical mask before the reservoir layer to enhance system performance. By adding the mask prior to sending the signal to the reservoir layer, the approach imposes certain requirements on the arbitrary waveform generator. To further accelerate processing, a new optical mask scheme is proposed, featuring three specific configurations: Parallel Diffraction Gratings, Mach-Zehnder Interferometer (MZI) Structure Mask, and Single Mode-Multimode-Single Mode (SMS) Structure Configuration. The performance of these optical masks was evaluated using a spoken-digit classification task. Results demonstrate that systems with optical masks significantly outperform both systems without masks and those employing digital masks. This highlights the superior efficacy of optical masking in enhancing system accuracy and efficiency.

6.2 Future Work

Future work should prioritize the development and enhancement of processing speed, aligning with the growing focus on high-throughput detection and classification in research. Building upon the existing work, efforts should concentrate on further improving the performance of photonic time stretch (PTS)-based photonic reservoir computing systems. This includes optimizing system architecture, refining key parameters, and exploring innovative approaches to achieve faster and more accurate detection and classification. These advancements will help unlock

the full potential of PTS-based systems for real-time, high-throughput applications.

The potential research direction may have three catalogues, they are as follows:

- The first research direction should focus on developing a real-time signal processor utilizing photonic reservoir computing. This involves designing systems capable of processing signals in real time with enhanced speed and accuracy, leveraging the unique advantages of photonic reservoir computing, such as high bandwidth, parallelism, and energy efficiency. Exploring this direction can pave the way for advanced applications in high-speed communication, real-time monitoring, and ultrafast data analysis.
- The second research direction should focus on developing system-on-chip solutions, also known as integrated photonic circuits. These integrated systems, characterized by their compact size, offer significant advantages in improving processing efficiency and speed. Advancements in this area would enable the miniaturization of photonic reservoir computing systems, facilitating their deployment in applications requiring high performance, scalability, and portability.
- Another promising research direction involves expanding applications in autonomous driving and AI systems in vehicles, particularly focusing on LiDAR technology. LiDAR plays a critical role in improving speed and measurement accuracy in automotive systems, and its integration has gained significant attention in recent research. Photonics reservoir computing (RC) offers advantages in one-dimensional signal processing, enabling real-time identification. Preliminary explorations into using RC for processing LiDAR signals have shown promising results. However, current implementations face limitations in accuracy and are restricted to processing discrete detected signals rather than continuous time-series data. To overcome these challenges, future work should focus on developing high-resolution methods to test and identify LiDAR signals more effectively. Advancements in this area could significantly enhance the performance of LiDAR

systems in autonomous vehicles, contributing to safer and more efficient AI-driven transportation solutions.

- For high-throughput detection, in addition to the previously mentioned applications, reservoir computing can be extended to spatial information processing for biomedical diagnostics and moving target recognition. A label-free approach can be employed to identify abnormal cells—such as cancer cells—by detecting the shape and position of targets as primary distinguishing features. To enrich the system's dynamic response to spatial information, a spatial mask concept can be introduced. To further enhance spatial information processing, two distinct patterns were applied to the optical link before the target: a Bar Code Pattern and a QR Code Pattern. The QR Code Pattern, in particular, provides richer spatial information compared to the Bar Code Pattern. For medical cell classification, a microfluidic channel or other application-specific designs can be utilized to ensure precise control and detection.

Bibliography

[1] A. M. Kaushik, K. Hsieh, and T. H. Wang, "Droplet microfluidics for high-sensitivity and high-throughput detection and screening of disease biomarkers," Wiley Interdiscip. Rev. Nanomed. Nanobiotechnol. 10, e1522 (2018).

[2] S. Xu, C. Yang, X. Yan, and H. Liu, "Towards high throughput and high information coverage: advanced single-cell mass spectrometric techniques," Anal. Bioanal. Chem. 414, 1–15 (2022).

[3] X. Xu, X. Zhou, J. Huang, Y. Liu, and Z. Zhang, "High-throughput multi-target molecular detection in an automatic light-addressable photoelectrochemical sensing platform," Anal. Chem. 96, 9185–9191 (2024).

[4] R. Miyan, X. Wang, J. Zhou, Y. Zeng, J. Qu, H. P. Ho, and Y. Shao, "Phase interrogation surface plasmon resonance hyperspectral imaging sensor for multi-channel high-throughput detection," Opt. Express 29, 31418–31425 (2021).

[5] N. Hao, Y. Zuo, Z. Dai, M. Xiong, J. Wei, J. Qian, and K. Wang, "High-throughput detection of multiple contaminants based on portable photoelectrochromic sensor chip," Anal. Chem. 93, 14053–14058 (2021).

[6] S. Gao, Q. Li, S. Zhang, X. Sun, X. Zheng, H. Qian, and J. Wu, "One-step high-throughput detection of low-abundance biomarker BDNF using

a biolayer interferometry-based 3D aptasensor," Biosens. Bioelectron. 215, 114566 (2022).

[7] S. Jiang, C. Guo, P. Song, N. Zhou, Z. Bian, J. Zhu, and G. Zheng, "Resolution-enhanced parallel coded ptychography for high-throughput optical imaging," ACS Photonics 8, 3261–3271 (2021).

[8] K. R. Barter, H. Paradis, R. L. Gendron, J. A. L. Vidal, and O. Meruvia-Pastor, "Novel segmentation algorithm for high-throughput analysis of spectral domain-optical coherence tomography imaging of teleost retinas," Mol. Vis. 28, 492 (2022).

[9] J. Zhou, J. Dong, H. Hou, L. Huang, and J. Li, "High-throughput microfluidic systems accelerated by artificial intelligence for biomedical applications," Lab Chip 24, 1307–1326 (2024).

[10] G. G. D. Suminda, S. Bhandari, Y. Won, U. Goutam, K. K. Pulicherla, Y. O. Son, and M. Ghosh, "High-throughput sequencing technologies in the detection of livestock pathogens, diagnosis, and zoonotic surveillance," Comput. Struct. Biotechnol. J. 20, 5378–5392 (2022).

[11] C. Cai, R. Jin, J. Nie, J. Kang, Y. Zhang, and J. Luo, "Reliable high throughput aerial acoustic communication for mobile network," IEEE Trans. Veh. Technol. 73, 5704–5716 (2023).

[12] M. Bain, J. L. Godínez Castellanos, and S. E. Bradforth, "High-throughput screening for ultrafast photochemical reaction discovery," J. Phys. Chem. Lett. 14, 9864–9871 (2023).

[13] Anatol Khilo. *Integrated Photonic Analog-to-Digital Converters*. PhD thesis, Massachusetts Institute of Technology, 2011.

[14] R. Dastres and M. Soori, "A review in advanced digital signal processing systems," Int. J. Electr. Comput. Eng. 11, (2021).

[15] J. Li, S. Fu, X. Xie, M. Xiang, Y. Dai, F. Yin, and Y. Qin, "Low-latency short-time Fourier transform of microwave photonics processing," J. Light. Technol. 41, 6149–6156 (2023).

[16] J. M. Jordán, J. Abella, and F. J. Cazorla. Homogeneous and heterogeneous mpsoc architectures for embedded systems. *International Journal of Distributed Sensor Networks*, 2012:1–14, 2012.

[17] G. Wang, Y. Zhou, R. Min, E. Du, and C. Wang, "Principle and recent development in photonic time-stretch imaging," Photonics 10, 817 (2023).

[18] Y. Zhang, R. Jin, D. Peng, W. Lyu, Z. Fu, Z. Zhang, and Y. Liu, "Broadband transient waveform digitizer based on photonic time stretch," J. Light. Technol. 39, 2880–2887 (2021).

[19] R. Li, Y. Weng, S. Wei, S. Lin, J. Huang, C. Song, and C. Lei, "Fourier-domain-compressed optical time-stretch quantitative phase imaging flow cytometry," Photon. Res. 12, 1627–1639 (2024).

[20] K. Hashimoto, T. Nakamura, T. Kageyama, V. R. Badarla, H. Shimada, R. Horisaki, and T. Ideguchi, "Upconversion time-stretch infrared spectroscopy," Light Sci. Appl. 12, 48 (2023).

[21] R. Li, Y. Weng, S. Lin, C. Wei, L. Mei, S. Wei, and C. Lei, "All-optical Fourier-domain-compressed time-stretch imaging with low-pass filtering," ACS Photonics 10, 2399–2406 (2023).

[22] B. Yang, Q. Xu, S. Yang, and H. Chi, "Wideband sparse signal acquisition with ultrahigh sampling compression ratio based on continuous-time

photonic time stretch and photonic compressive sampling," Appl. Opt. 61, 1344–1348 (2022).

[23] T. Jiang, L. Wang, and J. Li, "High-resolution timing jitter measurement based on the photonics time stretch technique," Opt. Express 31, 6722–6729 (2023).

[24] G. Wang, Y. Zhou, R. Min, E. Du, and C. Wang, "Principle and recent development in photonic time-stretch imaging," Photonics 10, 817 (2023).

[25] K. Sharifani and M. Amini, "Machine learning and deep learning: A review of methods and applications," World Inf. Technol. Eng. J. 10, 3897–3904 (2023).

[26] H. Niu, H. Li, J. Wang, X. Xu, and H. Ji, "Enhancing computer digital signal processing through the utilization of RNN sequence algorithms," Int. J. Comput. Sci. Inf. Technol. 1, 60–68 (2023).

[27] P. Ray, S. S. Reddy, and T. Banerjee, "Various dimension reduction techniques for high dimensional data analysis: a review," Artif. Intell. Rev. 54, 3473–3515 (2021).

[28] P. B. Weerakody, K. W. Wong, G. Wang, and W. Ela, "A review of irregular time series data handling with gated recurrent neural networks," Neurocomputing 441, 161–178 (2021).

[29] J. Zhu, Q. Jiang, Y. Shen, C. Qian, F. Xu, and Q. Zhu, "Application of recurrent neural network to mechanical fault diagnosis: A review," J. Mech. Sci. Technol. 36, 527–542 (2022).

[30] A. Orvieto, S. L. Smith, A. Gu, A. Fernando, C. Gulcehre, R. Pascanu, and S. De, "Resurrecting recurrent neural networks for long sequences," in Proc. Int. Conf. Mach. Learn., 26670–26698 (2023).

[31] K. Nakajima and I. Fischer, Reservoir Computing (Springer, Singapore, 2021).

[32] D. J. Gauthier, E. Bollt, A. Griffith, and W. A. Barbosa, "Next generation reservoir computing," Nat. Commun. 12, 1–8 (2021).

[33] H. Dai and Y. K. Chembo, "Classification of IQ-modulated signals based on reservoir computing with narrowband optoelectronic oscillators," IEEE J. Quantum Electron. 57, 1–8 (2021).

[34] Masaya Nakajima, Koji Tanaka, and Takashi Hashimoto. Scalable reservoir computing on coherent linear photonic processor. *Communications Physics*, 4(1):20, 2021.

[35] T. Kamiya and M. Tsuchiya, "Progress in ultrafast photonics," Jpn. J. Appl. Phys. 44, 5875 (2005).

[36] Y. Zhang, C. Tao, S. Luo, K. Y. Lau, J. Zheng, L. Huang, and Z. Sun, "Ultra-fast optical time-domain transformation techniques," Nat. Rev. Methods Primers 5, 11 (2025).

[37] Y. Zhang, C. Tao, S. Luo, K. Y. Lau, J. Zheng, L. Huang, and Z. Sun, "Ultra-fast optical time-domain transformation techniques," Nat. Rev. Methods Primers 5, 11 (2025).

[38] G. Genty, L. Salmela, J. M. Dudley, D. Brunner, A. Kokhanovskiy, S. Kobtsev, and S. K. Turitsyn, "Machine learning and applications in ultrafast photonics," Nat. Photonics 15, 91–101 (2021).

[39] M. Mohammadi, F. Habibi, M. Seifouri, and S. Olyaee, "Recent advances on all-optical photonic crystal analog-to-digital converter (ADC)," Opt. Quantum Electron. 54, 192 (2022).

[40] X. Li, J. Li, Y. Li, A. Ozcan, and M. Jarrahi, "High-throughput terahertz imaging: progress and challenges," Light Sci. Appl. 12, 233 (2023).

[41] F. Coppinger, A. S. Bhushan, and B. Jalali, "Photonic time stretch and its application to analog-to-digital conversion," IEEE Trans. Microw. Theory Techn. 47, 1309–1314 (1999).

[42] A. Mahjoubfar, D. V. Churkin, S. Barland, N. Broderick, S. K. Turitsyn, and B. Jalali, "Time stretch and its applications," Nat. Photonics 11, 341–351 (2017).

[43] C. Deakin, Dual Optical Frequency Comb Analog to Digital Conversion (Ph.D. dissertation, Univ. Coll. London, 2022).

[44] K. Sozański, "Overview of signal processing problems in power electronic control circuits," Energies 16, 4774 (2023).

[45] J. Jansson and W. Nordgren, "Analog mixed signal front-end for torque signal processing: A theoretical noise analysis and signal-chain evaluation," (2023).

[46] C. Toninelli, I. Gerhardt, A. S. Clark, A. Reserbat-Plantey, S. Götzinger, Z. Ristanović, and M. A. J. G. Orrit, "Single organic molecules for photonic quantum technologies," Nat. Mater. 20, 1615–1628 (2021).

[47] T. T. Wong, A. K. Lau, K. K. Wong, and K. K. Tsia, "Optical time-stretch confocal microscopy at 1 μm," Opt. Lett. 37, 3330–3332 (2012).

[48] B. T. Bosworth, et al., "High-speed flow microscopy using compressed sensing with ultrafast laser pulses," Opt. Express 23, 10521–10532 (2015).

[49] C. Rullière, Femtosecond Laser Pulses: Principles and Experiments (Springer, Berlin Heidelberg, 2013).

[50] A. M. Weiner, "Femtosecond pulse shaping using spatial light modulators," Rev. Sci. Instrum. 71, 1929–1960 (2000).

[51] C. Wang, "Dispersive Fourier transformation for versatile microwave photonics applications," Photonics 1, 586–612 (2014).

[52] B. H. Kolner, "Space-time duality and the theory of temporal imaging," IEEE J. Quantum Electron. 30, 1951–1963 (1994).

[53] A. Papoulis, "Pulse compression, fiber communications, and diffraction: A unified approach," J. Opt. Soc. Am. A 11, 3–13 (1994).

[54] M. A. Muriel, J. Azana, and A. Carballar, "Real-time Fourier transformer based on fiber gratings," Opt. Lett. 24, 1–3 (1999).

[55] H. Y. Xia and J. P. Yao, "Characterization of subpicosecond pulses based on temporal interferometry with real-time tracking of higher order dispersion and optical time delay," J. Light. Technol. 27, 5029–5037 (2009).

[56] S. Gupta and B. Jalali, "Time-warp correction and calibration in photonic time-stretch analog-to-digital converter," Opt. Lett. 33, 2674–2676 (2008).

[57] H. Y. Xia, C. Wang, S. Blais, and J. P. Yao, "Ultrafast and precise interrogation of fiber Bragg grating sensor based on wavelength-to-time mapping incorporating higher order dispersion," J. Light. Technol. 28, 254–261 (2010).

[58] G. Wang, Y. Zhou, R. Min, E. Du, and C. Wang, "Principle and recent development in photonic time-stretch imaging," Photonics 10, 817 (2023).

[59] T. Zhou, Y. Goto, T. Makino, C. MacPhee, Y. Zhou, A. M. Madni, and B. Jalali, "Time stretch with continuous-wave lasers," APL Photonics 9, 086101 (2024).

[60] S. Jooken, K. Zinoviev, G. Yurtsever, A. De Proft, K. de Wijs, Z. Jafari, and N. Verellen, "On-chip flow cytometer using integrated photonics for the detection of human leukocytes," Sci. Rep. 14, 10921 (2024).

[61] S. Chen, R. Hao, Y. Zhang, and H. Yang, "Optofluidics in bio-imaging applications," Photon. Res. 7, 532–542 (2019).

[62] R. Li, Y. Weng, S. Lin, C. Wei, L. Mei, S. Wei, and C. Lei, "All-optical Fourier-domain-compressed time-stretch imaging with low-pass filtering," ACS Photonics 10, 2399–2406 (2023).

[63] Y. Jiang, S. Karpf, and B. Jalali, "Time-stretch LiDAR as a spectrally scanned time-of-flight ranging camera," Nat. Photonics 14, 14–18 (2020).

[64] C. K. Mididoddi, F. Bai, G. Wang, J. Liu, S. Gibson, and C. Wang, "High-throughput photonic time-stretch optical coherence tomography with data compression," IEEE Photon. J. 9, 1–15 (2017).

[65] W. Liao, Y. Yue, S. Liu, C. Wang, and A. Zhang, "High-speed multi-channel signal acquisition in photonic time stretch optical coherence tomography through frequency division multiplexing," in Proc. Int. Topical Meet. Microw. Photon. (MWP), 1–3 (2024).

[66] A. H. Tang, P. Yeung, G. C. Chan, B. P. Chan, K. K. Wong, and K. K. Tsia, "Time-stretch microscopy on a DVD for high-throughput imaging cell-based assay," Biomed. Opt. Express 8, 640–652 (2017).

[67] R. Verma, V. Nagar, and S. Mahapatra, "Introduction to supervised learning," in Data Analytics in Bioinformatics: A Machine Learning Perspective, 1–34 (2021).

[68] D. Dwibedi, Y. Aytar, J. Tompson, P. Sermanet, and A. Zisserman, "With a little help from my friends: Nearest-neighbor contrastive learning of visual

representations," in Proc. IEEE/CVF Int. Conf. Comput. Vis., 9588–9597 (2021).

[69] Q. Ren, H. Zhang, D. Zhang, X. Zhao, L. Yan, J. Rui, and X. Zhu, "A framework of active learning and semi-supervised learning for lithology identification based on improved naive Bayes," Expert Syst. Appl. 202, 117278 (2022).

[70] A. Glielmo, B. E. Husic, A. Rodriguez, C. Clementi, F. Noé, and A. Laio, "Unsupervised learning methods for molecular simulation data," Chem. Rev. 121, 9722–9758 (2021).

[71] P. E. Jebarani, N. Umadevi, H. Dang, and M. Pomplun, "A novel hybrid K-means and GMM machine learning model for breast cancer detection," IEEE Access 9, 146153–146162 (2021).

[72] M. Sudharsan and G. Thailambal, "Alzheimer's disease prediction using machine learning techniques and principal component analysis (PCA)," Mater. Today Proc. 81, 182–190 (2023).

[73] O. F. Althuwaynee, A. Aydda, I. T. Hwang, Y. K. Lee, S. W. Kim, H. J. Park, and Y. Park, "Uncertainty reduction of unlabeled features in landslide inventory using machine learning t-SNE clustering and data mining apriori association rule algorithms," Appl. Sci. 11, 556 (2021).

[74] Y. Matsuo, Y. LeCun, M. Sahani, D. Precup, D. Silver, M. Sugiyama, and J. Morimoto, "Deep learning, reinforcement learning, and world models," Neural Netw. 152, 267–275 (2022).

[75] B. Singh, R. Kumar, and V. P. Singh, "Reinforcement learning in robotic applications: a comprehensive survey," Artif. Intell. Rev. 55, 945–990 (2022).

[76] M. Hu, "Temporal difference learning," in The Art of Reinforcement Learning: Fundamentals, Mathematics, and Implementations with Python (Apress, Berkeley, CA, 2023), pp. 75–107.

[77] I. Ilahi, M. Usama, J. Qadir, M. U. Janjua, A. Al-Fuqaha, D. T. Hoang, and D. Niyato, "Challenges and countermeasures for adversarial attacks on deep reinforcement learning," IEEE Trans. Artif. Intell. 3, 90–109 (2021).

[78] F. Shao and Z. Shen, "How can artificial neural networks approximate the brain?" Front. Psychol. 13, 970214 (2023).

[79] V. Dogra, S. Verma, Kavita, P. Chatterjee, J. Shafi, J. Choi, and M. F. Ijaz, "A complete process of text classification system using state-of-the-art NLP models," Comput. Intell. Neurosci. 2022, 1883698 (2022).

[80] N. Nehra, P. Sangwan, and D. Kumar, "Artificial neural networks: a comprehensive review," in Handbook of Machine Learning for Computational Optimization, 203–227 (2021).

[81] O. Barabash, A. Makarchuk, P. Open'ko, and S. Korotin. Application of svm, ffnns, k-nn and their ensembles for identifying functionally reliable systems. *Axioms*, 14(4):237, 2025.

[82] J. Wang, X. Li, J. Li, Q. Sun, and H. Wang, "NGCU: A new RNN model for time-series data prediction," Big Data Res. 27, 100296 (2022).

[83] A. Tsantekidis, N. Passalis, and A. Tefas, "Recurrent neural networks," in Deep Learning for Robot Perception and Cognition (Academic Press, 2022), pp. 101–115.

[84] Gonzalo Nápoles, Aleksandra Jastrzebska, Ivan Grau, and Yailé Salgueiro. Backpropagation through time learning for recurrence-aware long-term cognitive networks. *Knowledge-Based Systems*, 295:111825, 2024.

[85] H. Zhang and D. V. Vargas, "A survey on reservoir computing and its interdisciplinary applications beyond traditional machine learning," IEEE Access 11, 81033–81070 (2023).

[86] E. L. Bolager, A. Cukarska, I. Burak, Z. Monfared, and F. Dietrich, "Gradient-free training of recurrent neural networks," arXiv preprint arXiv:2410.23467 (2024).

[87] H. Jaeger, "The 'echo state' approach to analysing and training recurrent neural networks—with an erratum note," GMD Tech. Rep. 148, 13 (2001).

[88] W. Maass, T. Natschläger, and H. Markram, "Real-time computing without stable states: A new framework for neural computation based on perturbations," Neural Comput. 14, 2531–2560 (2002).

[89] M. Lukoševičius, "A practical guide to applying echo state networks," in Neural Networks: Tricks of the Trade, Second Edition (Springer, Berlin Heidelberg, 2012), pp. 659–686.

[90] D. Verstraeten, B. Schrauwen, M. D'Haene, and D. Stroobandt, "An experimental unification of reservoir computing methods," Neural Netw. 20, 391–403 (2007).

[91] L. Büsing, B. Schrauwen, and R. Legenstein, "Connectivity, dynamics, and memory in reservoir computing with binary and analog neurons," Neural Comput. 22, 1272–1311 (2010).

[92] I. S. Gradshteyn and I. M. Ryzhik, Tables of Integrals, Series, and Products, 6th ed. (Academic Press, San Diego, CA, 2000).

[93] M. Lukosevicius, D. Popovici, H. Jaeger, and U. Siewert, "Time warping invariant echo state networks," Tech. Rep. No. 2, Jacobs Univ. Bremen (2006).

[94] H. Jaeger, M. Lukosevicius, D. Popovici, and U. Siewert, "Optimization and applications of echo state networks with leaky-integrator neurons," Neural Netw. 20, 335–352 (2007).

[95] G. Holzmann and H. Hauser, "Echo state networks with filter neurons and a delay and sum readout," Neural Netw. 23, 244–256 (2010).

[96] T. Y. Zheng, W. H. Yang, J. Sun, X. Y. Xiong, Z. T. Li, and X. D. Zou, "Parameters optimization method for the time-delayed reservoir computing with a nonlinear Duffing mechanical oscillator," Sci. Rep. 11, 997 (2021).

[97] C. Meffan, T. Ijima, A. Banerjee, J. Hirotani, and T. Tsuchiya, "Non-linear processing with a surface acoustic wave reservoir computer," Microsyst. Technol. 29, 1197–1206 (2023).

[98] X. Liang, J. Tang, Y. Zhong, B. Gao, H. Qian, and H. Wu, "Physical reservoir computing with emerging electronics," Nat. Electron. 7, 193–206 (2024).

[99] Y. W. Shen, R. Q. Li, G. T. Liu, J. Yu, X. He, L. Yi, and C. Wang, "Deep photonic reservoir computing recurrent network," Optica 10, 1745–1751 (2023).

[100] J. Degrave, K. Caluwaerts, J. Dambre, and F. Wyffels, "Developing an embodied gait on a compliant quadrupedal robot," in Proc. IEEE/RSJ Int. Conf. Intell. Robots Syst. (IROS), 4486–4491 (2015).

[101] G. Dion, S. Mejaouri, and J. Sylvestre, "Reservoir computing with a single delay-coupled non-linear mechanical oscillator," J. Appl. Phys. 124, 154901 (2018).

[102] M. F. F. Chowdhury, W. A. Misba, M. M. Rajib, A. J. Edwards, D. Bhattacharya, M. S. Varghese, and J. Atulasimha, "Focused surface acoustic

wave induced nano-oscillator based reservoir computing," Appl. Phys. Lett. 121, 104101 (2022).

[103] T. Ijima, C. Meffan, M. Shimofuri, A. Banerjee, J. Hirotani, and T. Tsuchiya, "Nonlinear thermo-acoustic phase modulator for physical reservoir computing," Jpn. J. Appl. Phys. 64, 03SP33 (2025).

[104] M. L. Alomar, M. C. Soriano, M. Escalona-Morán, V. Canals, I. Fischer, C. R. Mirasso, and J. L. Rosselló, "Digital implementation of a single dynamical node reservoir computer," IEEE Trans. Circuits Syst. II 62, 977–981 (2015).

[105] J. Torrejon, M. Riou, F. A. Araujo, S. Tsunegi, G. Khalsa, D. Querlioz, and J. Grollier, "Neuromorphic computing with nanoscale spintronic oscillators," Nature 547, 428–431 (2017).

[106] Y. Zhong, J. Tang, X. Li, X. Liang, Z. Liu, Y. Li, and H. Wu, "A memristor-based analogue reservoir computing system for real-time and power-efficient signal processing," Nat. Electron. 5, 672–681 (2022).

[107] A. Katumba, Energy-Efficient Photonic Neuromorphic Computing for Telecommunication Applications (Ph.D. dissertation, Ghent Univ., 2019).

[108] L. J. Zipp and D. S. Stoker, "Dual time-and wavelength-multiplexed photonic reservoir computing," in AI and Optical Data Sciences II, Proc. SPIE 11703, 1170305 (2021).

[109] G. Van der Sande, D. Brunner, and M. C. Soriano, "Advances in photonic reservoir computing," Nanophotonics 6, 561–576 (2017).

[110] F. Denis-Le Coarer, M. Sciamanna, A. Katumba, M. Freiberger, J. Dambre, P. Bienstman, and D. Rontani, "All-optical reservoir computing on a photonic chip using silicon-based ring resonators," IEEE J. Sel. Top. Quantum Electron. 24, 1–8 (2018).

[111] M. Nakajima, K. Tanaka, and T. Hashimoto, "Scalable reservoir computing on coherent linear photonic processor," Commun. Phys. 4, 20 (2021).

[112] T. Zhou, W. Wu, J. Zhang, S. Yu, and L. Fang, "Ultrafast dynamic machine vision with spatiotemporal photonic computing," Sci. Adv. 9, eadg4391 (2023).

[113] L. Appeltant, Reservoir Computing Based on Delay-Dynamical Systems, Ph.D. dissertation, Vrije Universiteit Brussel/Universitat de les Illes Balears (2012).

[114] Y. Paquot, J. Dambre, B. Schrauwen, M. Haelterman, and S. Massar, "Reservoir computing: a photonic neural network for information processing," in Nonlinear Optics and Applications IV, Proc. SPIE 7728, 77280E (2010).

[115] F. Duport, B. Schneider, A. Smerieri, M. Haelterman, and S. Massar, "All-optical reservoir computing," Opt. Express 20, 22783–22795 (2012).

[116] K. J. Bai, C. Thiem, J. Lombardi, Y. Liang, and Y. Yi, "Design strategies and applications of reservoir computing: Recent trends and prospects," IEEE Circ. Syst. Mag. 23, 10–33 (2024).

[117] P. Kumar, M. Jin, T. Bu, S. Kumar, and Y. P. Huang, "Efficient reservoir computing using field programmable gate array and electro-optic modulation," OSA Continuum 4, 1086–1098 (2021).

[118] N. Fang, R. Qian, and S. Wang, "Bidynamical all-optical reservoir computing for parallel task processing," Opt. Express 31, 35377–35386 (2023).

[119] J. García-Beni, G. L. Giorgi, M. C. Soriano, and R. Zambrini, "Scalable photonic platform for real-time quantum reservoir computing," Phys. Rev. Appl. 20, 014051 (2023).

[120] S. Ghosh, K. Nakajima, T. Krisnanda, K. Fujii, and T. C. H. Liew, "Quantum neuromorphic computing with reservoir computing networks," Adv. Quantum Technol. 4, 2100053 (2021).

[121] C. Jenila and R. K. Jeyachitra, "Green indoor optical wireless communication systems: Pathway towards pervasive deployment," Digit. Commun. Netw. 7, 410–444 (2021).

[122] T. Koonen, K. Mekonnen, et al., "Ultra-high-capacity wireless communication by means of steered narrow optical beams," Philos. Trans. R. Soc. A 378, 20190192 (2020).

[123] Z. Li, Z. Zang, Z. Wei, Y. Han, L. Wu, Z. Zhao, and H. Y. Fu, "Multi-user accessible indoor infrared optical wireless communication systems employing VIPA-based 2D optical beam-steering technique," Opt. Express 29, 20175–20189 (2021).

[124] G. Wang, et al., "Highly efficient optical beam steering using an in-fibre diffraction grating for full-duplex indoor optical wireless communication," J. Light. Technol. 36, 4618–4625 (2018).

[125] Y. Yang, A. Zhou, L. Wu, S. Xu, H. Ma, T. Wei, and X. Zhang, "Scalable 3D beam-steering for directional millimeter wave wireless networks," IEEE Trans. Wireless Commun. 21, 696–709 (2021).

[126] G. Wang, et al., "Stable and highly efficient free-space optical wireless communication system based on polarization modulation and in-fibre diffraction," J. Light. Technol. 39, 83–90 (2021).

[127] K. Wang, T. Song, Y. Wang, C. Fang, J. He, A. Nirmalathas, and S. Kandeepan, "Evolution of short-range optical wireless communications," J. Light. Technol. 41, 1019–1040 (2022).

[128] W. A. Cahyadi, Y. H. Chung, Z. Ghassemlooy, and N. B. Hassan, "Optical camera communications: Principles, modulations, potential and challenges," Electronics 9, 1339 (2020).

[129] R. Singh, et al., "Design and characterisation of terabit/s capable compact localisation and beam-steering terminals for fiber-wireless fiber links," J. Light. Technol. 38, 6817–6826 (2020).

[130] G. Simon, G. Zachár, and G. Vakulya, "Lookup: Robust and accurate indoor localization using visible light communication," IEEE Trans. Instrum. Meas. 66, 2337–2348 (2017).

[131] N. Q. Pham, et al., "User localization and upstream signaling for beam-steered infrared light communication system," IEEE Photon. Technol. Lett. (2021).

[132] T. Koonen, K. A. Mekonnen, et al., "Fully passive user localization for beam-steered high-capacity optical wireless communication system," J. Light. Technol. 38, 2842–2848 (2020).

[133] C. K. Mididoddi, et al., "Ultrafast user localization and beam steering in optical wireless communication using an in-fibre diffraction grating," in Proc. Int. Topical Meet. Microw. Photon. (MWP), IEEE, 1–3 (2018).

[134] Y. Yue, C. K. Mididoddi, N. Jing, and C. Wang, "Reservoir computing assisted ultrafast user localization in beam steering optical wireless system," IEEE Photonics Technology Letters 33, 1030–1033 (2021).

[135] C. Palmer, Diffraction Grating Handbook (2005).

[136] H. Qin, Z. Yan, Q. Sun, G. Wang, C. Wang, D. Liu, and L. Zhang, "Theoretical analysis of diffraction grating based on 45°-tilted fiber gratings," Proc. IEEE 1–2 (2017).

[137] K. Zhou, L. Zhang, X. Chen, and I. Bennion, "Low thermal sensitivity grating devices based on ex-45° tilting structure capable of forward propagating cladding modes coupling," J. Light. Technol. 24, 5087–5094 (2006).

[138] H. Qin, et al., "Theoretical analysis of diffraction grating based on 45 degrees-tilted fiber gratings," in Proc. Opto-Electronics and Communications Conference (OECC) and Photonics Global Conference (PGC), IEEE (2017).

[139] G. Wang, Z. Yan, L. Yang, L. Zhang, and C. Wang, "Improved resolution optical time stretch imaging based on high efficiency in-fiber diffraction," Sci. Rep. 8, 600 (2018).

[140] G. Manhertz and A. Bereczky, "STFT spectrogram-based hybrid evaluation method for rotating machine transient vibration analysis," Mech. Syst. Signal Process. 154, 107583 (2021).

[141] K. Nallappan and M. Skorobogatiy, "Photonics based frequency hopping spread spectrum system for secure terahertz communications," Opt. Express 30, 27028–27047 (2022).

[142] V. B. Ristić, B. M. Todorović, and N. M. Stojanović, "Frequency hopping spread spectrum: History, principles and applications," Mil. Tech. Courier 70, 856–876 (2022).

[143] Y. Wang, Y. Hao, H. Han, J. Lu, and H. Li, "Frequency hopping pattern and synchronization based on hopping spread spectrum communication," in Proc. IEEE 4th Adv. Inf. Manage., Commun., Electron. Autom. Control Conf. (IMCEC), 894–898 (2021).

[144] Y. Sun, S. Wang, J. Chen, et al., "Interference and frequency-to-time mapping based high anti-jamming and anti-interception frequency hopping receiving," Opt. Express 29, 26486–26495 (2021).

[145] M. T. Khan and U. U. Sheikh, "A hybrid convolutional neural network with fusion of handcrafted and deep features for FHSS signals classification," Expert Syst. Appl. 225, 120153 (2023).

[146] H. H. A. Hamed, A. K. Abdullah, and S. Al-waisawy, "Frequency hopping spread spectrum recognition based on discrete Fourier transform and skewness and kurtosis," Int. J. Appl. Eng. Res. 13, 7081–7085 (2018).

[147] Y. U. A. N. Jia, P. T. I. A. N., and H. Y. U., "The identification of frequency hopping signal using compressive sensing," Commun. Netw. 1, 52 (2009).

[148] Y. Yue, S. Li, Y. Feng, A. Zhang, and C. Wang, "Real-time identification of frequency-hopping millimeter-wave signals using photonic time stretch and reservoir computing," Proc. SPIE 11902, 108–112 (2021).

[149] J. Zhou, Four-wave mixing in semiconductor optical amplifiers for terahertz spectroscopy and wavelength conversion (Ph.D. dissertation, California Institute of Technology, 1995).

[150] F. D. Mahad, A. S. M. Supa'at, S. M. Idrus, and D. Forsyth, "Analyses of semiconductor optical amplifier (SOA) four-wave mixing (FWM) for future all-optical wavelength conversion," Optik 124, 1–3 (2013).

[151] Y. Yang, H. Luo, R. Zhang, F. Yang, B. Wu, K. Qiu, and F. Wen, "Semiconductor optical amplifier (SOA)-driven reservoir computing for dense wavelength-division multiplexing (DWDM) signal compensation," Sensors 23, 5697 (2023).

[152] M. C. Soriano, S. Ortín, D. Brunner, L. Larger, C. R. Mirasso, I. Fischer, and L. Pesquera, "Optoelectronic reservoir computing: tackling noise-induced performance degradation," Opt. Express 21, 12–20 (2013).

[153] "TI 46-Word Speaker-Dependent Isolated Word Corpus," NIST Speech Disc 7-1.1, National Institute of Standards and Technology (1991).

[154] B. Zhou, W. Jia, C. Xiang, Y. Xie, J. Wang, G. Jin, and C. Zhou, "Polarization-independent 2×2 high diffraction efficiency beam splitter based on two-dimensional grating," Opt. Express 29, 32042–32050 (2021).

[155] "Diffraction grating," Wikipedia, , accessed March 24, 2025.

[156] N. K. Pavlycheva, "Diffraction gratings for spectral devices," J. Opt. Technol. 89, 142–150 (2022).

[157] H. Peng, "Curved, expanded and inclined patterns of dynamic double slit/cross-double slit/grating experiments," J. Eng. 2022(2), 160–179 (2022).

[158] C. S. Baird, "Interference of waves," AccessScience (2021, August). (accessed March 17, 2025).

[159] E. Hecht, Optics, 5th ed. (Pearson, 2017), p. 497.

[160] Y. Yue, S. Liu, R. Zhang, T. Luan, A. Zhang, and C. Wang, "Experimental investigation of an optical reservoir computer with MZI-based optical mask," 2023 International Topical Meeting on Microwave Photonics (MWP), pp. 1–4 (2023).

[161] C. Wang, M. Li, and J. Yao, "Continuously tunable photonic microwave frequency multiplication by use of an unbalanced temporal pulse shaping system," IEEE Photon. Technol. Lett. 22, 1285–1287 (2010).

[162] Y. Wei, X. Wang, C. Liu, R. Wang, C. Shi, C. Liu, and T. Jiang, "High sensitivity MZI based on the modular interference with small group velocity dispersion difference," J. Light. Technol. 41, 6773–6778 (2023).

[163] M. Li and J. Yao, "All-optical short-time Fourier transform based on a temporal pulse-shaping system incorporating an array of cascaded linearly chirped fiber Bragg gratings," IEEE Photon. Technol. Lett. 23, 1439–1441 (2011).

[164] C. Wang and J. Yao, "Complete characterization of an optical pulse based on temporal interferometry using an unbalanced temporal pulse shaping system," J. Light. Technol. 29, 789–796 (2011).

[165] Y. Yue, S. Liu, and C. Wang, "Photonic time stretch reservoir computer using a multi-mode fibre-based optical mask," 2024 IEEE Photonics Conference (IPC), pp. 1–2 (2024).

[166] D.-P. Zhou, L. Wei, W.-K. Liu, and J. W. Y. Lit, "Simultaneous strain and temperature measurement with fiber Bragg grating and multimode fibers using an intensity-based interrogation method," IEEE Photon. Technol. Lett. 21, 468–470 (2009).

[167] M. Kumar, A. Kumar, and S. M. Tripathi, "A comparison of temperature sensing characteristics of SMS structures using step and graded index multimode fibers," Opt. Commun. 312, 222–226 (2014).

[168] Q. Wu, Y. Semenova, P. Wang, and G. Farrell, "High sensitivity SMS fiber structure based refractometer–analysis and experiment," Opt. Express 19, 7937–7944 (2011).

[169] Q. Wang, G. Farrell, and W. Yan, "Investigation on single-mode multimode-single-mode fiber structure," J. Light. Technol. 26, 512–519 (2008).

[170] Q. Wu, Y. Qu, J. Liu, J. Yuan, S. P. Wan, T. Wu, and G. Farrell, "Singlemode-multimode-singlemode fiber structures for sensing applications—A review," IEEE Sens. J. 21, 12734–12751 (2020).

[171] E. Reyes-Vera, C. M. B. Cordeiro, and P. Torres, "Highly sensitive temperature sensor using a Sagnac loop interferometer based on a side hole photonic crystal fiber filled with metal," Appl. Opt. 56, 156–162 (2017).